1994

Active noise control in a three-dimensional space

Jihe Yang
Iowa State University

Order Number 9424275

Active noise control in a three-dimensional space

Yang, Jihe, Ph.D.

Iowa State University, 1994

U·M·I
300 N. Zeeb Rd.
Ann Arbor, MI 48106

Active noise control in a three-dimensional space

by

Jihe Yang

A Dissertation Submitted to the

Graduate Faculty in Partial Fulfillment of the

Requirements for the Degree of

DOCTOR OF PHILOSOPHY

Department: Aerospace Engineering and Engineering Mechanics
Major: Engineering Mechanics

Approved:

Signature was redacted for privacy.

In Charge of Major Work

Signature was redacted for privacy.

For the Major Department

Signature was redacted for privacy.

For the Graduate College

Iowa State University
Ames, Iowa
1994

TABLE OF CONTENTS

LIST OF TABLES

LIST OF FIGURES

ACKNOWLEDGMENTS

I would like to express my sincere appreciation of my advisor Dr. David K. Holger for his help, suggestions and guidance. Although he is very busy most of the time, he is always generous with his time. Without his assistance, this research would not have been accomplished. I would also like to thank my committee members, Dr. Ambar K. Mitra, Dr. J. Adin Mann III, Dr. James E. Bernard and Dr. Hsien-Sen Hung for their help, encouragement, support and generous with their time.

CHAPTER 1. INTRODUCTION

1.1 Historical Review

Suppression of unwanted sound has long been an important objective of noise control research. Generally speaking, there are two basic noise control techniques, namely, passive control techniques and active cancellation. Until recently, passive techniques had been more fully developed than active techniques. Passive techniques have been studied for a quite long time and have proven to be especially effective at mid- and high-frequencies. Active noise control techniques are more recent and have been developed rapidly over the past twenty years. Active noise control is particularly efficient at low frequencies where traditional passive techniques are inefficient and expensive. The research described in this thesis deals with implementation of active noise cancellation in three-dimensional space. Active cancellation is achieved by the intentional superposition of acoustic waves to create a destructive interference pattern so that attenuation of unwanted sound occurs. The basic foundation of active noise cancellation is Young's principle which states that a pressure wave propagating in space can be canceled by the addition of the inverted wave form. The concept is straightforward, but its implementation is difficult. In order to cancel a waveform effectively, the radiation pattern must be matched exactly at every point along its propagation path. However, every sound source has its own radiation pattern, and an exact antiphase match is impossible to achieve. That is why the physical principle of active noise cancellation

has long been understood, but only recently applied. The first formalization of the method appeared in the form of a patent by Lueg [1] in 1933 in Germany. In his patent, Lueg made use of two physical principles for realizing active noise attenuation, interference and absorption. The interference principle results from the arbitrary physical mixing of acoustic waves leading to constructive and destructive interference which cause intensification and attenuation of the sound field, respectively. Lueg attempted to manipulate this principle of suppression so that the destructive interference of sound waves could be used to eliminate unwanted noise. He introduced the concept of active attenuation of sound using artificially generated acoustic waves mixed with the unwanted sound wave so that the waves were in anti-phase and destructive interference resulted. Lueg illustrated the basic phenomenon that provides the possibility of active noise control---an acoustic wave at a specific frequency travels much slower than an electrical signal with same frequency. This means that when a sound wave is traveling from a point where it is detected to a point where it is to be attenuated, there is enough time for an electronic circuit to generate an inverse signal and activate the control elements. Lueg also used the absorption principle by synchronizing the movements of a loudspeaker's diaphragm in anti-phase to the unwanted sound so that the noise energy was absorbed by the loudspeaker. Although Lueg's patent was not very extensive, the ideas he developed for active cancellation of unwanted sound waves formed the basis for modern research in active noise control. Since then, there has been considerable effort devoted to active noise control that has led to a wide range of successful applications.

Cancellation of duct noise has been an emphasis in active noise control. This is because low frequency noise propagation in ducts is of significant practical interest, and also because at low frequencies sound propagates as a plane (one-dimensional) wave in ducts. Below the duct cut-off frequency, plane waves are the only propagating modes, and it is much easier to deal with one-dimensional propagation than three. The success of the method in one

dimension provides a basis for extension to three-dimensional radiation problems because in both cases there are only outgoing waves. An acoustic monopole system was originally considered by Lueg for active noise control in ducts. In this system, the primary sound field in the duct was detected by a microphone, and a secondary source radiated sound in both upstream and downstream directions. A standing wave was produced upstream which interfered with the pattern of the unwanted noise. In this system, the noise reduction is extremely sensitive to the microphone position. In 1976, Leventhal [2] developed the Chelsea system using two secondary sources with a detector microphone midway between them. The control was set to nullify the resultant of the secondary sources at the detector location, thus isolating the detector from secondary source radiation. This system provided 20-25dB noise reduction over a narrow frequency range of less than one octave. Since the middle of 1970's, there has been significant research completed involving active noise control in ducts. Jessel and his co-workers have made important contributions to the theory of active attenuators and general consideration of sound fields pertaining to duct noise [3-6]. Their contributions have largely been based upon the application of Huygen's principle. Eriksson et al. and Zarder et al. have developed and implemented methods for high-order mode cancellation in ducts[7-8]. Shepherd and his co-workers achieved active attenuation in a duct with turbulent flow[9]. Work in the area is ongoing with significant contributions though the 1980's [10-16]. In most cases, up to 20dB of noise reduction has been achieved for frequencies up to 500Hz. This frequency limit is imposed by a combination of sampling/processing speed limitations and the failure of the plane wave model for higher frequencies.

Another important area of recent research is active noise control in cylinders. The motivation for this work is a simplified model for an of aircraft fuselage. The cylinder is elastic and vibrationally excited by external sources. A typical configuration is designed to simulate propeller noise transmitted through a fuselage wall into an aircraft cabin. Silcox et al

[17] and Lester and Fuller [18-19] investigated the use of four secondary sources placed at 90 degree increments around the cylinder in the same plane as the primary source. Significant attenuation over most of the cross section was observed. They also found that increasing the number of secondary sources improves the results. Bullmore et al [20] studied an alternate secondary source placement. They concluded that if it is impossible to place the secondary sources close to the primary sources, it is still possible to achieve good reduction provided the sources are placed so that they couple efficiently to the dominant acoustic resonant modes excited by the primary sources. Salikuddin and Ahuja [21] investigated transmission characteristics of fuselage surfaces. They obtained significant noise reduction in the interior of aircraft by using an array of four secondary sources mounted on the fuselage wall. Besides ducts and cylinders, there are many other impressive examples of active noise cancellation, including fans [22-23] and transformers [24]. Most previous applications were for simplified geometric configurations, such as one-dimensional space or free space. The implementation of active noise cancellation in a confined three-dimensional space is significantly more difficult than in one-dimensional space and free space. Three-dimensional active noise cancellation makes use of Huygen's principle which extends Young's principle to provide an approach for wide area noise reduction. It states that the sound field at any point within a closed domain produced by a sound source outside the domain can be reproduced exactly by an array of fictitious sources distributed on the surface of the domain [25]. An alternate application of Huygen's principle is to enclose the sound sources within the Huygen's surface. By generating the inverted signal at the surface, sound radiation from the sources can be attenuated. In spite of the conceptual simplicity of Huygen's principle, implementation of the principle for three-dimensional active noise control was rather slow because in theory, it requires an infinite number of point sources distributed on the Huygen's surface. Within the last fifteen years, advances in computer technology have made it possible to reasonably approximate the

Huygen's surface using a finite number of point sources. Since then, active noise cancellation in three-dimensional space has received more and more attention. Because enclosures including rooms and vehicle passenger compartment are potentially interesting applications of active noise control in three-dimensional space, they provide straight forward opportunities for application of Huygen's principle. Either the sound generated by a noise source within the enclosure is prevented from radiating or sound outside the enclosure is prevented from entering. Nelson, Bullmore, Elliott and Curtis [26-28] demonstrated active sound attenuation in a rectangular cavity. With the aid of known characteristic functions, they were able to predict the primary sound pressure distribution and perform active noise cancellation. The effect of location of secondary sources was illustrated by positioning the secondary sources at different locations and comparing results. Although they provided a useful method for active noise cancellation, their method is limited to a regular geometry with known characteristic functions. Molo and Bernhard [29] proposed a generalized method for active noise control in three-dimensional space using the boundary element method, which can be applied to any irregular geometry. There have also been a number of additional investigations of three-dimensional applications of active noise control since the middle 1980s [30-37].

1.2 Objective

Although the body of prior work discussed above has provided a number of examples of practical three-dimensional active noise control, a number of fundamental problems remain. Generally, active noise attenuation consists of three stages, i.e., prediction of the primary sound field, determination of the number and locations of secondary sources and finally optimization of secondary source strengths. Prior research has developed and implemented methods for sound field prediction and secondary source strength optimization, but none of

them has provided a systematic method for determining the optimal number or locations of secondary sources.

As mentioned above, Huygen's principle models the surface of a domain using an array of fictitious sources and the sound pressure at any point within the domain can be reproduced identically by these sources. In other words, the sound pressure at any point within the domain can be reduced to zero if the secondary sources generate an inverted version of the sound wave incident on the surface. Practically, it is impossible to obtain zero sound pressure within the entire domain, but it should be possible to optimize reduction of sound pressure by optimizing both locations and strengths of the secondary sources using information about the fictitious source distribution on the Huygen's surface. The objective of this research is to improve active noise attenuation in three-dimensional spaces by developing a systematic method for locating and optimizing the strength of secondary sources. The focus, as well as the main contribution of this research, is a method for optimizing the locations of secondary sources using the fictitious source strength distribution on the boundary. The feasibility of improving attenuation by optimizing secondary source locations using the fictitious source distribution on the boundary of the domain is described theoretically and verified numerically.

1.3 Numerical Implementation

Active noise cancellation system design requires that the characteristics of the primary sound field be known. The acoustic fields investigated in this research are assumed to be stationary and time harmonic. Even with these restrictions, analytic solutions of sound fields are only available for a limited number of special problems. For many practical problems, there are no analytical solutions. Arbitrary acoustic fields can, however, be simulated numerically. There are several numerical methods that can be applied to predict radiated

acoustic fields including the finite element method, the finite difference method and the boundary element method. Among these numerical techniques, the indirect boundary element method is an implementation of Huygen's principle and a potentially efficient method for acoustic problems. For well-posed boundary conditions, the radiated fields of primary sources can be predicted, and the corresponding fictitious source distribution representing the effect of the domain boundaries can be determined. Once the radiated field of the primary noise sources and the fictitious source distribution representing the boundary have been determined, the secondary source locations and strengths can be optimized. The proposed optimization process involves two steps; secondary source location optimization and secondary source strength optimization. It is proposed that optimal locations of secondary sources can be deduced from the fictitious source strength distribution on the boundary of the domain resulting from the specified primary noise sources. The optimal strengths of the secondary sources are calculated by minimizing the sum of the squared pressure at selected observation points.

Chapter 2 of this thesis discusses the indirect boundary integral equations and their numerical implementation. Selected special cases with known analytical solutions will be used to verify the accuracy of the computer implementation of the indirect boundary element method for both interior and exterior problems with either Dirichlet or Neumann boundary conditions. In Chapter 3, the proposed optimization method for secondary source locations and strengths will be described. Finally in Chapter 4, selected active noise control applications in three-dimensional space will be examined using the optimization approach presented in Chapter 3. Interior and exterior radiation problems involving rectangular cavities were simulated on the computer to illustrate predicted active noise cancellation using the proposed optimization methods. Different boundary conditions, including rigid wall and finite normal acoustic impedance, were also considered to investigate the versatility of the method. It was

demonstrated that different strategies may be necessary for local or global active noise control. The numerical results obtained in this work are also compared to experimental and numerical results from the archival literature.

CHAPTER 2. BOUNDARY ELEMENT METHOD FOR ACOUSTIC PROBLEMS

2.1 Introduction

This chapter is concerned with the development and implementation of the boundary element method for solution of acoustic boundary value problems governed by the wave equation. The time harmonic acoustic radiation problem is represented by a boundary integral equation based upon Huygen's principle. This integral equation approach is valid for both interior and exterior acoustic radiation problems, except at certain characteristic frequencies, which are the resonant frequencies of the corresponding interior domain. A numerical implementation of Huygen's principle, known as the indirect boundary element method (IBEM), will be presented. The formulations of pressure, velocity and normal acoustic impedance boundary conditions are incorporated into this numerical technique. In this work, quadratic boundary elements were used for the numerical approximation. The difficulty in dealing with edge and corner collocation points where the outward normal is not unique is investigated and a method to circumvent the difficulty is described and implemented. To verify the numerical approach used in this investigation, examples are presented for both interior and exterior acoustic radiation problems using either a point source or a pulsating sphere source in free space, half space and enclosed cavities. The numerical predictions are also compared with existing analytical solutions. Good agreement between numerical and

analytical results are observed for all cases investigated. Although only selected geometries have been investigated, this method and its implementation are general and could be applied to any geometry.

2.2 Boundary Integral Formulation

The problems to be considered all deal with acoustic behavior in a three-dimensional space. A general geometry considered is shown in Figure 2.1. A primary acoustic point source with strength Ψ is located by the vector $\vec{x}_s$ within the domain D. Likewise, an arbitrary point x within the domain is defined by vector $\vec{x}$ and a point on the boundary B is represented by ζ. For this problem, the governing differential equation in terms of the velocity potential is the scalar wave equation

$$\nabla^2\Phi - \frac{1}{c^2}\frac{\partial^2\Phi}{\partial t^2} = \Psi(\bar{x}_s) \tag{2.1}$$

where Φ is the complex velocity potential, c the speed of sound propagation and t the time. When harmonic time dependence is assumed, i.e., $\Phi=\phi e^{-j\omega t}$ and $\Psi=\psi e^{-j\omega t}$ equation (2.1) becomes

$$\nabla^2\phi + k^2\phi = \psi(\bar{x}_s) \tag{2.2}$$

where $\omega = kc$ is the angular frequency and k the wave number. Equation (2.2) is the linearized, lossless Helmholtz equation for time harmonic acoustic waves in terms of the velocity potential ϕ. The definition of velocity potential is

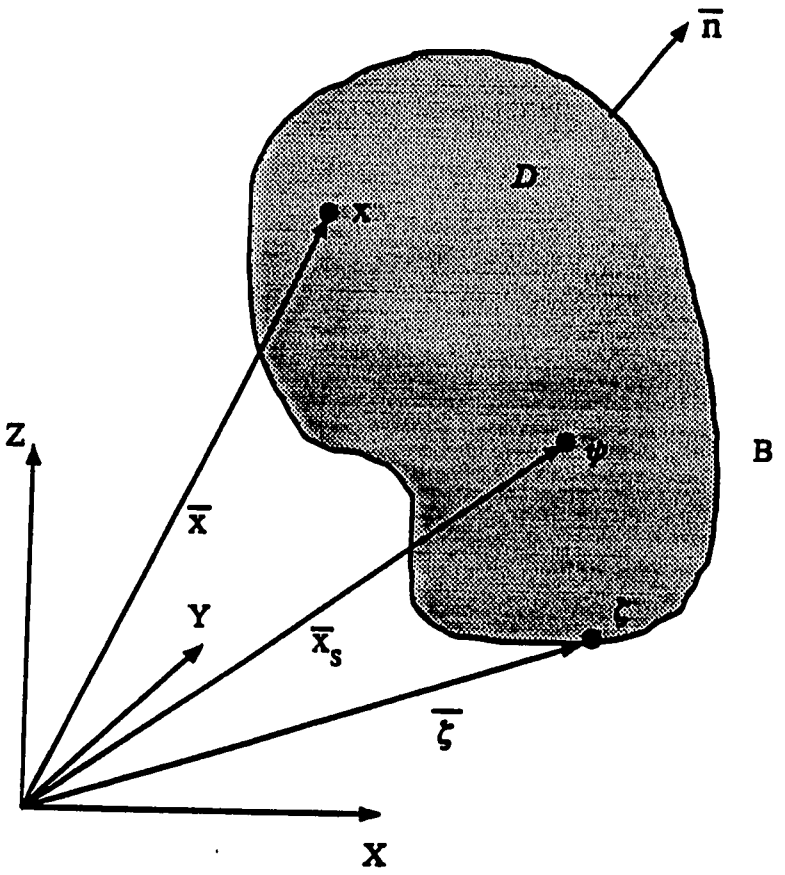

Figure 2.1: Problem description.

$$u = \nabla\phi \tag{2.3}$$

where u is acoustic particle velocity. The acoustic pressure, p, is related to the velocity potential by equation (2.3) and the linearized momentum equation

$$\nabla p = -\rho \frac{\partial u}{\partial t}$$

where ρ is the density of fluid. With harmonic time dependence, the above equation can be rewritten as

$$\nabla p = -j\omega\rho\nabla\phi$$

thus

$$p = -j\omega\rho\phi \tag{2.4}$$

Two far field boundary conditions are necessary for acoustic radiation problems to ensure that the velocity potential, ϕ, and also the pressure, p, behave in a physically correct fashion far from the primary source. The conditions that are normally applied are

$$\lim_{r\to\infty}[\phi(r)] = 0$$

and the Sommerfeld radiation condition [38]

$$\lim_{r\to\infty}[r(j\frac{\partial\phi}{\partial r}+k\phi)]=0 \tag{2.5}$$

is imposed on the velocity potential ϕ.

To solve equation (2.2) for the velocity potential, ϕ, as well as the pressure, p, and the particle velocity, u, using equations (2.3) and (2.4), the approach of this work is a boundary integral method that is an implementation of Huygen's principle. The method is general and can be employed to deal with a variety of interior and exterior acoustic problems in three-dimensional space. According to Huygen's principle, the effect of the domain boundary can be represented by a fictitious source distribution that will reproduce an identical sound field in the domain. The mathematical representation of this principle is

$$\phi(x)=\int_{\Gamma}\sigma(\xi)G(\xi,x)d\Gamma(\xi)+\int_{V}\psi(x_s)G(x_s,x)dV \tag{2.6}$$

where σ is the fictitious source strength distribution on the boundary, $G=\frac{1}{4\pi r}e^{jkr}$ the free space Green's function, r the distance between any two points, k the wave number, ξ an arbitrary point on the boundary, x_s the locations of physical sources, Γ the total surface of the boundary and V the total volume of the domain D. The domain D may be the interior or exterior of the boundary surface Γ.

In the general case, equation (2.6) is subject to the general mixed boundary condition

$$\alpha\phi+\beta\frac{\partial\phi}{\partial n}=\gamma \tag{2.7}$$

where α, β, and γ are arbitrary constants in complex form and n the outward normal to the boundary Γ. When $\alpha = 1$ and $\beta = 0$, equation (2.7) reduces to the essential boundary condition

$$\phi = \gamma \tag{2.8}$$

When $\alpha = 0$ and $\beta = 1$, equation (2.7) becomes the natural boundary condition

$$\frac{\partial \phi}{\partial n} = \gamma \tag{2.9}$$

Another important boundary condition, known as the normal acoustic impedance boundary condition, results from specifying a linear combination of ϕ and $\frac{\partial \phi}{\partial n}$ on the boundary. The definition of normal acoustic impedance is

$$z_n = \frac{p}{u_n} \tag{2.10}$$

where z_n is the normal acoustic impedance, u_n the normal acoustic particle velocity on the boundary and p the acoustic pressure on the boundary. Substituting equation (2.3) and (2.4) into equation (2.10), the normal acoustic impedance can be represented in terms of the velocity potential as

$$z_n = -\frac{j\omega\rho\phi}{\frac{\partial\phi}{\partial n}} \tag{2.11}$$

or

$$jk\phi + \frac{z_n}{\rho c}\frac{\partial\phi}{\partial n} = 0 \tag{2.12}$$

Comparing equation (2.12) with equation (2.7), it is seen that equation (2.12) is a special case of the general boundary condition with $\alpha = jk$, $\beta = \frac{z_n}{\rho c}$ and $\gamma = 0$.

It has been proved [39] that equation (2.6) gives a solution that satisfies both the Helmholtz equation (2.2) and the radiation condition (2.5). In order to calculate the velocity potential using equation (2.6), the fictitious source strength distribution σ must first be determined. This is done by collocating the field point x onto the boundary and forcing the solution for σ to satisfy the imposed boundary condition. $\phi(x)$ in equation (2.6) is a continuous function of x, differentiable to all orders everywhere except at $x \in \Gamma$, where the integrand contains a singularity. This singularity can be investigated by breaking the boundary into two surfaces when the field point is collocated onto the boundary. One of the surfaces is a small disc tangent to the surface at point x and the other is the entirety of the remaining surface containing no singularity, as shown in Figure 2.2(a). It is assumed that the boundary surface has a unique tangent plane at any point.

For the essential boundary condition, equation (2.6) becomes

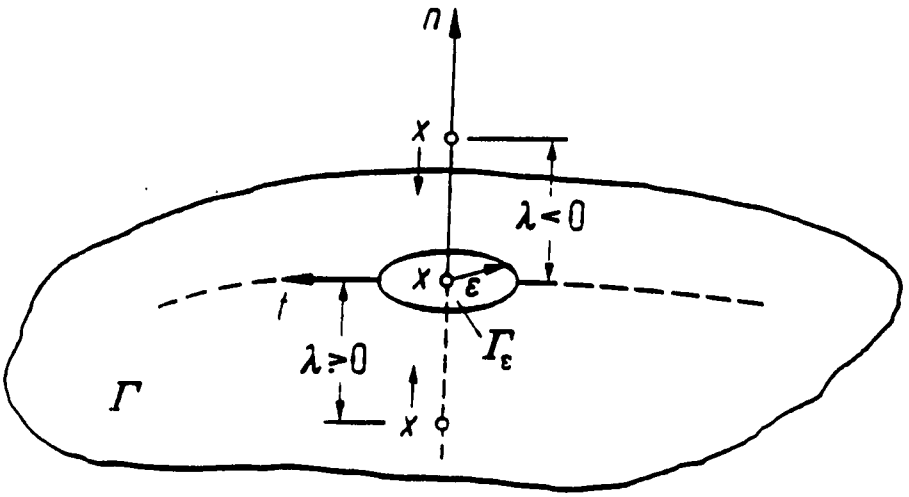

(a)

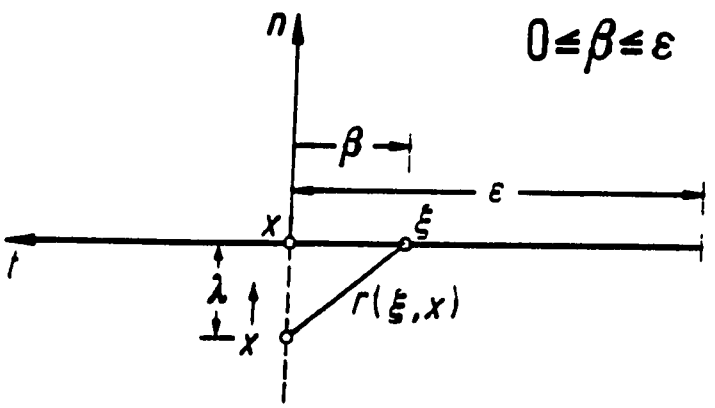

(b)

Figure 2.2: Discontinuity of the boundary integral kernel.

$$\phi(x) = \lim_{\varepsilon \to 0} \left\{ \int_{\Gamma_\varepsilon} \sigma(\xi) G(\xi, x) d\Gamma(\xi) + \int_{\Gamma - \Gamma_\varepsilon} \sigma(\xi) G(\xi, x) d\Gamma(\xi) \right\} + \int_V \psi(\xi) G(x_s, x) dV \qquad (2.13)$$

In equation (2.13), the third integral is regular when x is on the boundary and the second integral is continuous as the field point x approaches the boundary and will produce the same integral when the limit is taken. By substituting the Green' function and using polar coordinates, the first integral can be written as

$$\lim_{\varepsilon \to 0} \int_{\Gamma_\varepsilon} \sigma(\xi) \frac{1}{4\pi r} e^{jkr} d\Gamma(\xi) = \lim_{\varepsilon \to 0} \int_{\Gamma_\varepsilon} \frac{1}{4\pi} \sigma(\xi) e^{jkr} dr d\theta \qquad (2.14)$$

which vanishes when ε approaches zero as long as σ is bounded. Thus, for the essential boundary condition, equation (2.6) reproduces itself when the field point is collocated onto the boundary.

$$\phi(x_b) = \int_\Gamma \sigma(\xi) G(\xi, x_b) d\Gamma(\xi) + \int_V \psi(x_s) G(x_s, x_b) dV \qquad (2.15)$$

where x_b is a point on the boundary Γ.

For the natural boundary condition, when the field point is collocated onto the boundary, the representation of the boundary integral is obtained by differentiating equation (2.6) with respect to the outward normal n as

$$\frac{\partial \phi(x)}{\partial n(x)} = \int_\Gamma \sigma(\xi) \frac{\partial G(\xi, x)}{\partial n(x)} d\Gamma(\xi) + \int_V \psi(x_s) \frac{\partial G(x_s, x)}{\partial n(x)} dV \qquad (2.16)$$

It is obvious that the second integral contains no singularity while the first one is singular when the field point approaches the boundary. Again the total boundary can be split into two parts, $\Gamma-\Gamma_\varepsilon$ and Γ_ε. Equation (2.16) then becomes

$$\frac{\partial\phi(x)}{\partial n(x)}=\lim_{\varepsilon\to 0}\left\{\int_{\Gamma_\varepsilon}\sigma(\xi)\frac{\partial G(\xi,x)}{\partial n(x)}d\Gamma(\xi)+\int_{\Gamma-\Gamma_\varepsilon}\sigma(\xi)\frac{\partial G(\xi,x)}{\partial n(x)}d\Gamma(\xi)\right\} +\int_V\psi(x_s)\frac{\partial G(x_s,x)}{\partial n(x)}dV \tag{2.17}$$

In equation (2.17), only the first integral contains a singularity and it can be rewritten as

$$I=\lim_{\varepsilon\to 0}\left\{\int_{\Gamma_\varepsilon}\frac{1}{4\pi}\sigma(\xi)\left[\frac{1}{r}\frac{\partial}{\partial n}(e^{jkr})+e^{jkr}\frac{\partial}{\partial n}\left(\frac{1}{r}\right)\right]d\Gamma(\xi)\right\} \tag{2.18}$$

The first term can be written as

$$I_1=\lim_{\varepsilon\to 0}\int_{\Gamma_\varepsilon}\frac{jk}{4\pi r}\sigma(\xi)e^{jkr}\nabla r\cdot\vec{n}d\Gamma(\xi)$$

It is easy to see that this term is the same form as equation (2.14) and will go to zero as ε goes to zero. Then equation (2.18) can be written as

$$I=\frac{1}{4\pi}\lim_{\varepsilon\to 0}\left\{\int_{\Gamma_\varepsilon}[\sigma(\xi)-\sigma(x)]e^{jkr}\frac{\partial}{\partial n}\left(\frac{1}{r}\right)d\Gamma(\xi)+\sigma(x)\int_{\Gamma_\varepsilon}e^{jkr}\frac{\partial}{\partial n}\left(\frac{1}{r}\right)d\Gamma(\xi)\right\} \tag{2.19}$$

In equation (2.19) the first integral is zero when $x\to\xi$. Equation (2.18) then becomes

$$I=\frac{1}{4\pi}\lim_{\varepsilon\to 0}\left\{\sigma(x)\int_{\Gamma_\varepsilon}e^{jkr}\frac{\partial}{\partial n}\left(\frac{1}{r}\right)d\Gamma(\xi)\right\} \tag{2.20}$$

According to Figure 2.2(a), the disc centered at x has a radius ε and surface area Γ_ε. The field point x, originally located at a distance λ from the surface, moves along the normal to the boundary surface in such way that $|\lambda|<<\varepsilon$. It is assumed that $\lambda>0$ if x moves in the direction of normal and $\lambda<0$ if x moves in opposite direction with the normal. With Figure 2.2(b), equation (2.20) becomes

$$I=\frac{1}{4\pi}\lim_{\varepsilon\to 0}\left\{\sigma(x)\int_{\Gamma_\varepsilon}e^{jkr}\frac{1}{r^2}\nabla r\cdot\vec{n}d\Gamma(\xi)\right\} \tag{2.21}$$

Substituting

$$\nabla r\cdot\vec{n}=\cos\theta=\frac{\lambda}{r} \tag{2.22}$$

and

$$d\Gamma = 2\pi\beta d\beta \tag{2.23}$$

into equation (2.21), equation (2.20) may be rewritten as

$$I = -\frac{1}{4\pi}\lim_{\varepsilon\to 0}\left\{\sigma(x)\int_0^{\varepsilon} e^{jkr}\frac{\lambda}{r^3}2\pi\beta d\beta\right\} \tag{2.24}$$

With further approximation as $\beta d\beta \equiv rdr$ since $|\lambda|<<\varepsilon$, the right side of equation (2.24) becomes

$$I = -\frac{1}{2}\lim_{\varepsilon\to 0}\left\{\sigma(x)\int_{|\lambda|}^{\varepsilon} e^{jkr}\frac{\lambda}{r^2}dr\right\} = \frac{1}{2}\lim_{\varepsilon\to 0}\left\{\sigma(x)\left[\frac{\lambda}{\varepsilon}e^{jk\varepsilon} - \frac{\lambda}{|\lambda|}e^{jk|\lambda|}\right]\right\} \tag{2.25}$$

By taking the limit and noting that $\lambda\to 0$ much faster than ε, equation (2.18) can finally be written in the form of

$$I = -\frac{1}{2}\sigma(x)sgn(\lambda) \tag{2.26}$$

Thus, with the normal velocity boundary condition, the boundary integral representation is

$$u_n(x_b) = \pm\frac{1}{2}\sigma(\xi) + \int_\Gamma \sigma(\xi)\frac{\partial G(\xi, x_b)}{\partial n(x_b)}d\Gamma(\xi) + \int_V \psi(x_s)\frac{\partial G(x_s, x_b)}{\partial n(x_b)}dV \tag{2.27}$$

where the positive sign is for exterior problems and the negative sign is for interior problems.

The boundary integral formulation for the normal acoustic impedance boundary condition can be derived from equations (2.4), (2.6), (2.10) and (2.27). Equation (2.10) can be rewritten as

$$p - z_n u_n = 0 \tag{2.28}$$

Incorporating this with equations (2.4), (2.6), and (2.27) gives

$$\begin{aligned} &\pm\frac{1}{2} z_n(x_b)\sigma(x_b) + \int_\Gamma \sigma(\xi)[z_n(x_b)\frac{\partial G(\xi, x_b)}{\partial n(x_b)} + j\omega\rho G(\xi, x_b)]d\Gamma(\xi) \\ &= -\int_V [j\omega\rho\psi(x_s)G(x_s, x_b) + z_n(x_b)\psi(x_s)\frac{\partial G(x_s, x_b)}{\partial n(x_b)}]dV \end{aligned} \tag{2.29}$$

It has been proved by Schenck [39] and Filippi [40] that both equations (2.15) and (2.27), and thus equation (2.29), have unique solutions for any wave number except at eigenvalues of the corresponding interior problem.

2.3 Numerical Implementation

2.3.1 Boundary element method

Equations (2.13), (2.27) and (2.29) represent the boundary integral equations where the field variable ϕ is forced to satisfy the imposed boundary condition of pressure, normal particle velocity and normal acoustic impedance, respectively. The numerical implementation of Huygen's principle, i.e., the computational scheme used in this work to solve these equations is called the indirect boundary element method (IBEM). The boundary element

method is a numerical procedure to solve integral equations via a discretization of only the boundary of the domain The unknown variables on the boundary are approximated by shape functions on each element of the boundary surface so that the unknown function is replaced by discrete nodal values. To determine these nodal values, the boundary integral equations are collocated at each node with known boundary condition so that the original boundary integral equations are converted into a finite set of linear algebraic equations. The solutions of the original problems are approximated by the solutions of these linear algebraic equations. Each element integration in the boundary element method is evaluated relative to all collocation points or nodes and hence couples all nodes and not just its neighboring nodes as in the finite element method. Thus the resulting matrices are fully populated.

2.3.2 Shape function approximation

The boundary integral equations are approximated by dividing the boundary into small elements, see Figure 2.3. The variables on each element are represented by shape functions according to the values at nodes. The evaluations of the discretized integrals reduce the integral equations to a system of linear algebraic equations, which can be solved for unknown variables by applying the preimposed boundary conditions.

The numerical procedure employed in this work uses quadratic shape functions to approximate both unknowns and the geometry of each boundary element. The boundary is discretized into curvilinear quadrilateral or triangular elements and mapped to standard squares or equilateral triangles, respectively, as shown in Figure 2.4. The quadrilateral elements have eight nodes and triangular elements have six nodes, with the corner nodes numbered consecutively followed by midside nodes in clockwise fashion as shown in Figure 2.3. The triangles are considered to be degenerated quadrilaterals in which three of the nodes,

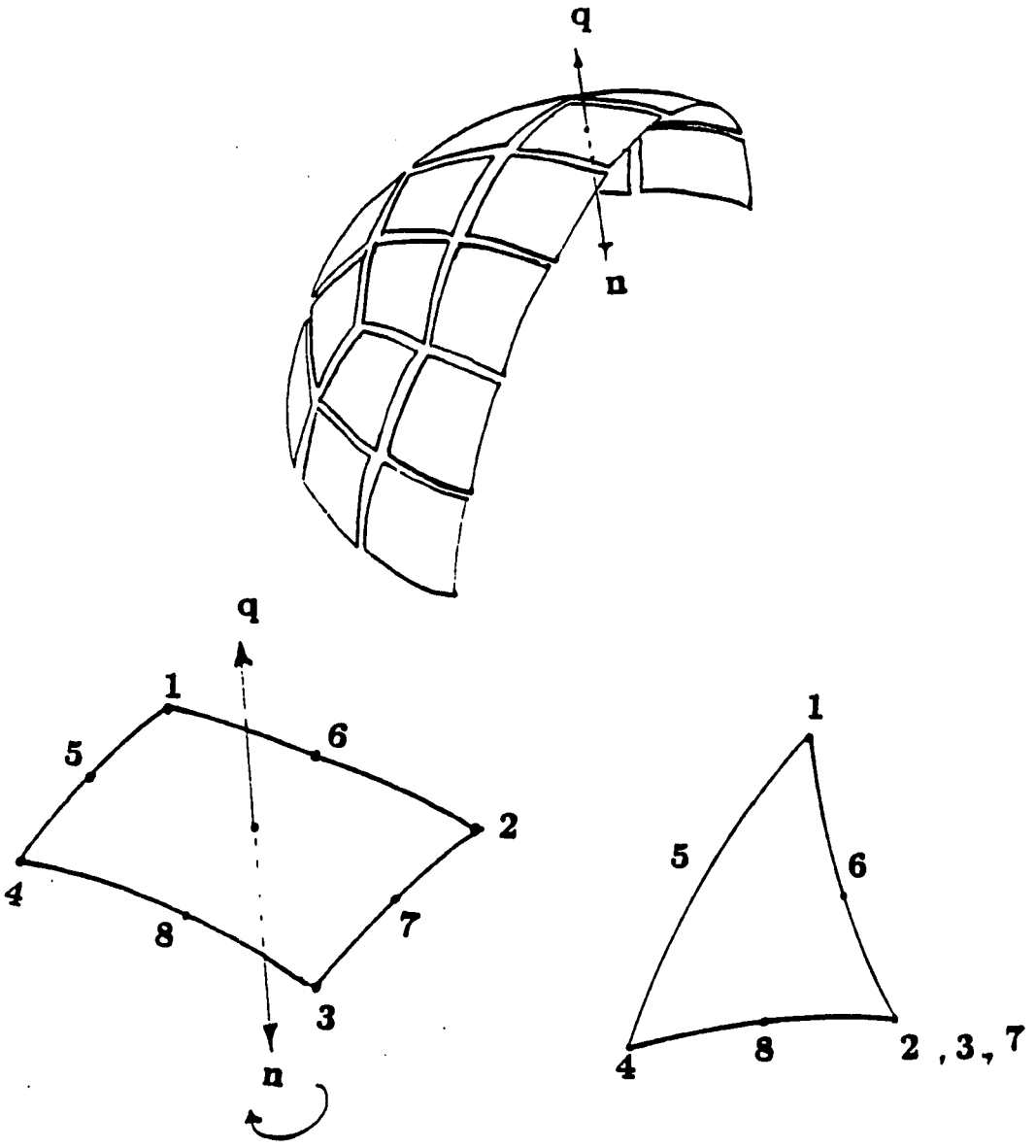

Figure 2.3: Boundary elements and connectivity.

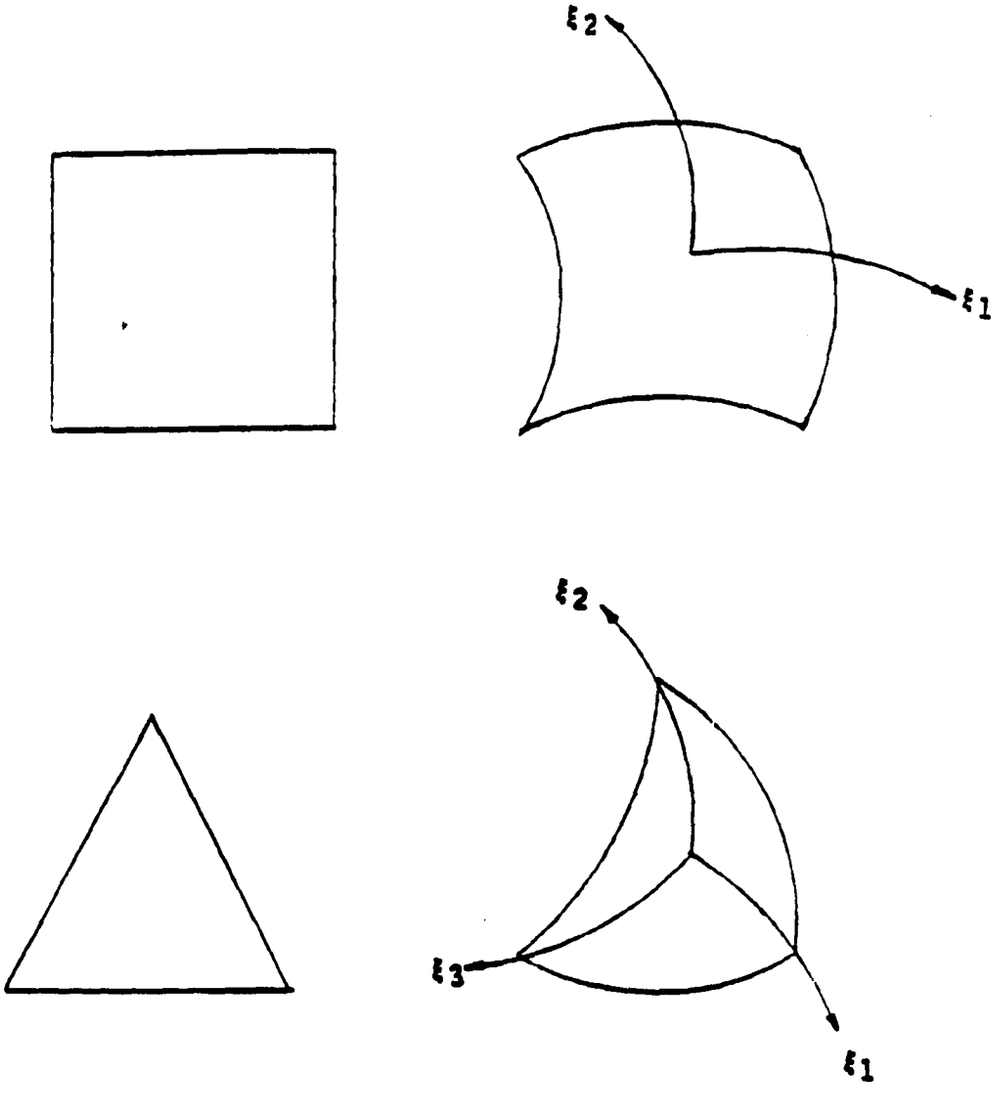

Figure 2.4: Mapping of curvilinear elements.

2nd, 3rd and 7th, have collapsed into one. The clockwise numbering convention sets the normal direction $\bar{n}$ for the elements.

The boundary Γ is broken into m elements and ξ_i denotes the local coordinates on each element. A variable ϕ over an element is thus represented as

$$\phi(\xi) = \sum_{j=1}^{n} N_j(\xi)\phi_j \tag{2.30}$$

where n is the total number of nodes on the element, ϕ_j the nodal values of ϕ on the element and $N_j(\xi)$ the shape functions. The general quadratic shape functions of the quadrilaterals and triangles are listed in the Appendix A in terms of local coordinates ξ_i.

The surface geometry of each element is similarly approximated by quadratic shape functions matching the nodal coordinates on the element. The global Cartesian coordinate x for a geometric point on the element is represented by

$$x = \sum_{j=1}^{n} N_j(x)x_j \tag{2.31}$$

where x_j is the coordinate of the j-th node on the element.

2.3.3 Numerical evaluation of integrals

A general formulation of the boundary integral described in this chapter has the generic form

$$I(x)=\int_{\Gamma}\phi(y)K(y,x)d\Gamma(y) \tag{2.32}$$

where I is the variable of interest, ϕ the variable on the boundary and K the integral kernel. If Γ is divided into m elements with n nodes and area $\partial\Gamma$ for each element, the integration (2.32) can be represented as the sum of these elements

$$I(x)=\sum_{i=1}^{m}\int_{\partial\Gamma}\phi(y)K(y,x)d\Gamma(y) \tag{2.33}$$

With the application of shape functions from equations (2.30) and (2.31), equation (2.33) can be written as

$$I(x)=\sum_{i=1}^{m}\sum_{j=1}^{n}\phi_{ij}\int_{\partial\Gamma}N_j(\xi)K(\xi,x)J(\xi)d\Gamma(\xi) \tag{2.34}$$

where ϕ_{ij} is the value of ϕ at the j-th node of the i-th element and $J(\xi)$ the Jacobean of coordinate transformation, i.e.,

$$d\Gamma = J(\xi_1,\xi_2)d\xi_1 d\xi_2 \tag{2.35}$$

The integral on each element can then be evaluated by Gaussian quadrature.

After discretizing the boundary Γ into elements and collocating field points onto the boundary nodes by sequence, equations (2.15), (2.27) and (2.29) can be written as a set of

linear algebraic equations. For a discretization of N total nodes, these equations can be represented in a matrix form as

$$[A][\sigma]=[R] \tag{2.36}$$

where A is a known N×N square coefficient matrix related to the geometry of the boundary, σ a column vector containing the unknown fictitious source strength at each boundary node and R a column vector of prescribed boundary conditions as well as the contribution from primary sources. Equation (2.6) can also be rewritten in matrix form as

$$[\phi]=[H][\sigma]+[\psi_s] \tag{2.37}$$

where ϕ is a column vector of velocity potential at each field point, H a known coefficient matrix relating to boundary nodes and field points and ψ_s a column vector containing the direct contribution from primary sources.

Once equation (2.36) is solved for fictitious source strength σ, equation (2.37) can be employed to evaluate the velocity potential ϕ at each field point. Finally, the acoustic variables such as pressure and particle velocity can be calculated using equations (2.3) and (2.4), respectively.

2.3.4 Dealing with corner and edge nodal points

In the above description of boundary integral equations and their numerical implementation, it is assumed that the boundary surface has a unique tangent plane at any point, i.e., a smooth boundary surface. However, there are many practical problems that involve geometric discontinuities such as edges and corners. For these problems, the velocity

potential is uniquely defined, but its normal derivatives are multivalued at the edges and corners. Therefore, equations (2.27) and (2.29) are not valid at edges and corners. To circumvent this problem, three methods of approximation have been investigated as part of this research. The first method is to leave a gap at the edge so that each boundary node has a unique normal derivative. The second uses the multiple independent node concept, i.e., to collocate each edge node twice (three times for corner nodes) with different normal corresponding to each surface. The third method shifts the edge node and corner node to each corresponding surface so that each shifted node has a unique normal.

The method adopted in this work is the third one because numerical results suggest that this technique give the best approximation for the edge and corner nodes. In this technique, the edge node is broken into two nodes (three nodes for corner nodes). These nodes are then shifted onto the corresponding boundary surfaces. Thus, each node has a unique tangent surface. The geometry of each boundary element is still modeled with nodes at corners or edges, but the acoustic variables on each boundary element are approximated using shifted boundary nodes. The geometry of the boundary and acoustic variables are mapped with different shape functions for elements on edges and corners. The shape functions for all types of boundary elements are presented in Appendix A. The shrinkage of each edge node is 20% of the element dimension in the direction of shifting as shown in Appendix A. With this kind of mapping, the geometry of the boundary remains unchanged. The only difference from isoparametric elements is the mapping of the variables on each edge element using different nodes and different shape functions. This difference will not introduce additional error, but it will increase the number of degrees of freedom for the system. With typical computers, this trade-off is negligible. Numerical experiments indicated that this method gives satisfactory results.

2.3.5 Solution procedures

Once the numerical procedures described above have been applied to approximate and assemble the system matrix, equation (2.36) can be used to solve for the fictitious source strength distribution, σ, on the boundary. To solve for, σ, a complex equation solver is needed. The matrix equation is neither banded nor triangular so a robust equation solver is required. The subroutines used, LINPACK [41] subroutines cgefa, cscal, cgeco and cgesl, are double precision linear equation solvers for complex systems of equations. Since matrices in the boundary element method, unlike the finite element method, are fully populated, the matrices are first factored by Gaussian elimination and then solved.

2.4 Validation of the Numerical Implementation

Numerical results are presented in this section for several acoustic problems that were used to verify the computer implementation of the IBEM described above. These examples include both interior and exterior problems with essential and natural boundary conditions. Point sources or pulsating sphere sources were used as primary sources. Numerical predictions of the acoustical field are compared with the available analytical solutions for selected cases.

2.4.1 Point source in free field

A point source with strength $\psi = 1$, located at (0, 0, 0) in a rectangular coordinate system was used to verify numerical results for exterior radiation problems with pressure and normal particle velocity boundary conditions. The driving frequency selected was 200Hz for this case. Four hundred field points were selected on a plane surface defined by -1m≤x≤1m, -1m≤y≤1m and z=3m. The analytical solution [42] for the problem is given by

$$p(r) = \frac{\psi}{4\pi r} e^{jkr} \tag{2.38}$$

where p is the acoustic pressure at any field point, r the distance from the point source to the field point, k the wave number and ψ the strength of the point source. Figure 2.5 contains the analytical results for the magnitude of the pressure at field points using equation (2.38).

Numerical results were obtained for both pressure and normal velocity boundary conditions. An imaginary spherical surface with radius r=0.1m was used as the boundary for this example. The imaginary spherical surface was divided into 72 boundary elements. The acoustic pressure at each boundary node was obtained using equation (2.38) as the pressure boundary condition. The normal particle velocity at each boundary node can be calculated from equation (2.38) and Euler's equation

$$\nabla p = -\rho \frac{\partial u}{\partial t}$$

as

$$u_n(r) = -\frac{\psi}{4\pi\omega\rho}\left[\frac{j}{r^2} + \frac{k}{r}\right] e^{jkr} \tag{2.39}$$

The numerical predictions with different boundary conditions are plotted in Figures 2.6 and 2.7. Comparing the numerical prediction of Figure 2.6 and Figure 2.7 with the analytical results of Figure 2.5, it is observed that good agreement has been obtained for this case. The

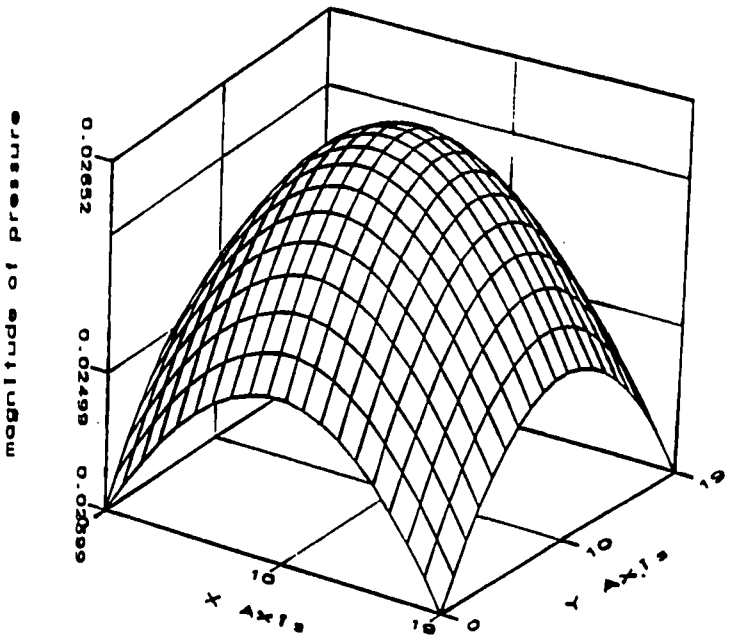

Figure 2.5: Analytic result of pressure distribution for a point source in free field.

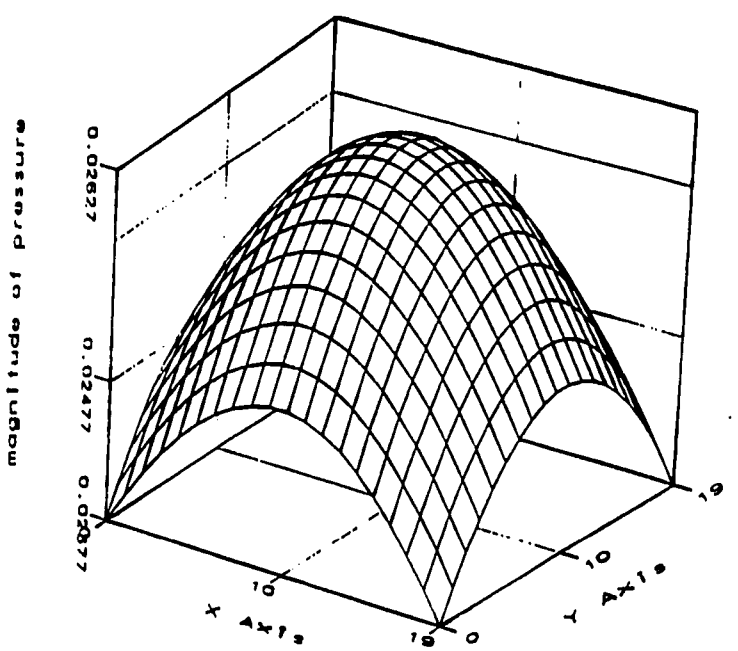

Figure 2.6: IBEM result of pressure distribution for a point source in free field with pressure boundary condition and 72 boundary elements.

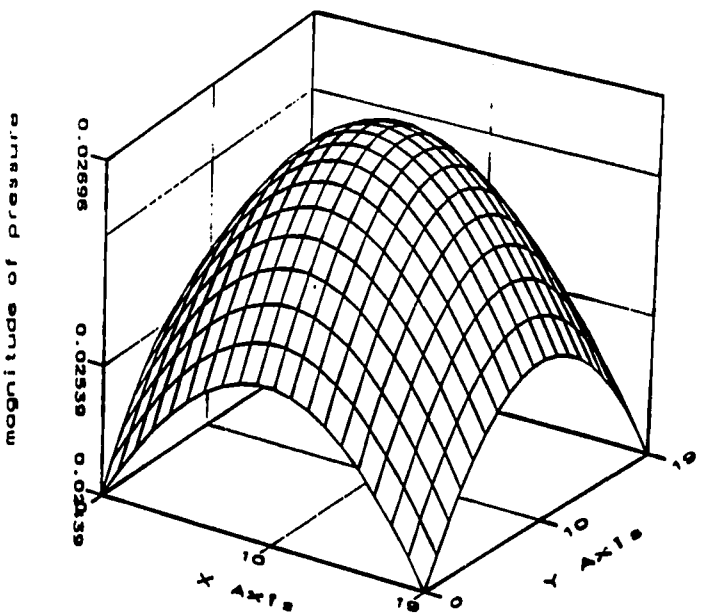

Figure 2.7: IBEM result of pressure distribution for a point source in free field with normal velocity boundary condition and 72 boundary elements.

relative error of the maximum and minimum values are only 0.943% and 0.917% for the pressure boundary condition and 1.67% and 1.66% for the velocity boundary condition.

2.4.2 A point source near an infinite rigid plane

In this case, a point source with strength ψ =1 was placed at (0, 0, 0.5). An infinite plane was located at z=0. The driving frequency was again 200Hz. Four hundred field points were evenly distributed on the plane surface -1m≤x≤1m, -1m≤y≤1m and z=3m. An analytical solution can be obtained for this case using the image method [43] as shown in Figure 2.8. The acoustic image point source S_i is located at (0, 0, -0.5) with the same strength as the physical point source. The infinite plane is replaced by the image source that combined with the physical acoustic point source S_a can satisfy the boundary condition at z=0 as well as the radiation condition at $r \to \infty$. The acoustic pressure at any field point is expressed as

$$p(R,R') = \frac{\psi}{4\pi}\left[\frac{1}{R}e^{jkR} + \frac{1}{R'}e^{ikR'}\right] \tag{2.40}$$

where R is the distance from the physical point source to the field point and R' the distance from the image source to the field point. The magnitude of the pressure distribution at field points predicted by equation (2.40) is shown in Figure 2.9.

In the numerical model, the infinite plane was replaced by a finite plane with dimensions 10m×10m. The plane surface was assumed to have zero thickness so that only one surface was discretized. The boundary of the plane surface was divided into a 20×20 element grid in the x and y directions, respectively. For this rigid plane, the boundary condition was $u_n = 0$ everywhere on the plane surface. Numerical results for this case are plotted in Figure 2.10. Comparing Figures 2.9 and 2.10 reveals that the numerical predictions

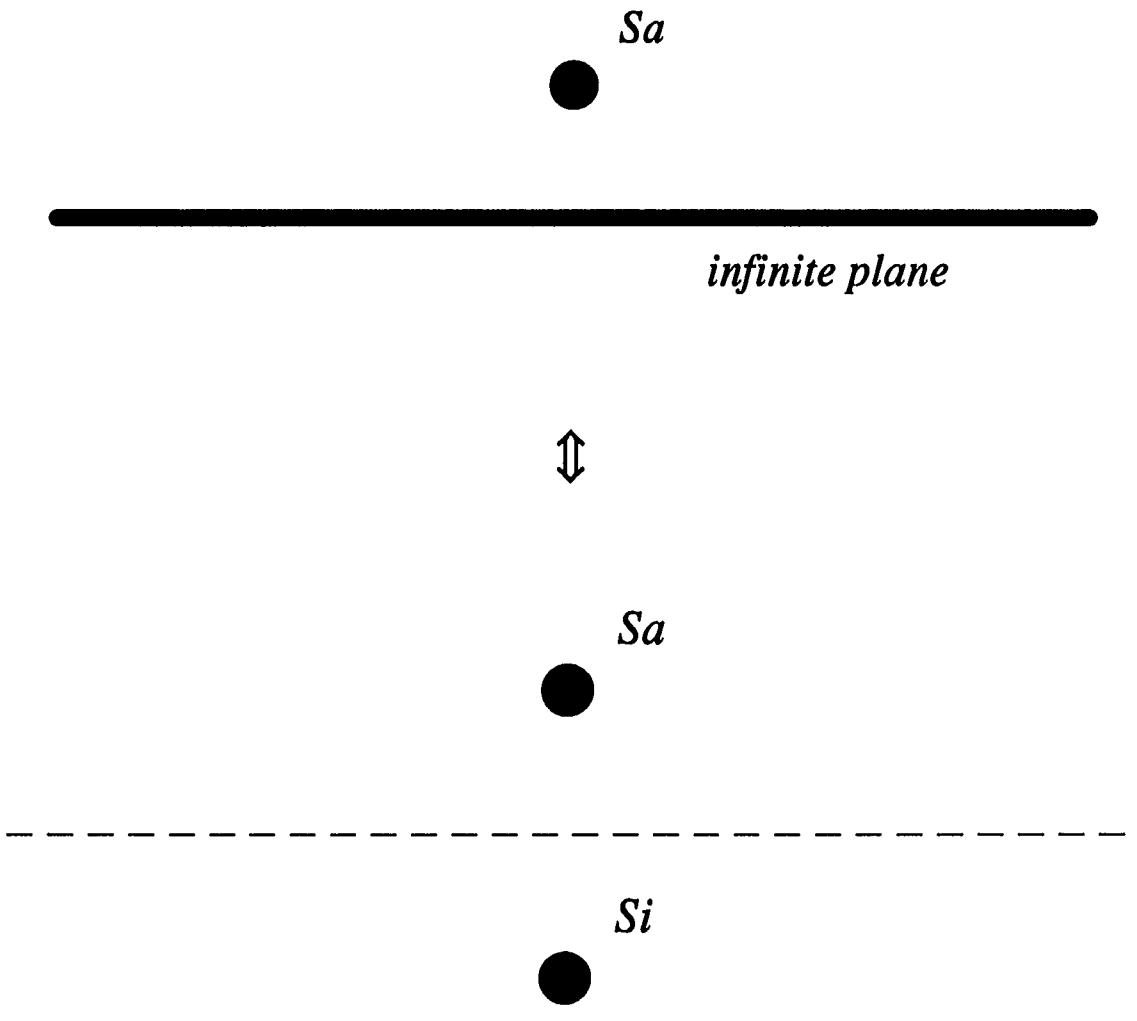

Figure 2.8: Image geometry.

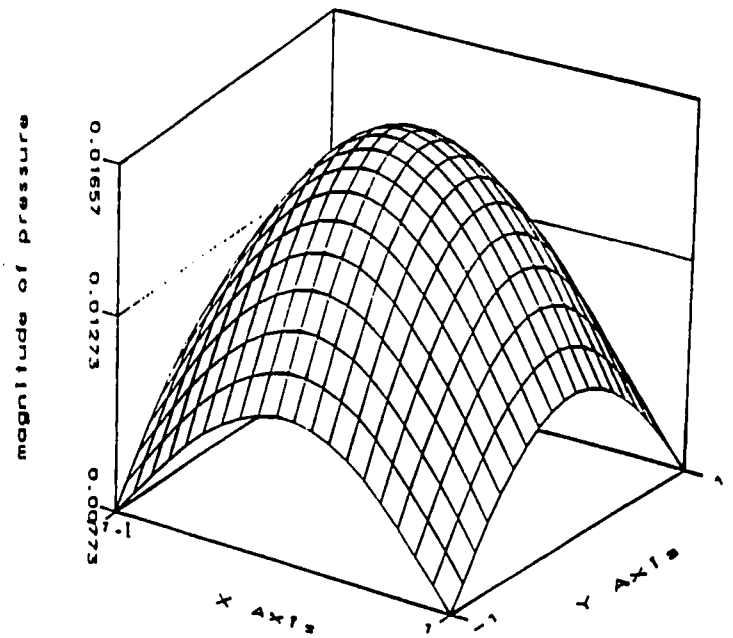

Figure 2.9: Analytic result of pressure distribution for a point source near an infinite rigid plane in free field.

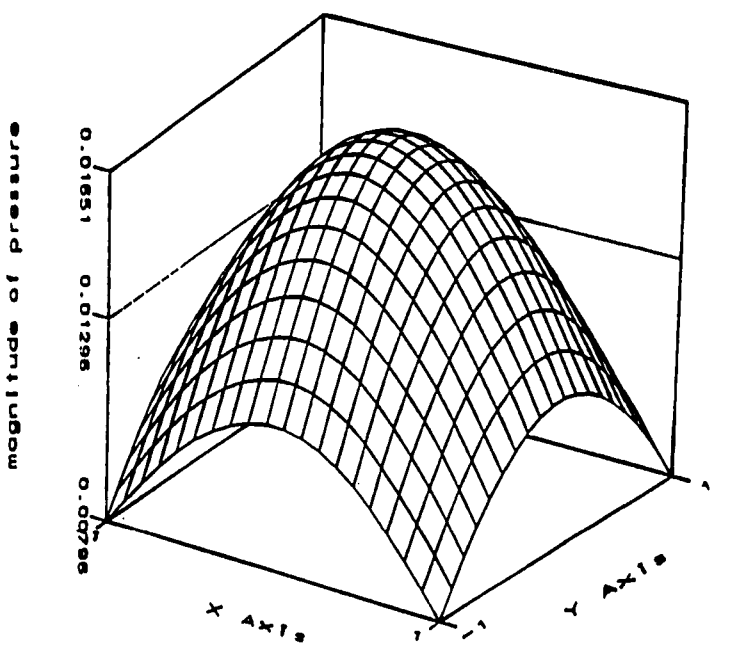

Figure 2.10: IBEM result of pressure distribution for a point source near a 10m by 10m rigid plate with 20x20 boundary elements.

are in agreement with the analytical results. In this example, the dimensions of the boundary elements were 0.5m×0.5m. The leading dimension was less than one-third of the acoustic wave length of approximately 1.7m at this frequency. In a second test simulation, the infinite plane was replaced by a 20m×20m finite surface while remaining a 20×20 element grid. Results for this case are shown in Figure 2.11. A comparison of Figure 2.11 with Figure 2.9 reveals a significant deterioration in the numerical predictions over the previous case. This is because the dimension of an element, which is 1m×1m for this discretization, is greater than half the wave length (1.7m) of the driving frequency. Theoretically, the smaller the boundary elements, the more accurate the numerical results will be. Of course, smaller element sizes increase the number of elements required to represent a given boundary with correspondingly increased computational time. Other researchers have found that in order to obtain good approximations using the boundary element method, the leading dimension of a boundary element should be less then one-third to one-quarter of the wavelength of the driving frequency. When a 25×25 element discretization was used for this surface, the numerical predictions are as shown in Figure 2.12. Although the leading dimension of the element is still greater than one-third of the wave length, the numerical result shown in Figure 2.12 is very close to the theoretical one shown in Figure 2.10 and is much better than the one shown in Figure 2.11. It can be seen from these results that the ratio of acoustic wave length to leading dimension of the boundary elements has significant influence on the accuracy of the numerical prediction using the boundary element method.

2.4.3 Pulsating sphere in a free field

The example investigated here is radiation from a pulsating sphere with uniform normal surface velocity into a free field. A pulsating sphere with radius 0.1m was positioned at (0, 0, 0). The driving frequency was 200Hz. Four hundred field points were distributed

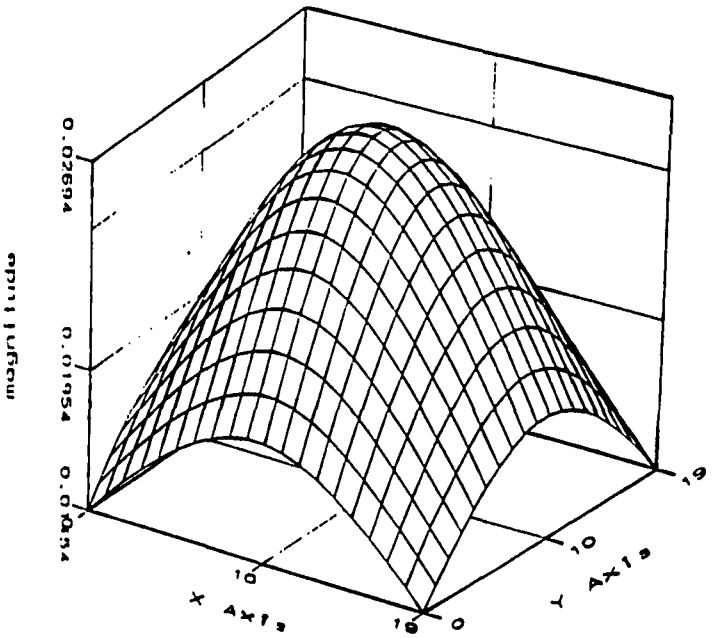

Figure 2.11: IBEM result of pressure distribution for a point source near a 20m by 20m rigid plate with 20x20 boundary elements.

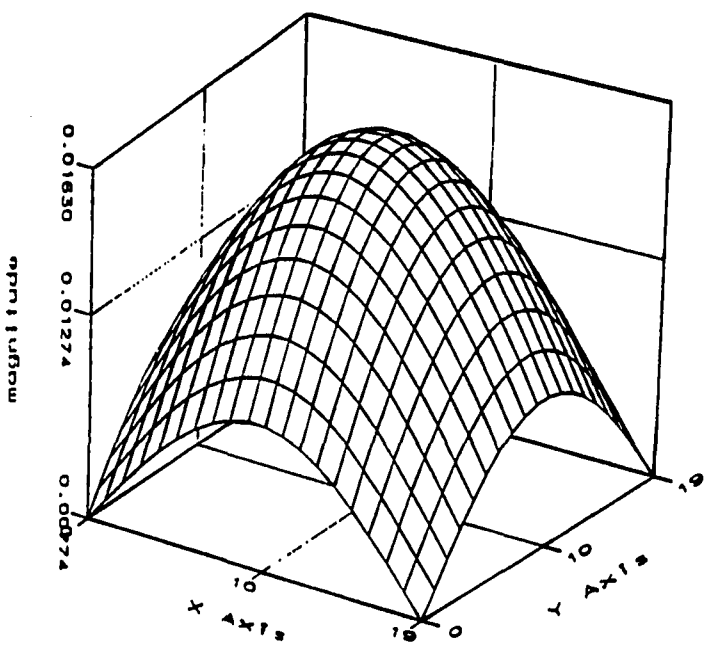

Figure 2.12: IBEM result of pressure distribution for a point source near a 20m by 20m rigid plate with 25x25 boundary elements.

uniformly on the plane surface -1m≤x≤1m, -1m≤y≤1m and z=3m. The analytical solution for acoustic pressure in a free field outside a pulsating sphere is given by [38]

$$p(r) = -\frac{jp\omega a^2 u_s}{r(1-jka)} e^{ikr} \tag{2.41}$$

where ρ is the density of the medium, ω the angular frequency, a the radius of the pulsating sphere, r the distance from the center of the pulsating sphere to the field point and u_s the normal surface velocity of the pulsating sphere. With $u_s = 1 m/s$, the magnitude of the resulting pressure distribution is plotted in Figure 2.13.

In the numerical simulation, the surface of the pulsating sphere is discretized into 72 elements. For the boundary condition $u_n = 1 m/s$ on each boundary node, the numerical prediction is shown in Figure 2.14. Good agreement between the analytical solution and numerical result is observed from the plots in Figures 2.13 and 2.14. The relative error is only 1.66% for both maximum value and minimum value.

2.4.4 Pulsating sphere near an infinite rigid plane

Another example using a pulsating sphere as a source is a pulsating sphere placed near an infinite rigid plane. The infinite plane was defined by z=0. A pulsating sphere with radius 0.1m was located at (0, 0, 0.5). The driving frequency was 200Hz. Four hundred field points were uniformly distributed on the plane surface -1m≤x≤1m, -1m≤y≤1m and z=3m. As in the point source case, an image pulsating sphere can be used to replace the effect of the infinite rigid plane. With the image source located at (0, 0, -0.5), the acoustic pressure at any field point is a combination of the contribution of the physical pulsating sphere and the image source. The theoretical solution for this combination can be represented by

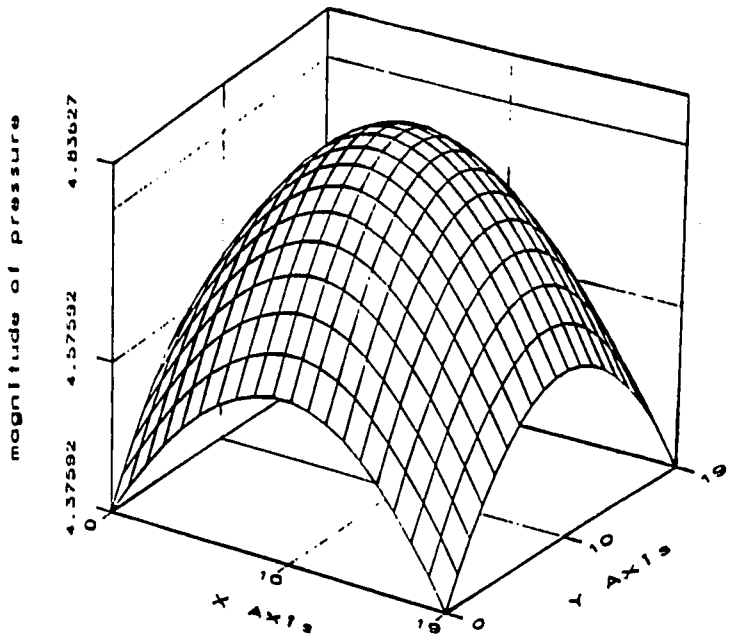

Figure 2.13: Analytic result of pressure distribution for a pulsating sphere source in free field, f=200Hz.

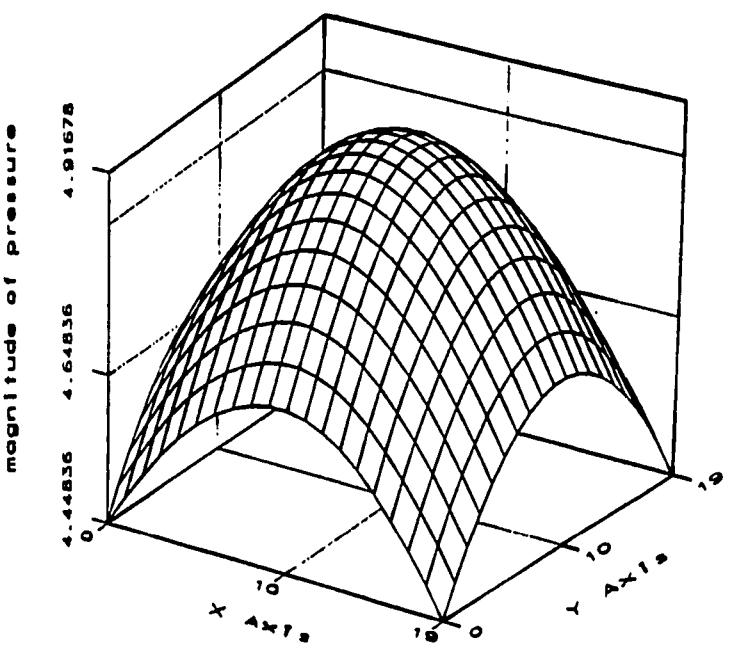

Figure 2.14: IBEM result of pressure distribution for a pulsating sphere source in free field with normal velocity boundary condition and 72 boundary elements, f=200Hz.

$$p(R,R') = -\frac{jr\omega a^2 u_s}{1-jka}\left[\frac{1}{R}e^{jkR} + \frac{1}{R'}e^{jkR'}\right] \tag{2.42}$$

where R is the distance from the center of the physical source to the field point of interest and R' the distance from the center of image source to the same field point. For $u_s = 1^{m}/_{s}$, the magnitude of the pressure distribution obtained from equation 2.42 on the observation surface is plotted in Figure 2.15.

In the numerical prediction of the pressure distribution, 72 elements were used to approximate the pulsating sphere surface. The infinite rigid plane was replaced by a zero thickness finite plate with dimensions 10m×10m. The plate was divided into a 20×20 element grid in the x and y directions, respectively. The boundary condition used was $u_n = 1^{m}/_{s}$ for each node on the surface of the pulsating sphere and $u_n = 0$ for the nodes on the plate. Figure 2.16 contains the numerical predictions for this case. It can be seen that the numerical predictions in Figure 2.16 are in good agreement with the analytical results in Figure 2.15. The relative error is 2.38% for the maximum value and 4.68% for the minimum value. If more accurate results are desired, more boundary elements could be added to refine the discretization.

2.4.5 Acoustic response in a spherical cavity

In this example, the interior field of a pulsating sphere was investigated. If the surface of a spherical cavity of radius a pulsates radially with a uniform velocity $u_n = 1^{m}/_{s}$, the analytical solution for the velocity potential at a distance r from the center of the cavity is [44]

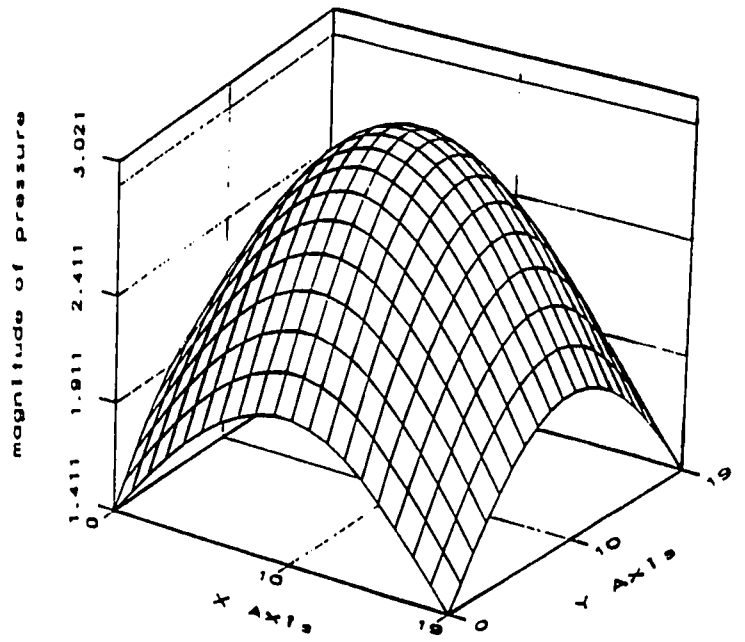

Figure 2.15: Analytic result of pressure distribution for a pulsating sphere source near an infinite rigid plane, f=200Hz.

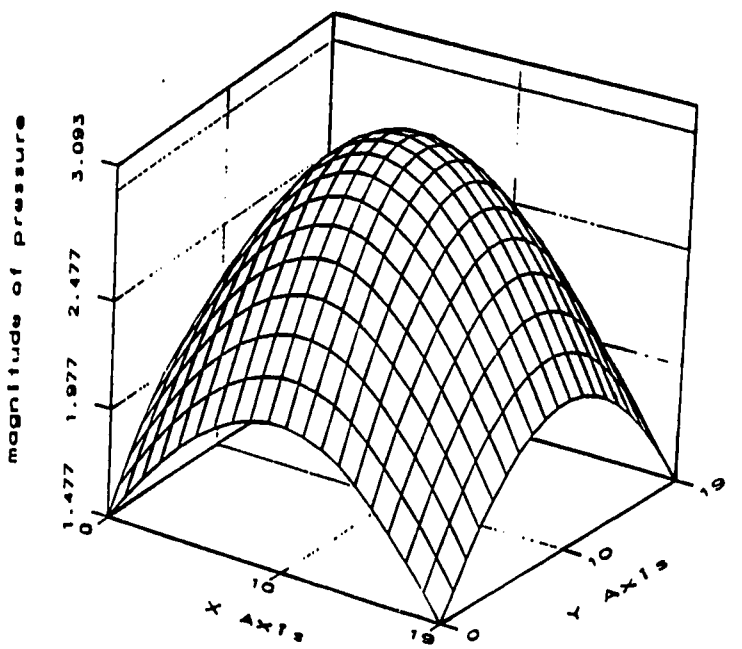

Figure 2.16: IBEM result of pressure distribution for a pulsating source near a 10m by 10m rigid plate with 20x20 boundary elements, f=200Hz.

$$\phi(r) = \frac{ka^2}{ka\cos(ka) - \sin(ka)}\left[\frac{\sin(kr)}{kr}\right] \tag{2.43}$$

where ϕ is velocity potential, a the radius of the cavity and k the wave number. At the center of the sphere, i.e., r=0, equation (2.43) becomes

$$\phi(r) = \frac{ka^2}{\cos(ka)[ka - \tan(ka)]} \tag{2.44}$$

and the velocity potential is only a function of ka. For $ka = n\pi$, where n=1, 2, 3 ···etc., the magnitude of ϕ is equal to a, the radius of the pulsating sphere. When $\tan(ka)=ka$, the magnitude of ϕ will be infinite.

The analytical solution for a spherical cavity pulsating with a uniform ϕ=1 at $r=a$ is

$$\phi(r) = \frac{ka}{\sin(ka)}\left[\frac{\sin(kr)}{kr}\right] \tag{2.45}$$

ϕ will be infinite when ka=nπ where n=1, 2, 3 ···etc.

In the numerical model, the surface of the spherical cavity was discretized into 72 elements. Both $\phi = 1$ and $\frac{\partial\phi}{\partial r} = 1$ were used as boundary conditions. Numerical predictions and analytical results are shown in Figures 2.17, 2.18, 2.19 and 2.20 for a=1, r=0 and r=0.5, respectively. Good agreement between boundary element method predictions and theoretical results was obtained for all cases except at certain frequencies where the boundary integral equation failed to have a unique solution [39].

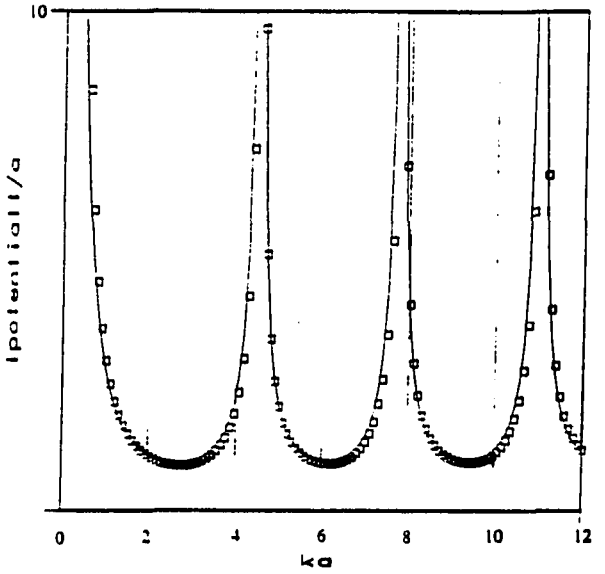

Figure 2.17: $|\phi|/a$ at r=0 vs ka for $(\partial\phi/\partial r)_{r=1}=1$, solid line: analytical result; □: IBEM prediction with 72 boundary elements.

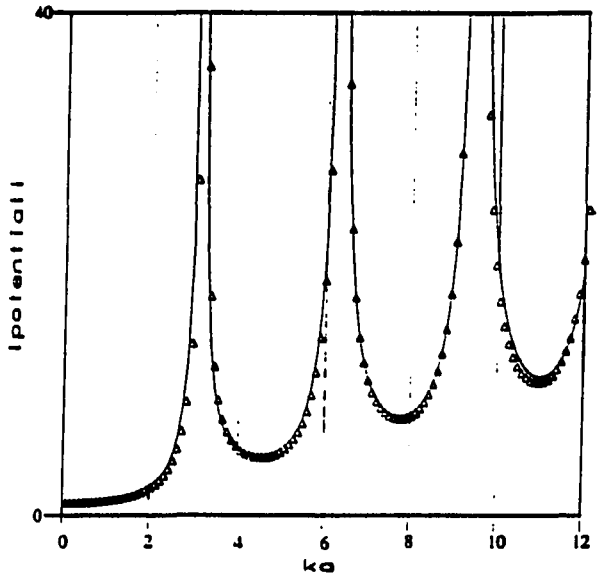

Figure 2.18: $|\phi|/a$ at r=0 vs ka for $(\phi)_{r=1}=1$, solid line: analytical result; Δ: IBEM prediction with 72 boundary elements.

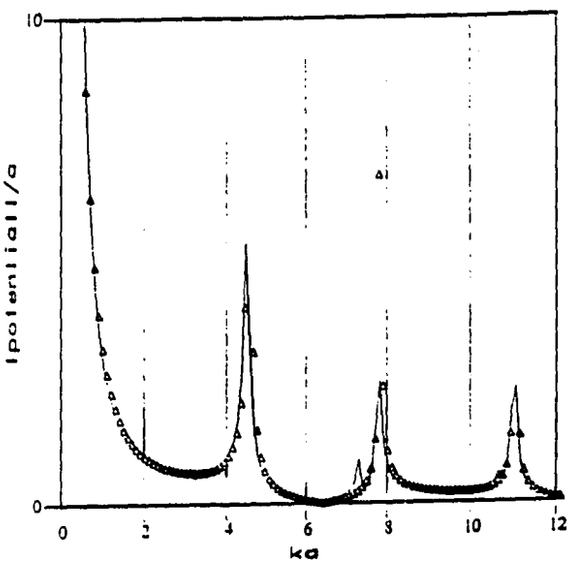

Figure 2.19: $|\phi|/a$ at r=0.5 vs ka for $(\partial\phi/\partial r)_{r=1}=1$, solid line: analytic result; Δ: IBEM result with 72 boundary elements.

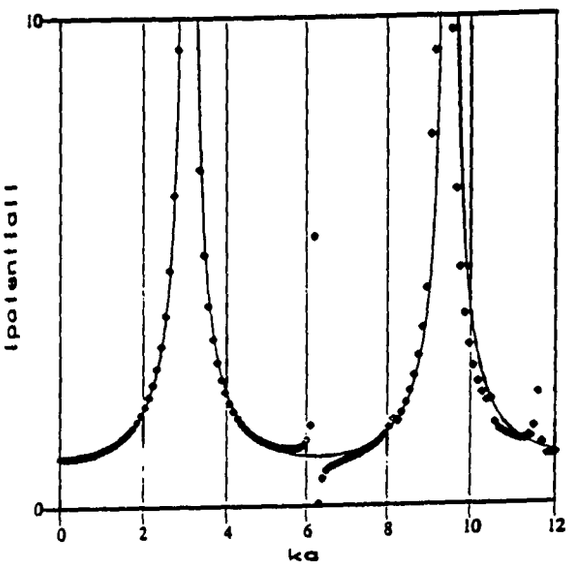

Figure 2.20: $|\phi|/a$ at r=0.5 vs ka for $(\phi)_{r=1}=1$, solid line: analytical result; $\Diamond$: IBEM prediction with 72 boundary elements.

2.4.6 Resonant frequencies of a rectangular cavity

All the examples presented heretofore in this chapter have been for point sources or spherical sources with smooth geometric boundaries. Corners and edges are known to create difficulties for the boundary element method due to the geometric boundary discontinuities. A method to circumvent difficulties associated with geometric boundary discontinuities has been described in section 2.2.4. To investigate the proposed method, the acoustic response of a rectangular cavity with dimensions 4m×5m×3m in the x, y and z directions, respectively, was simulated. One wall of the cavity was driven while the remaining five walls were rigid as shown in Figure 2.21. A simplistic analytical approach for this problem is to consider the problem on a one-dimensional basis as a driven/closed cavity. The approximate pressure solution for this problem, if considering only modes in the y-direction, is

$$p(y) = Ae^{jk(L-y)} + Be^{-jk(L-y)} \tag{2.46}$$

where L is the length of the cavity in the direction normal to the driven end, A and B the constants determined by the boundary conditions and y a position variable ranging from 0 to L. The boundary condition are that the velocity at the closed end is zero and at the driven end is v_0, a non zero value. With these boundary conditions, the approximate analytical solution [45] for equation (2.46) can be written as

$$p(y) = -j\rho c v_0 \frac{\cos[k(L-y)]}{\sin(kL)} \tag{2.47}$$

A point at y=0.1m is selected as a reference point to calculate the magnitude of the pressure. The resonant frequencies in the y direction can be determined from the peak on the

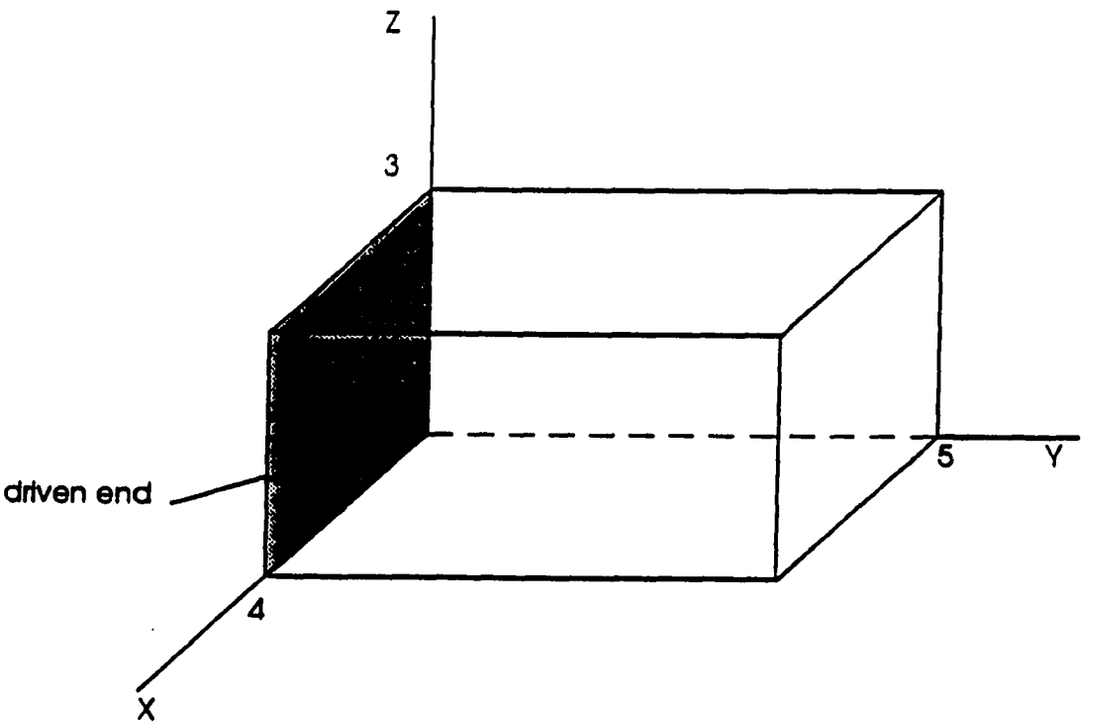

Figure 2.21: Configuration and the dimensions of the rectangular cavity.

plot of pressure versus wave number k. The resulting pressure magnitude versus k for this case is plotted in Figure 2.22.

The exact expression [42] for the resonant frequencies in an idealized three dimensional rectangular cavity is

$$k(l,m,n)=\sqrt{\left(\frac{l\pi}{L_x}\right)^2+\left(\frac{m\pi}{L_y}\right)^2+\left(\frac{n\pi}{L_z}\right)^2} \tag{2.48}$$

where L_x, L_y and L_z are dimensions in the x, y and z directions, respectively, l , m, n = 0, 1, 2, ··· etc, the order of resonant mode in the x, y and z directions. For this special case with m=0, n=0 and L=5m, equation (2.48) becomes

$$k(l)=\frac{l\pi}{5} \tag{2.49}$$

The first four resonant wave numbers are listed in Table 2.1.

For the numerical model, the boundary was discretized into 94 elements with 384 boundary nodes. Figure 2.23 contains the numerical predictions of pressure magnitude versus

Table 2.1: Resonant wave number

l	1	2	3	4
k (analytical)	0.628	1.257	1.885	2.513
k (numerical)	0.630	1.252	1.881	2.515

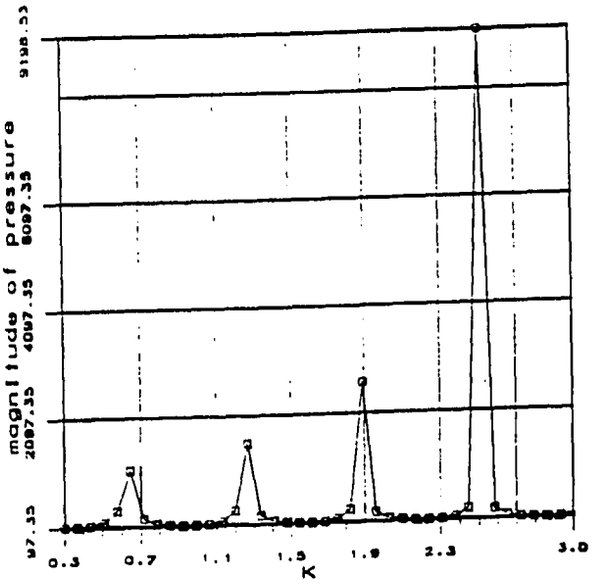

Figure 2.22: Analytical result of magnitude of pressure in the y direction vs. wave number.

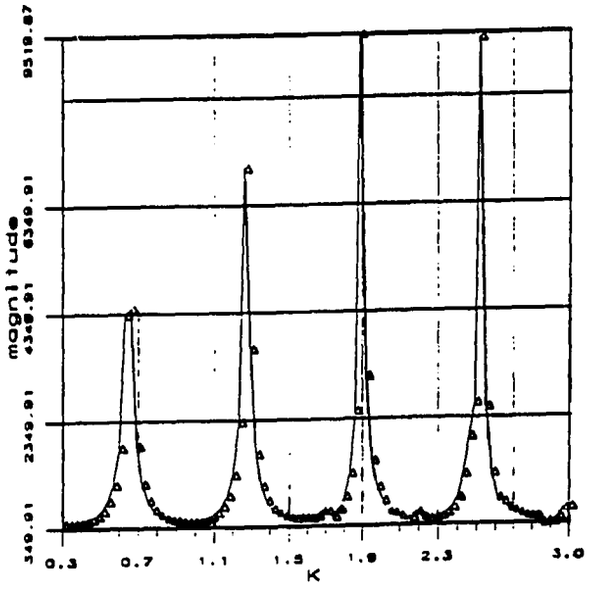

Figure 2.23: IBEM result of magnitude of pressure in the y direction vs. wave number, using 94 boundary elements.

k. From Figures 2.22, 2.23 and Table 2.1, it can be seen that excellent agreement was obtained for the resonant frequencies.

2.4.7 Pressure distribution inside a rectangular cavity

In this example, the cavity configuration and boundary conditions were the same as in the previous case. Sixty field points were distributed uniformly in the y direction from 0 to 5m. With $v_0=1^{m}/_{s}$ in equation (2.47), the pressure distribution as a function of y was investigated for wave numbers, k=1, 2 and 3. Figure 2.24 contains the numerical predictions and the analytical results for the case k=1. In the numerical approximation, the boundary of the cavity was discretized using 94 elements with 384 boundary nodes. The acoustic wave length for this case was $\lambda = 6.28m$ and the leading dimension of the boundary element was 1m (less than one sixth of the acoustic wave length). When k=2, the acoustic wave length was $\lambda = 3.14m$. The same boundary discretization as for the k=1 case was used and the predictions are plotted in Figure 2.25. For the k=3 case, the acoustic wave length was $\lambda = 2.09m$ and more boundary elements were required to meet the criterion mentioned earlier. A discretization using 376 boundary elements with 1326 boundary nodes was implemented for this wave number and the numerical predictions are shown in Figure 2.26 along with the corresponding analytical solution.

Comparisons of numerical predictions with analytical results in Figures 2.24, 2.25 and 2.26 reveal very good agreement for all cases. This good agreement also suggests that the method used to deal with corner and edge points is successful and satisfactory.

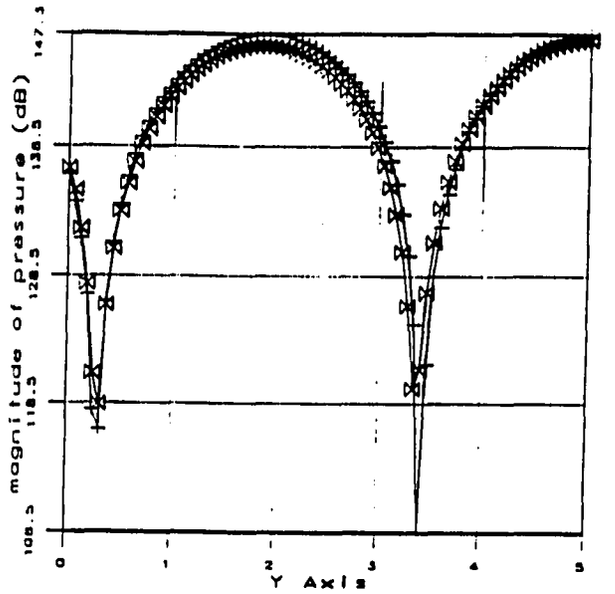

Figure 2.24: Magnitude of pressure in the y direction for k=1, +: analytical result, ∞: IBEM prediction with 384 degrees of freedom.

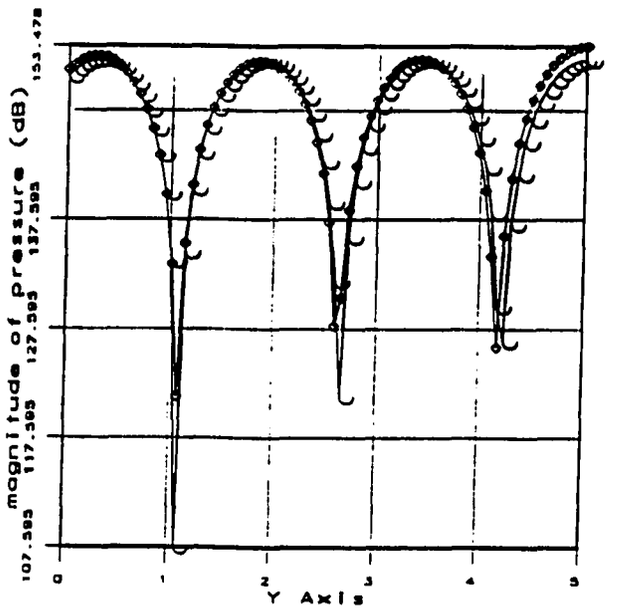

Figure 2.25: Magnitude of pressure in the y direction for k=2, ∪: analytical result, ◊: IBEM prediction with 384 degrees of freedom.

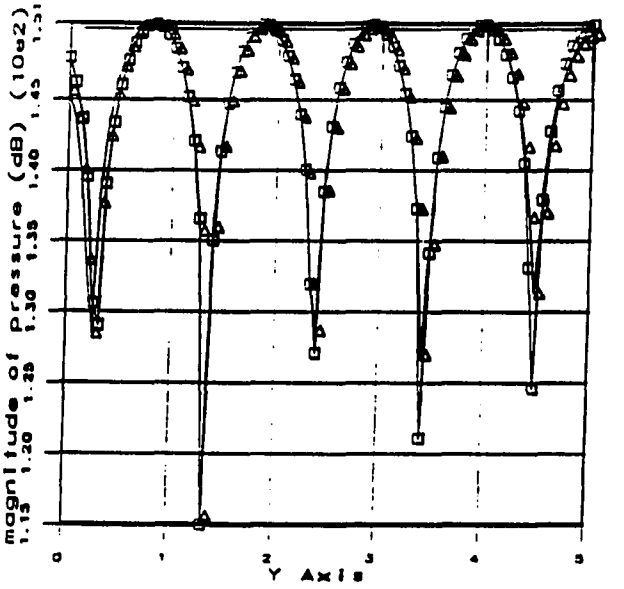

Figure 2.26: Magnitude of pressure in the y direction for k=3, □: analytical result, Δ: IBEM prediction with 1326 degrees of freedom.

2.5 Summary

In this chapter, the boundary integral equation and a numerical implementation, the indirect boundary element method, have been described for time harmonic acoustic problems. The boundary integral formulation of the problem and its regularization for numerical implementation were discussed in detail. The surface integral was transformed into a set of linear algebraic equations by discretizing the surfaces of the boundary and the sources. The matrix form of the resulting set equations was solved using standard LINPACK routines. A method to handle discontinuities in boundary geometry was presented and verified. A relationship between minimum leading dimension of the boundary element and the corresponding acoustic wave length as well as computational requirements were discussed and verified. Point sources and pulsating spheres were used as acoustic sources for validation studies because of the availability of analytical solutions for these simple sources. Various examples, interior and exterior radiation problems with essential and natural boundary conditions, have been investigated to verify the accuracy and effectiveness of the numerical implementation. By comparing numerical predictions with the analytical solutions, it has been shown that the IBEM implementation gives accurate predictions of acoustic fields for different sources and boundary conditions in free space, half space and cavities.

CHAPTER 3. OPTIMIZATION OF SECONDARY SOURCES

3.1 Introduction

Active noise cancellation in a region of interest normally becomes feasible after the acoustic radiation pattern from the primary sources has been determined. A number of secondary sources are then added into the system to attenuate the noise field by generating a destructively interfering field. The combination of the two acoustic fields results in a region of near silence. According to Huygen's principle, an infinite number of perfect point sources would be required to create a Huygen's surface that would generate a perfectly destructive acoustic field. However, this ideal Huygen's surface is impossible to achieve either practically or computationally. A compromise approach proposed in this chapter uses a finite number of optimized secondary sources to achieve "optimal" reduction of the noise level in a selected region.

After the number of secondary sources has been specified, their optimization generally involves two parameters, optimal locations and optimal complex strengths. Additional parameters, such as the number of secondary sources, could also be optimized in some sense, but such optimization is not included in this investigation. The primary focus of this research is to develop a systematic approach for obtaining numerical estimates of optimal secondary source locations. After the optimal secondary source locations have been found, the

secondary source strengths are then optimized by minimizing the mean square pressure at selected observation points.

3.2 Optimization of the Number of Secondary Sources

The primary sound field in any domain is the result of the acoustic noise sources and the effects of the domain boundaries. An attempt to actively cancel the primary sound field involves the addition of secondary sources to the system. Thus, the system generally contains the following parameters that are related to optimal active noise cancellation:

- The locations of observation points
- The number of secondary sources
- The locations of secondary sources
- The complex strengths of secondary sources

If all these parameters are included in the consideration of optimal active noise control, the control function will be very complicated and some of the parameters could lead to intractable nonlinear equations. The objective of this investigation is to find a simple, feasible, and systematic approach to achieve approximately optimal active noise cancellation. The IBEM technique or, to be more specific, the fictitious source strength distribution on the boundary of the domain, is employed to accomplish this objective. After locating the observation points, the optimization of active noise cancellation is reduced to optimization of the secondary sources, which involves three parameters--locations, complex strengths and number of secondary sources. Among these parameters, the order of optimization is also an important consideration.

Optimization of the number of secondary sources is not a focus of this research. In this work, selection of the number of secondary sources is secondary to the optimization of

the locations and complex strengths of the secondary sources. With an initial number of secondary sources, usually two or three depending on the primary acoustic field, optimal active noise cancellation can be obtained by optimizing secondary source locations and complex strengths. One or two additional secondary sources are then incorporated into the system. By iterating and checking the convergence of the noise reduction after each iteration, the optimal number of secondary sources can be obtained approximately. Numerical results suggest rapid convergence to an optimal number of secondary sources. Active cancellation is usually maximized after the addition of only a small number of secondary sources, and further reductions for increased numbers of secondary sources are negligible.

3.3 Optimization of the Locations of Secondary Sources

In order to optimize the strengths and phases of secondary sources, their locations must be specified. It is highly desirable, if not essential, that optimal secondary source locations be estimated before optimization of their complex strengths since the locations effect the optimal secondary source strengths. In addition, the objective of noise control within common three-dimensional cavities is often to attenuate the dominant resonant modes. If the position of a secondary source happens to be at a nodal point of a dominant resonant mode, it will not contribute to the cancellation of that mode. When a secondary source is placed near a nodal point of a resonant mode, a very large magnitude of the secondary source strength, probably unreasonably large, is likely to be required for the optimization. For some cases, although the dominant mode may be suppressed, other resonant modes could be excited by the secondary sources and the total sound pressure level may actually increase, instead of being attenuated, due to improper locations of secondary sources. Determination of appropriate secondary source locations is thus a critical step in active noise control.

The primary contribution of this research is to take advantage of the fictitious source distribution on the Huygen's surface, i.e., on the boundary of the domain, to estimate optimal locations for secondary sources. In equation (2.37), the vector σ contains the fictitious source strength at each boundary node. The velocity potential, as well as the acoustic pressure and particle velocity at any field point is the result of contributions from the primary sources, φ_s, and the fictitious source distribution used to represent the effect of the boundary Γ. This means that boundary nodes with higher fictitious strengths make greater contributions to the field points than those with smaller source strengths. This also implies that secondary sources placed at locations of boundary nodes with higher fictitious source strengths will be more effective and efficient for active noise cancellation. In this work, secondary sources are physically modeled as small baffled pistons mounted at the locations of selected boundary nodes. In this approach, only boundary nodes can be candidates for locations of secondary sources. This restriction is a potential disadvantage of the approach, but actual detrimental effects are limited since optimization is relatively insensitive to the specific choice of high fictitious strength nodes as will be seen in next chapter.

Dealing with interior acoustic problems is a bit different from exterior problems because of interior resonant modes. For global control of interior acoustic noise, besides the locations of high fictitious strengths, an additional criterion for optimal locations of secondary sources is to avoid the excitation of resonant modes. In cases of low modal density, knowledge of the primary field and modal density distribution in the cavity make it possible to estimate optimal secondary source locations using multiple candidates of high fictitious source strength nodes to avoid the excitation of resonant modes.

For high frequency excitation, it is difficult to find optimal secondary source locations to achieve global active noise suppression in an enclosed cavity because of the high modal density. Thus, for high modal density cases, local control in a selected region is probably the

better choice, and the high fictitious source strength is the only criterion necessary for estimating optimal locations of secondary sources.

3.4 Optimization of the Strengths of Secondary Sources

The primary sound field in an enclosure is the result of the noise sources and the boundary effect. After optimal locations for secondary sources have been estimated, the system is usually composed of four parts: boundary with well-posed boundary conditions, primary sources with known locations and strengths, observation points and secondary sources with known locations and unknown strengths. Thus, the only unknown parameter, the strength of the secondary sources, can then be optimized. The approach used here to optimize the secondary source strengths is minimization of the sum of the squared pressures at selected observation points. The approach is to monitor the amplitude of pressure fluctuations at the observation points and to adjust the strengths of the secondary sources to minimize the sum of the squared pressure amplitudes at these locations. The mathematical expression of this approach is

$$\Omega = \sum_{i=1}^{n_{obp}} |p_i|^2 w_i \tag{3.1}$$

where Ω is the control function, p_i the pressure at i-th observation point, w_i the weighting factor at i-th observation point and n_{obp} the total number of observation points. Equation (3.1) can be rewritten in matrix form as

$$\Omega = [p^H][W][p] \tag{3.2}$$

where p is a column vector containing the pressure at each observation point, p^H the Hermitian transpose of p and W a diagonal matrix of weighting factors at each observation point.

From equations (2.4) and (2.37), the pressure at observation points can also be expressed in matrix form as

$$[p_{obp}]=[E][\sigma]+[p_s] \tag{3.3}$$

where E is a coefficient matrix related to the geometry of the boundary and observation points, p_s a column vector containing the direct contribution from primary sources, p_{obp} a column vector of pressure at each observation point and σ a column vector of fictitious source strength at each boundary node. From equation (2.36), the σ vector can be expressed as

$$[\sigma]=[A]^{-1}[R] \tag{3.4}$$

and equation (3.3) can be written as

$$[p_{obp}]=[C][R]+[p_s] \tag{3.5}$$

where

$$[C]=[E][A]^{-1} \tag{3.6}$$

As has been mentioned earlier, in this research the secondary sources are modeled as baffled pistons located at selected boundary nodes. Physically, the secondary source strengths are the normal velocities of the baffled pistons. The objective of the optimization is actually to optimize the normal velocities at the selected boundary nodes, which can also be treated as the boundary conditions at the nodes. Vector R in equation (3.5) contains all the secondary source strengths to be optimized. After partitioning R to separate selected nodes from the rest, equation (3.5) can be rearranged as

$$[p_{obp}]=[C_2][q]+[D] \tag{3.7}$$

where q is a column vector containing the secondary source strengths that are to be optimized, C_2 the known coefficient matrix partitioned from C and

$$[D]=[p_s]+[C_1][R_1] \tag{3.8}$$

where C_1 is the coefficient matrix partitioned from C and R_1 the column vector partitioned from R.

Substituting equation (3.7) into the control objective function, equation (3.2) becomes

$$\begin{aligned}\Omega=&[D^H][W][C_2][q]+[q^H][C_2^H][W][D]\\&+[D^H][W][D]+[q^H][C_2^H][W][C_2][q]\end{aligned} \tag{3.9}$$

Ω in equation (3.9) is a real, positive definite quadratic function of secondary source strengths. It has been proven [46] that this type of function has a unique global minimum. So

there exists a unique optimal solution for the complex secondary source strengths that minimizes the sound pressure level at the selected observation points. By taking the partial derivative with respect to q, equation (3.9) becomes

$$\frac{\partial \Omega}{\partial q} = [D^H][W][C_2] + [q^H][C_2^H][W][C_2] \tag{3.10}$$

Equating the derivative to zero and using the identities of matrix operation, the optimized solution for q is

$$[q_o] = -[[C_2^H][W][C_2]]^{-1}[C_2][W][D] \tag{3.11}$$

By substituting D from equation (3.8) into the above equation, the final expression for optimal secondary source strengths is

$$[q_o] = -[[C_2^H][W][C_2]]^{-1}[C_2^H][W]([p_s] + [C_1][R_1]) \tag{3.12}$$

where q_o is the column vector containing optimized secondary source strengths.

3.5 Summary

In this chapter, the indirect boundary element method is employed to determine optimal locations for secondary sources. With the aid of the fictitious source distribution on the boundary, optimal locations of secondary sources can be estimated in a systematic way.

For exterior problems, the only criterion for deciding the optimal locations of secondary sources is the magnitude of fictitious source strengths. For some interior problems with low modal density, it is also critically important to avoid excitation of other resonant modes in order to achieve global reduction of sound pressure level. For interior problems with high modal density, where global control of the primary noise field is not feasible, local optimal control can be obtained by positioning the secondary sources at boundary nodes with higher fictitious source strengths.

CHAPTER 4. RESULTS OF ACTIVE NOISE CONTROL IN THREE-DIMENSIONAL SPACE

4.1 Introduction

In the previous two chapters, the IBEM and its numerical implementation for active noise control as well as a procedure for optimization of secondary sources were discussed in detail. In this chapter, the results of active noise control in three-dimensional space using the approach proposed in this research will be presented. These results include three-dimensional interior resonant mode problems as well as exterior radiation problems. The primary acoustical field is predicted using the IBEM. The criteria proposed in Chapter 3 are employed to estimate optimal locations for secondary sources and then the strengths of the secondary sources are optimized using the squared pressure criterion at selected observation points. Some of the results are compared with alternative numerical and experimental results from the archival literature.

For simplicity, acoustical point sources were used for all cases studied but the approach is easily extended to other acoustical sources. The geometric configurations of the boundary involved in the examples presented are rectangular prisms because of the visibility of mode shapes for interior problems and because of prior results that are available for comparison. As mentioned earlier, the IBEM is capable of dealing with any boundary configuration.

4.2 Global Control of the (1, 1, 0) Mode of a Rectangular Cavity

The first case presented is a replication of the work of Elliott and co-workers [47], for which both numerical and experimental results were presented by the authors. The original problem was active minimization of a harmonic sound field within a rectangular cavity with internal dimensions 0.668m×0.265m×0.05m, as shown in Figure 4.1. The dimensions of the cavity were chosen so that the natural frequencies of the mode were reasonably well spaced over the frequency range of interest. Also one dimension was much smaller than the others to ensure that only a two dimensional sound field was excited in the cavity over a reasonable frequency range. The cavity was made of 18mm medium density fiberboard. Dome loudspeakers with diameter of 20mm were used as the primary and secondary sources in the experimental model. The location of the center of each source is shown in Table 4.1. Elliott and coworkers obtained their numerical predictions by using the characteristic function approach with a damping ratio of 0.01 for all modes.

Several approximations were made in this replication.

- All the sources were replaced with point sources.

Table 4.1: Coordinates of the centers of loudspeakers in the experimental enclosure

source	x_1(m)	x_2(m)	x_3(m)
P	0.025	0.025	0.0
S_1	0.135	0.025	0.0
S_2	0.643	0.24	0.0

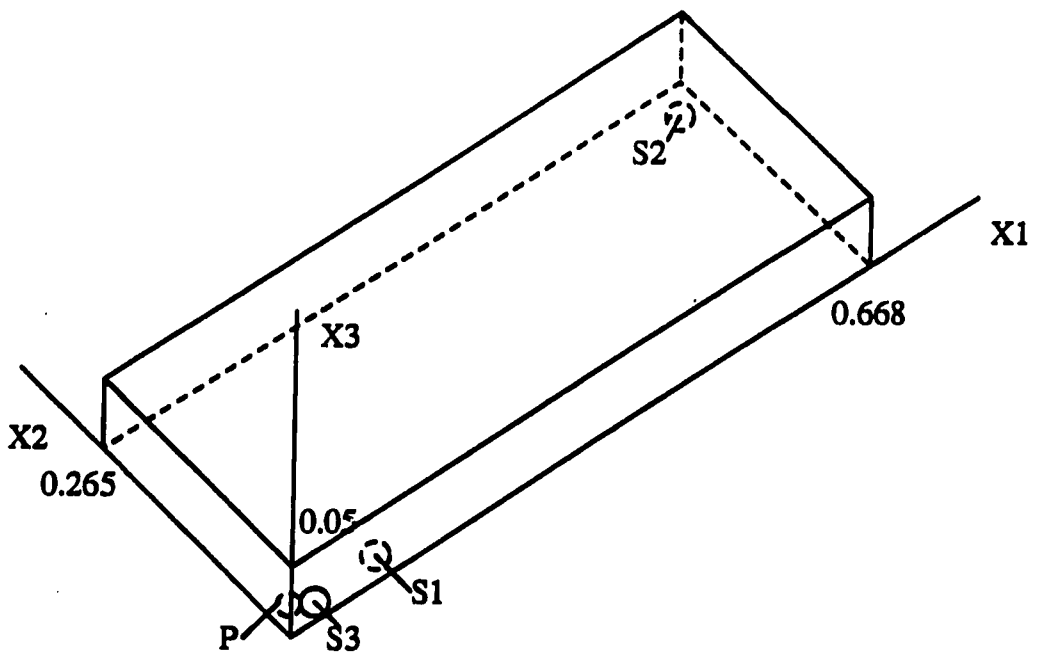

Figure 4.1: Enclosure configuration and the locations of sources.

- All the walls were assumed to be rigid.
- The locations of the primary source and secondary sources were shifted from the positions where Elliott and coworkers placed these sources because the locations of the sources have to be the locations of boundary nodes when the approach proposed in this investigation is employed.

  The location of each source is shown in Table 4.2.

Table 4.2: Coordinates of the sources in this replication

source	$x_1(m)$	$x_2(m)$	$x_3(m)$
P	0.02569	0.0106	0
S_1	0.1285	0.0106	0
S_2	0.6423	0.2544	0
S_3	0.02569	0	0.01

The objective of this example is to cancel the (1, 1, 0) dominant resonant mode inside the cavity. With the rigid wall approximation, the resonant frequency of this mode can be calculated using [42]

$$f(l,m,n) = \frac{c}{2\pi}\sqrt{\left(\frac{l\pi}{L_x}\right)^2 + \left(\frac{m\pi}{L_y}\right)^2 + \left(\frac{n\pi}{L_z}\right)^2} \tag{4.1}$$

which gives f(1, 1, 0) = 696Hz. Elliott and co-workers obtained an experimental result of 680Hz and a numerical result of 692 Hz, thus the relative error caused by our approximations is acceptable.

Two hundred field points were distributed on the x_3=0.025m plane to investigate the pressure field within the cavity. Figures 4.2 contains the pressure distribution within the cavity for the primary source only. In Figures 4.2, 4.3 and 4.4, (a) is the result of Elliott and co-workers' numerical prediction, (b) is their experimental result and (c) is the numerical result obtained using the IBEM. In their investigation, two secondary sources were located at S_1 and S_2 respectively to obtain two different results for active noise cancellation of (1, 1, 0) mode. To replicate their results with the approach proposed in this investigation, two point sources were positioned at S_1 and S_2 respectively. One field point (0.663m, 0.26m, 0) was selected as the observation point for optimization of secondary source strengths. Figures 4.3 and 4.4 are plots of the replications of the active noise cancellation results. From Figures 4.2, 4.3 and 4.4, it can be seen that the numerical results obtained by the approach proposed in this research match very well with the experimental results as well as the numerical ones obtained using the characteristic function approach.

All the results presented thus far are replications of those obtained by Elliott and co-workers'. The great advantage of optimizing secondary source locations using the fictitious source strength distribution on the boundary has not been employed. Although around 10dB reduction was achieved by using secondary sources located at S_1 and S_2 respectively, there could be other even better locations for the secondary sources. Examination of the fictitious source strength distribution on each boundary wall revealed the maximum strength to be on the wall at x_2=0. The fictitious source strength profile on the wall is plotted in Figure 4.5. From Figure 4.5, it is obvious that the nodal location, S_3, has significantly greater fictitious source strength than other nodal locations. Probably this is because of its nearness to the primary source. To meet the fictitious source strength criterion for optimal location of secondary sources discussed in Chapter 3, this boundary node is an ideal location for a secondary source. To consider the secondary location criterion, the resonant frequencies

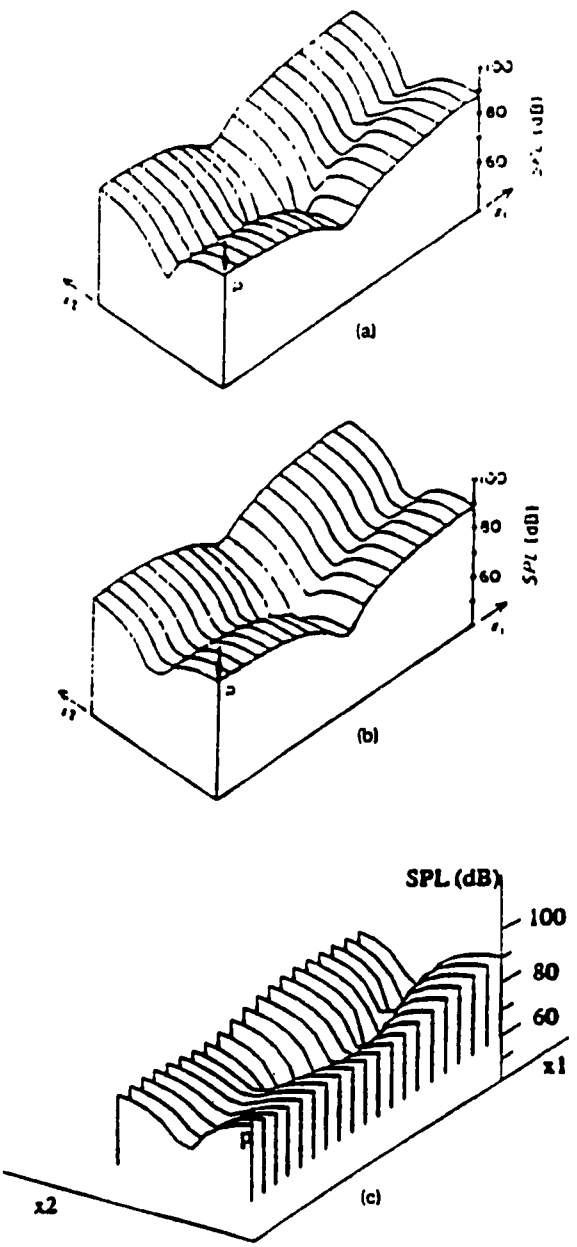

Figure 4.2: Pressure distribution of sound field without control, (a) numerical result using characteristic functions, (b) experimental result ((a) and (b) are from Elliot, et. al. [47]), (c) numerical prediction using IBEM.

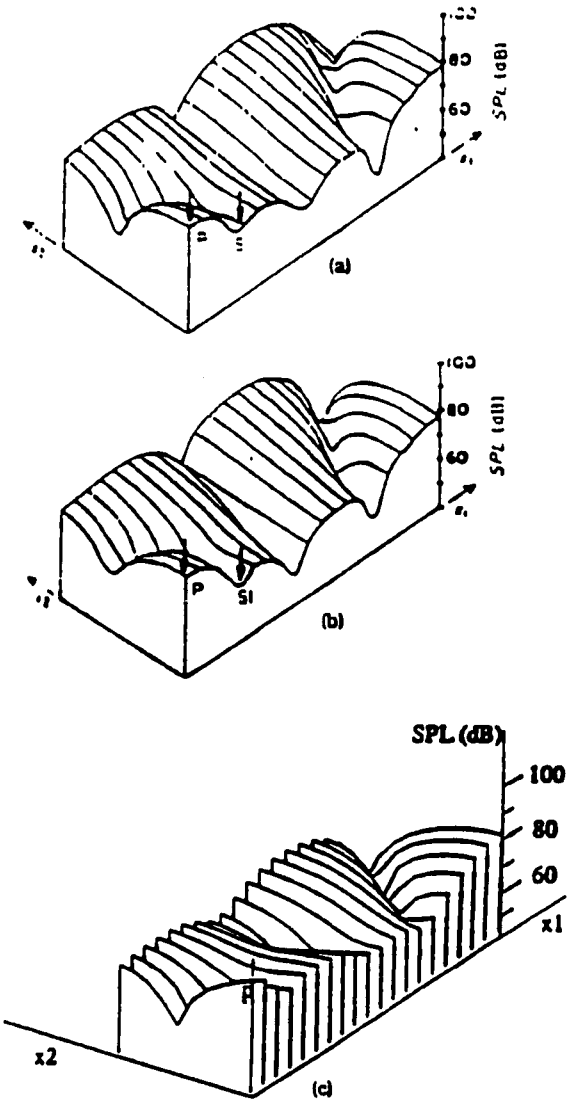

Figure 4.3: Pressure distribution of sound field with one secondary source located at S_1, (a) numerical result using characteristic functions, (b) experimental result ((a) and (b) are from Elliot, et. al. [47]), (c) numerical prediction using IBEM.

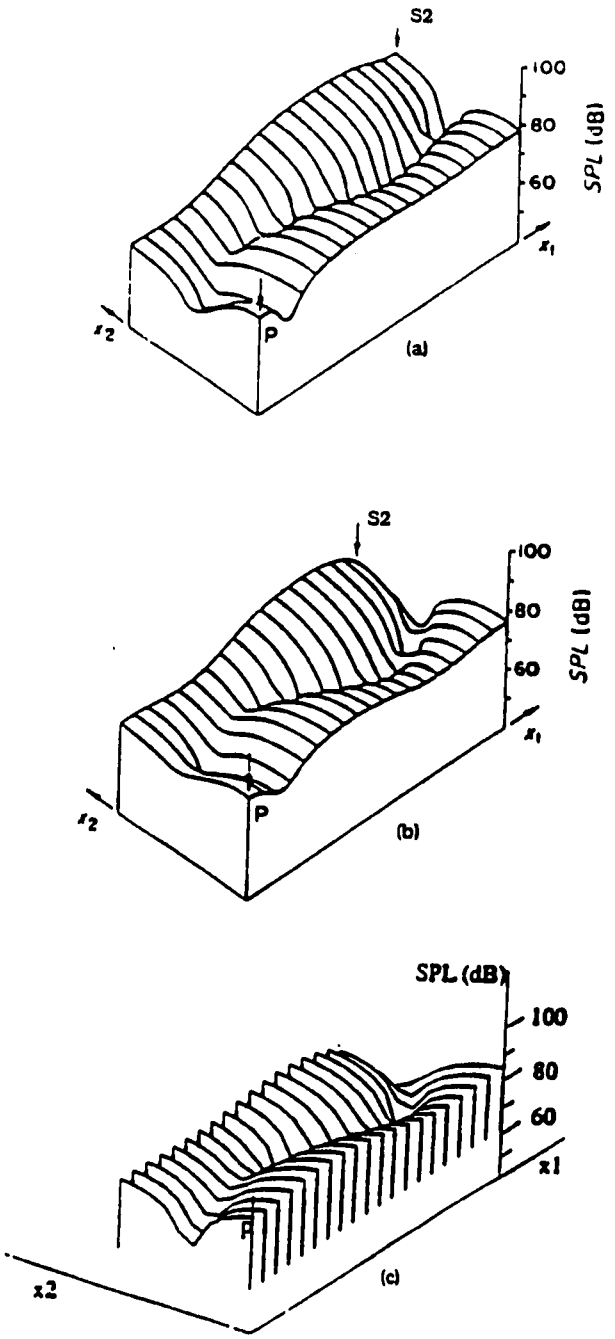

Figure 4.4: Pressure distribution of sound field with one secondary source located at S_2, (a) numerical result using characteristic functions, (b) experimental result ((a) and (b) are from Elliot, et. al. [47]), (c) numerical prediction using IBEM.

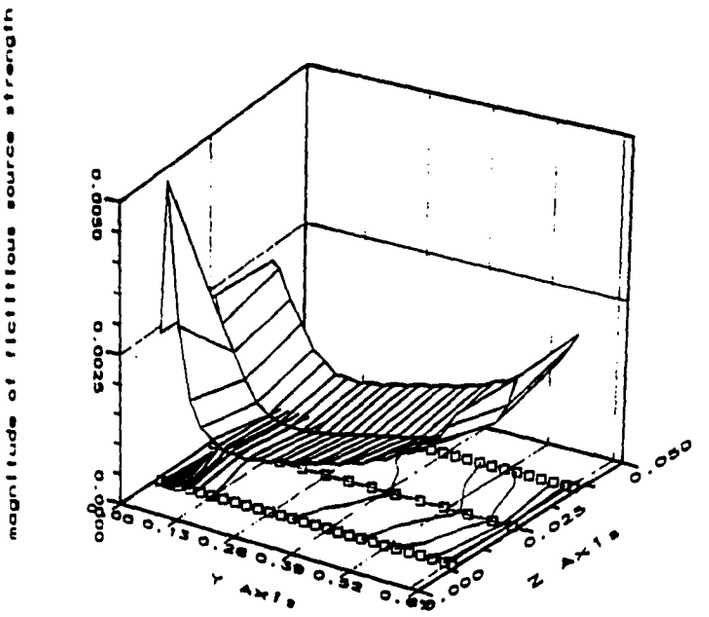

Figure 4.5: Fictitious source strength profile on the wall $x_2 = 0$.

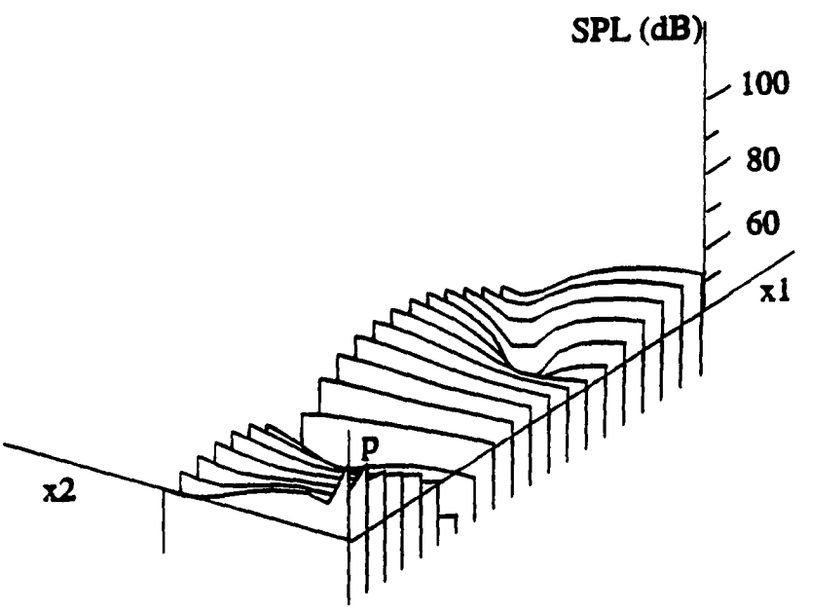

Figure 4.6: Pressure distribution of sound field with one secondary source located at S_3.

lower than the (1, 1, 0) mode, which could be excited by the secondary source, are listed in Table 4.3. These frequencies were calculated using equation (4.1). The next frequency above the (1, 1, 0) mode is 770Hz corresponding to the (0, 3, 0) mode, which will not be excited by a 696Hz secondary source.

Table 4.3: Resonant frequencies below the (1, 1, 0) mode

frequency (Hz)	257	513	647
mode	(0, 1, 0)	(0, 2, 0)	(1, 0, 0)

From Table 4.3, the only unwanted mode that could be excited by a secondary source at S_3 is (0, 2, 0) mode at a frequency of 513Hz. Since this frequency is not close to the driving frequency, the (0, 2, 0) mode should not be significantly excited by a secondary source placed at the nodal location denoted by S_3. Besides, the modal density near the driving frequency is quite low. Thus, S_3 could be a near optimal location for a secondary source. For this secondary source location, the optimal strength of the secondary source was calculated to be (0.0062m/s, 3.14rad) corresponding to magnitude and phase using the criterion described in Chapter 3. The resulting active noise cancellation using one secondary source located at S_3 is plotted in Figure 4.6. Comparing Figure 4.6 with Figures 4.3 and 4.4, around 30dB additional reduction is predicted for this optimal location of a secondary source and about 40dB attenuation has been obtained from the original pressure field shown in Figure 4.2.

From this example, good agreement between the IBEM results and experimental results as well as the numerical ones using characteristic functions can be observed. This good agreement suggests that not only the results of the IBEM computer program are satisfactory and accurate, but also that the code for optimization of secondary source strength

is reliable. Also, the much better result obtained by placing a secondary source at S_3 suggests that the approach presented in this investigation could be a good systematic method for estimating optimal locations for secondary sources.

4.3 Active Noise Control of Sound Radiation From a Rectangular Box

This example is another replication of previous work. Giordano and co-workers [48] presented results for active noise control of a three-dimensional extended radiator. The dimensions of the rectangular prism radiator were 760mm×600mm×457mm in the x, y and z directions, respectively, as shown in Figure 4.7. The sides of the box were 13mm thick aluminum. The top and bottom of the box were closed with 3mm thick steel plates. The two steel plates were clamped at their edges and were driven by electromagnetic shakers located within the box. The driving frequency was 63Hz, corresponding to the (1, 1) structural mode of the plates. The measured normal velocity distributions of the top and bottom plates are also plotted in Figure 4.7. The normal velocities on the sides of the box were assumed to be zero. In their investigation, 175 field points were distributed on a spherical surface located 10 wavelengths from the center of the box, which was about 54.9m from the center of the box. Figure 4.8 contains numerical predictions obtained by Giordano and co-workers using direct a boundary element method (DBEM) and an active noise control result obtained using four loudspeakers as secondary sources. The speakers were located at the corners of the top plate indicated by 1, 2, 3 and 4 in Figure 4.7. The IBEM prediction of primary pressure magnitude at field points is shown in Figure 4.9. Since three-dimensional polar graphic software was unavailable, the plot is a two-dimensional plane with 100 field points evenly distributed on a circle of radius 54.9m centered at the center of the box. Because no actual experimental data for the normal velocity distribution on the top and bottom plates was available, the normal

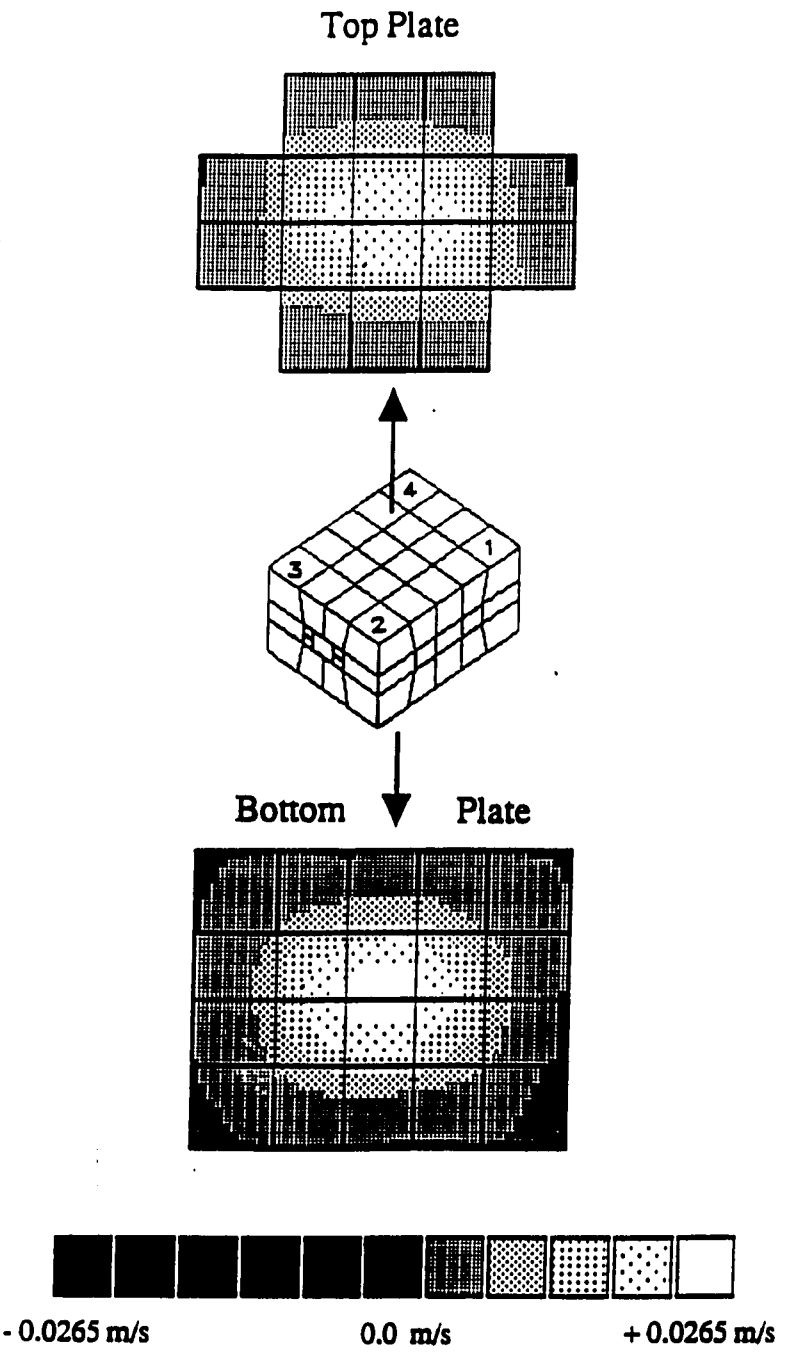

Figure 4.7: Configuration of a three-dimensional extended radiator and the measured normal velocity profiles on the top and bottom plates (from Giordano and co-workers [48]).

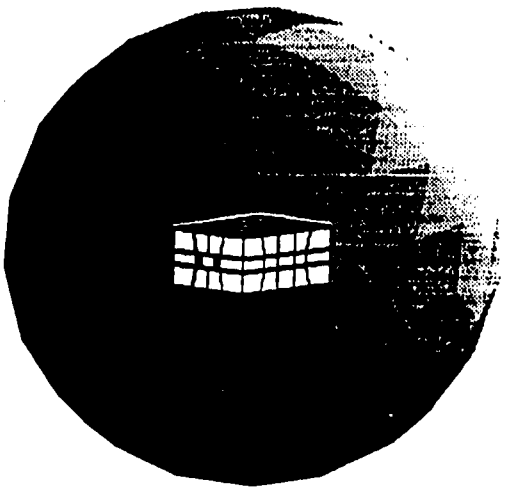

Plates Only

maximum = 46 dB

(a)

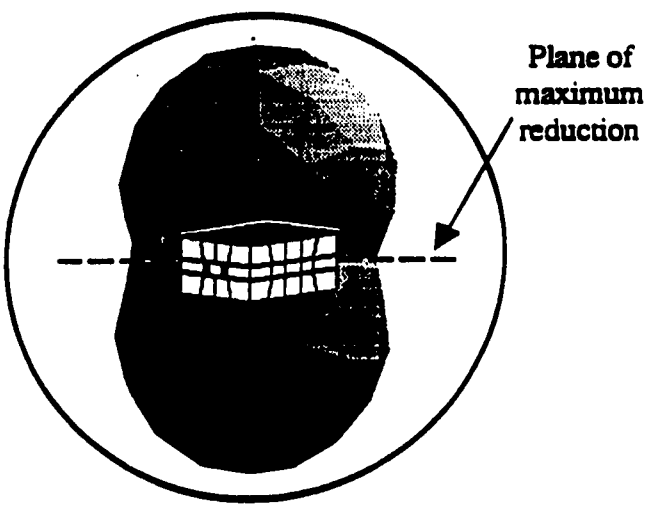

Plates + Active Sources

maximum = 40 dB

(b)

Figure 4.8: Numerical result of sound field using direct boundary element method, (a) primary field without control, (b) with active control (from Giordano and co-workers [48]).

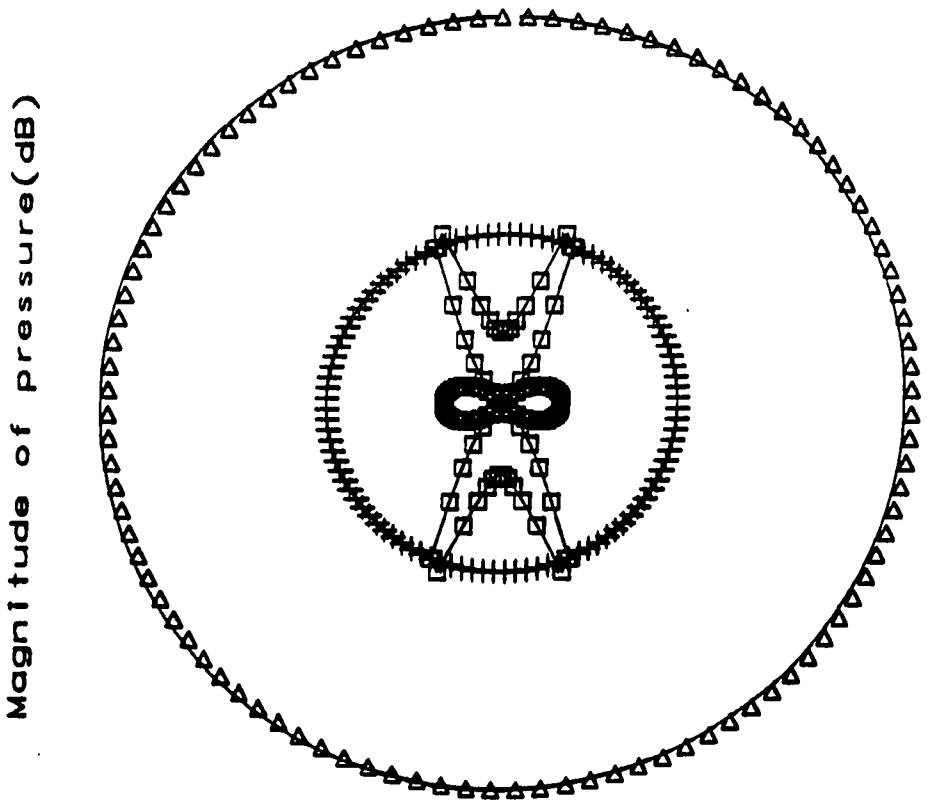

Figure 4.9: Pressure distribution of sound field, Δ: primary pressure level with maximum 48.8dB, □: after control using one secondary source with maximum 21.3dB.

velocity on the two plates used as boundary conditions for the IBEM prediction was approximated by linear interpolation of the velocity profiles given by Giordano and co-workers (Figure 4.7). The predicted pressure magnitude by the DBEM was 46dB and the IBEM prediction was 48.8dB. Giordano and coworkers did not present experimental results in their paper, but they mentioned that experimental results were consistently 3dB to 5dB above their numerical predictions. This implies that the IBEM result is very close to their experimental result. To determine optimal locations for secondary sources using the IBEM, the fictitious source strength distribution on the top and bottom plates are plotted in Figures 4.10(a) and 4.10(b) and maximum fictitious source strength was found to be at the center of the bottom plate. From Figure 4.10(b), it can be seen that there are three boundary nodal locations on the bottom plate having maximum fictitious source strength. All of them are candidate optimal locations for secondary sources since this is an exterior radiation problem. Two cases were considered to investigate active control of the radiated sound field.

For the first case, only one secondary source, positioned at the center of the bottom plate, was utilized. The optimal strength for this secondary source was found to be (0.48m/s, 3.14rad). The result of active control using this secondary source along with the primary pressure pattern is illustrated in Figure 4.9. The circle represented by Δs is the sound pressure level without active control. The pattern denoted by $\square$s is the result for active control and the circle represented by +s is a scale of 21.3dB. The maximum pressure level of 21.3dB indicates that more than 27.5dB attenuation was achieved in all the directions. Figure 4.9 also shows a strong directivity of the radiation pattern after control. This directivity pattern implies strong coupling between the secondary source and plate vibration.

Three secondary sources located at positions of maximum fictitious source strengths on the bottom plate were used for the second trial. Using the computer program for optimization of secondary source strength, the optimal strengths of these secondary sources

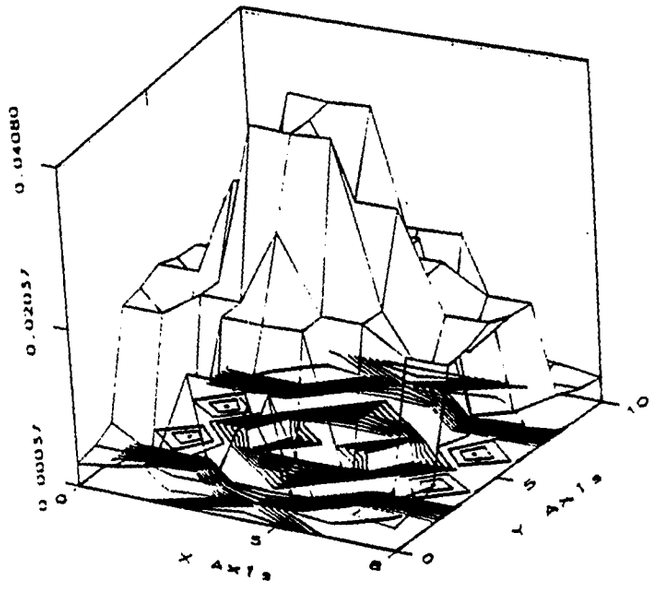

(a)

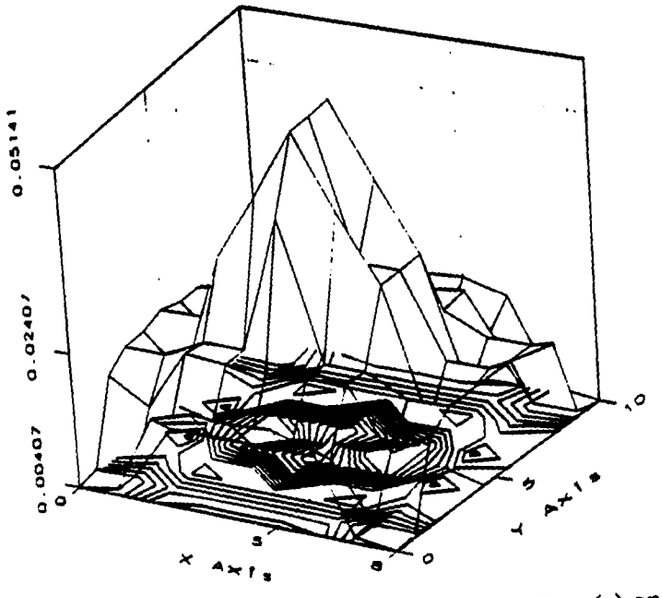

(b)

Figure 4.10: Profiles of fictitious source strength distribution, (a) on the top plate, (b) on the bottom plate.

were estimated to be (0.73m/s, 0), (0.21m/s, 0) and (0.73m/s, 0) respectively. The results for active control using these three secondary sources is shown in Figure 4.11. The maximum predicted sound pressure level is 14.7dB, and the predicated reduction in sound pressure level is about 34.1dB. Besides the significant reduction in radiated sound, it is interesting to notice that the radiation pattern is non-directive. The combination of these secondary sources and plate vibration has the radiation properties of a monopole.

The numerical results show that active noise control obtained in both cases is satisfactory and all of the three positions of boundary nodes were near optimal locations for secondary sources. Comparing with the results obtained by Giordano and co-workers shown in Figure 4.8, much better results were predicted using the method proposed in this research. Examination of the fictitious source strength profile on the top plate, plotted in Figure 4.10(a), reveals that the positions indicated by 1 to 4 in Figure 4.7, where Giordano and co-workers located their four secondary sources, were locations of minimum fictitious source strengths. This is a potential explanation for why Giordano and co-workers' system was not as efficient in canceling the sound radiation from the plates.

4.4 Active Noise Cancellation of the (0, 1, 0) Mode Within a Rectangular Cavity

Starting from this case, the same configuration of boundary and primary source were used to investigate the active noise control inside a rectangular cavity. The dimensions of the cavity are 4m×5m×3m in the x, y and z directions, respectively, as shown in Figure 4.12. All six sides of the cavity were assumed to be rigid. A primary point source was placed inside the cavity at coordinates (1, 1, 1). The first seventy resonant frequencies of the cavity [calculated from equation (4.1)] are listed in Appendix B. Four hundred field points were

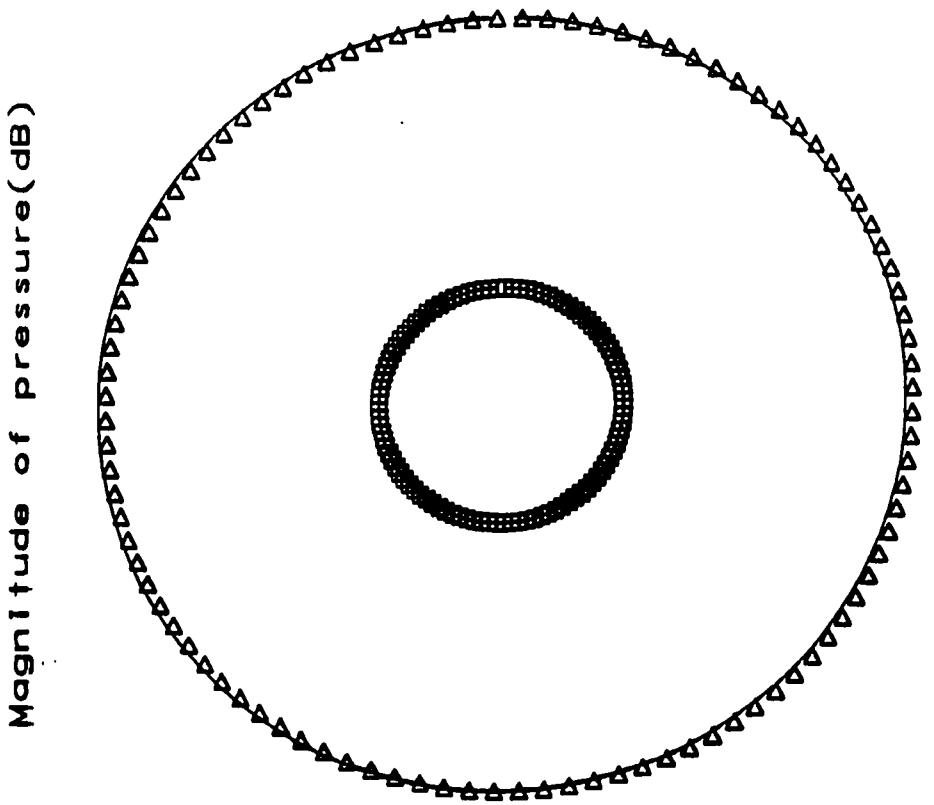

Figure 4.11: Pressure distribution of sound field, Δ: primary pressure level with maximum 48.8dB, □: result after adding three secondary sources with maximum 14.7dB.

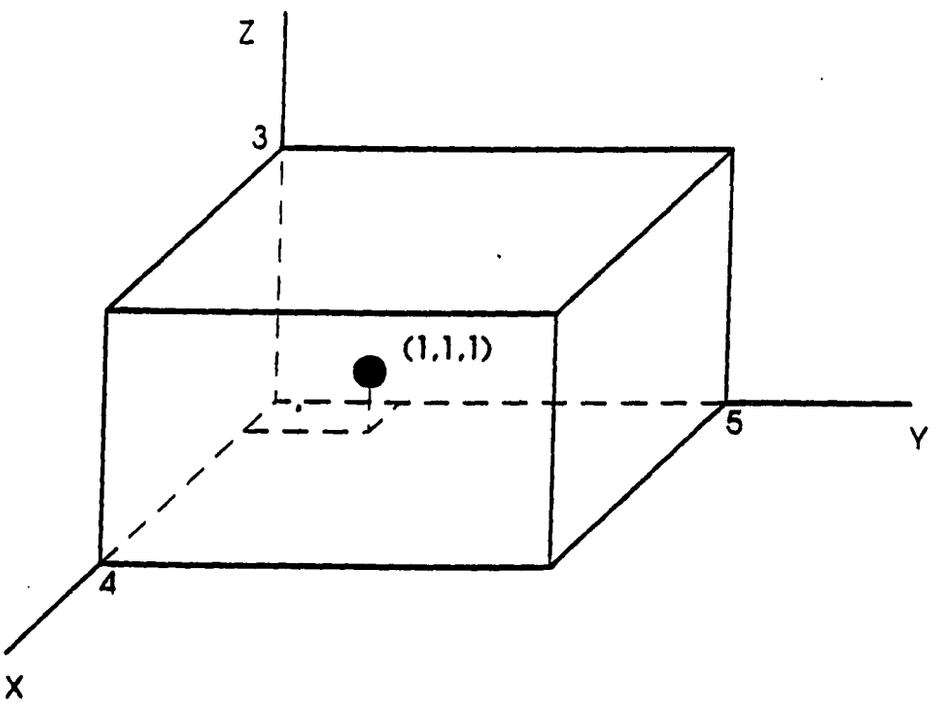

Figure 4.12: Configuration of the cavity and location of the primary point source.

chosen on the plane surface $z = 1.5m$ and $0.5m \leq x \leq 3.5m$, $0.5m \leq y \leq 4.5m$ to evaluate the sound pressure level.

For a driving frequency of 34.3Hz, the lowest resonant frequency of the cavity, the (0, 1, 0) mode shape was excited as illustrated in Figure 4.13(a). In order to cancel this dominant mode, a secondary source was located and optimized following the procedure described in Chapter 3. Since the (0, 1, 0) mode is the lowest resonant mode of the cavity, there were no other modes that would be excited by secondary sources. Any boundary nodal locations with high fictitious source strength are candidate optimal locations for secondary sources. Examination of the fictitious source strength distribution on each boundary wall reveals a maximum value at the corner on the wall $z = 0$, as illustrated in Figure 4.14(a). The nodal location (0.2, 0.5, 0) denoted by • in Figure 4.14(a) was selected as an optimal location for the secondary source. The strength of the secondary source was then optimized using 10 observation points evenly distributed along $y = 0.5m$ and $y = 4.5m$, which correspond to maximum pressure locations of the primary sound field as shown in Figure 4.13(a). The optimal secondary source strength was found to be (0.0549m/s, -1.579rad) for the magnitude and phase respectively. The predicted result of active cancellation is shown in Figure 4.14(b). In order to visualize the reduction in pressure level, the vertical scale in Figure 4.14(b) is identical to the scale in Figure 4.14(a). From Figure 4.14(b), it can be observed that the pressure level throughout most of the field plane was below 80dB except for a small region where the sound field was dominated by the direct contribution from the primary source located at (1, 1, 1). Comparing Figure 4.14(b) with Figure 4.13(a) reveals a surprisingly large attenuation for only one secondary source. To better understand the mechanism responsible for this surprising result, the pressure distribution, both magnitude and phase of the secondary source only is plotted in Figure 4.15. It is noticed that the pressure magnitude plots in both Figure 4.15(a) and Figure 4.13(a) are virtually identical. Comparison of the phase plots given

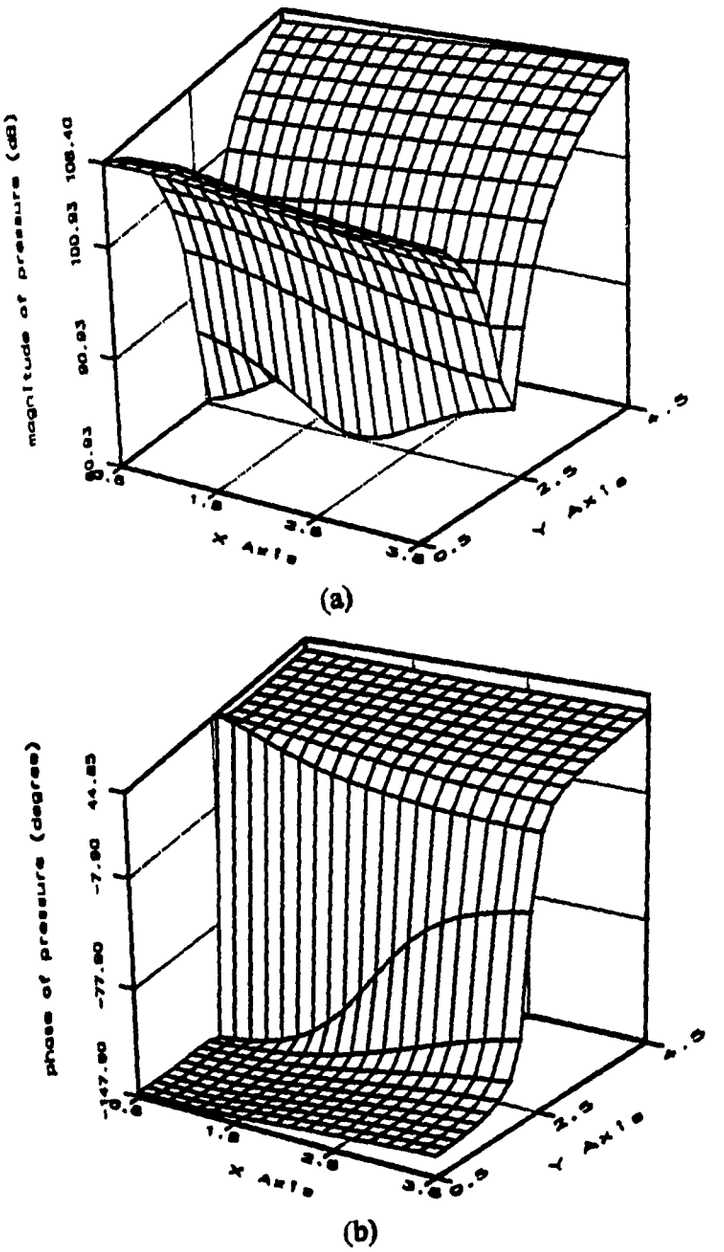

Figure 4.13: Primary pressure distribution in the cavity for f=34.3Hz, (a) magnitude, (b) phase.

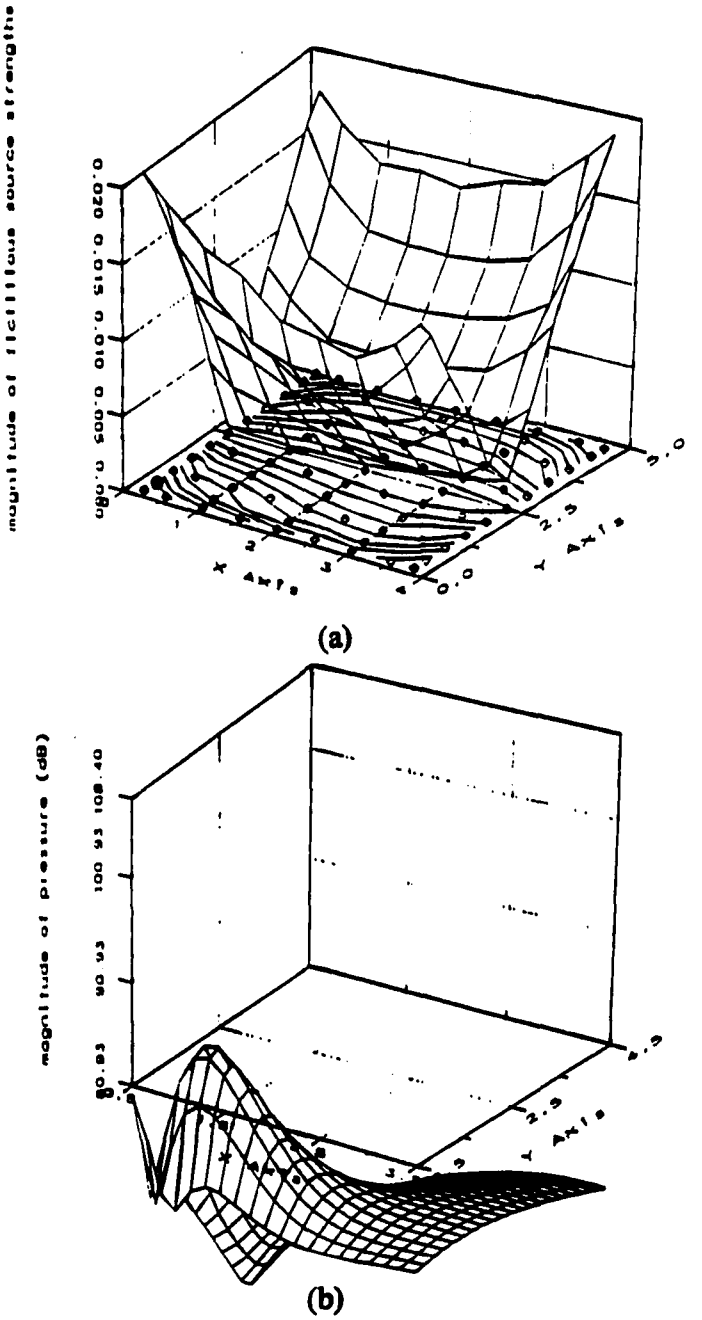

Figure 4.14: (a) Distribution of fictitious source strength on the boundary z = 0, (b) pressure distribution of the sound field with control using one secondary source located at •, f=34.3Hz.

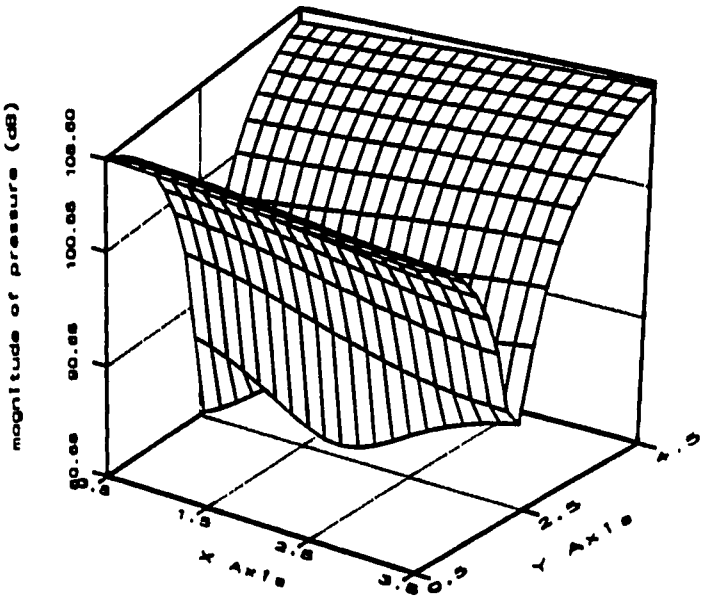

(a)

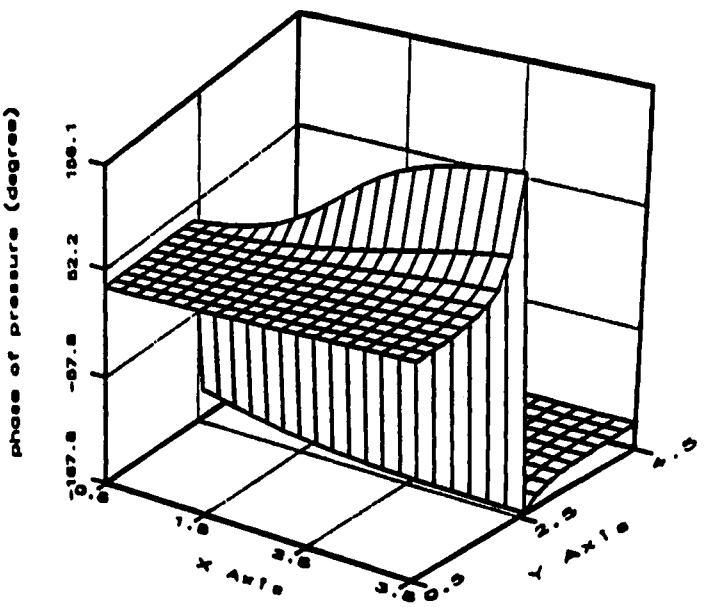

(b)

Figure 4.15: Pressure distribution of the sound field due to a secondary source located at •, f=34.3Hz, (a) magnitude, (b) phase.

in Figure 4.15(b) and 4.13(b) reveals that the secondary source field is almost exactly out of phase with the primary field. This is the explanation of why the combination of these fields results in such a large suppression of the primary sound pressure level at the field points.

To illustrate the potential of multiple optimal locations for secondary sources as mentioned in Chapter 3, the previous case was investigated for secondary sources located at other high fictitious source strength positions. Figure 4.16 illustrates active control prediction for secondary sources at different high fictitious source strength locations while the primary source and observation points remained unchanged. Figure 4.16(a) is a plot of the pressure field after active control with a secondary source at (0.5, 0.2, 3), and Figure 4.16(b) a similar plot for a secondary source at (0.5, 0, 0.2). The optimal strength for the two secondary sources are (0.0517m/s, -1.59rad) and (0.05m/s, -1.59rad), respectively. Comparing Figures 4.16 and 4.13(a), it is observed that almost the same attenuation of sound pressure level can be obtained using any of the three different secondary source locations.

The node denoted by • in Figure 4.14(a) is not a location of maximum fictitious source strength on that wall. The corner node near • is the actual location of maximum fictitious source strength. According to the discussion in Chapter 3, this corner node should be a better location for the secondary source but this is not true for this case. Figure 4.17 is a plot of predicted pressure after active control using the corner node as the location for a secondary source. In Figure 4.17, the primary mode shape is canceled by the secondary source, but global reduction is much less than is predicted for the previous cases. To understand this exception, the magnitude and phase due to the secondary source only are plotted in Figure 4.18(a) and (b). From Figure 4.18, it can be seen that the sound field is dominated by the first mode in the y direction, but there are also significant contributions from other wave forms which are the direct field from the secondary source and the reflection from the corner. It is more obvious in Figure 4.18(b) that the mode excited by the secondary source is not solely in

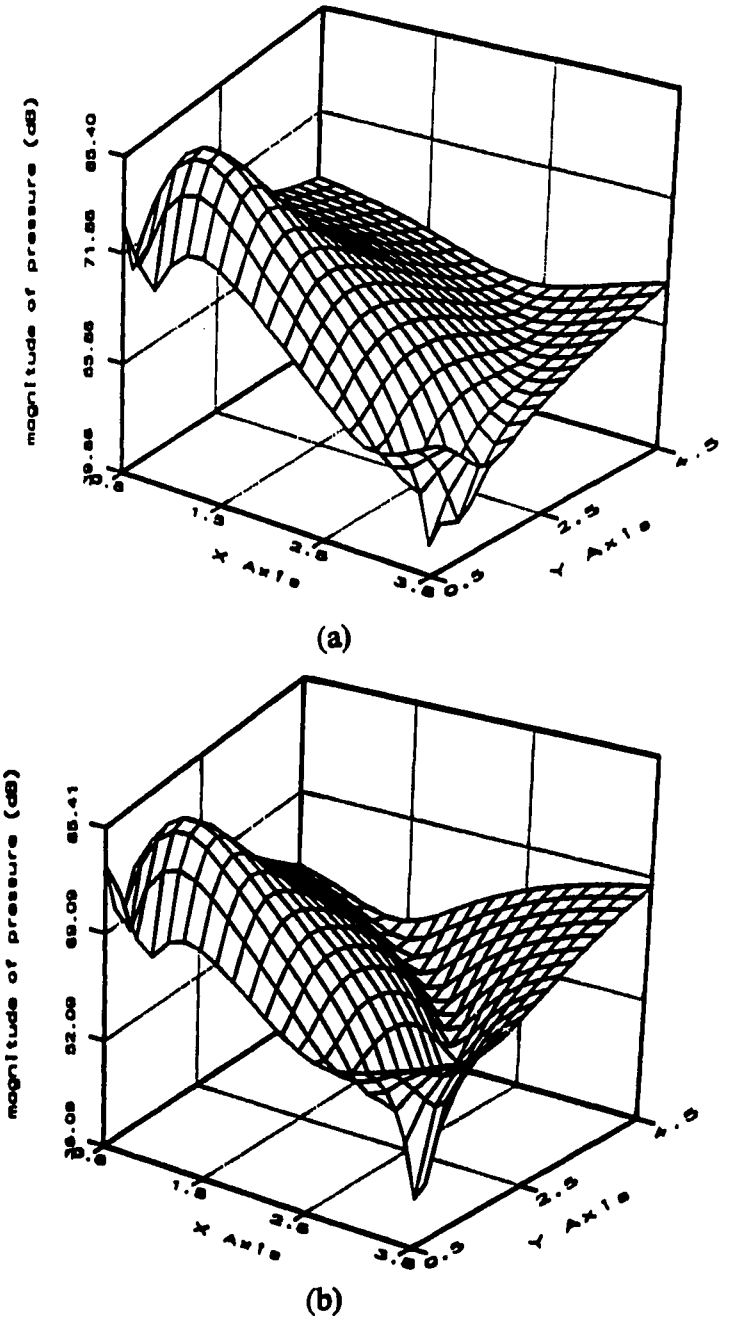

Figure 4.16: Demonstration of multiple optimal locations for secondary sources, (a) predicted active control with a secondary source located at (0.5, 0.2, 3), (b) predicted active control for a secondary source located at (0.5, 0, 0.2).

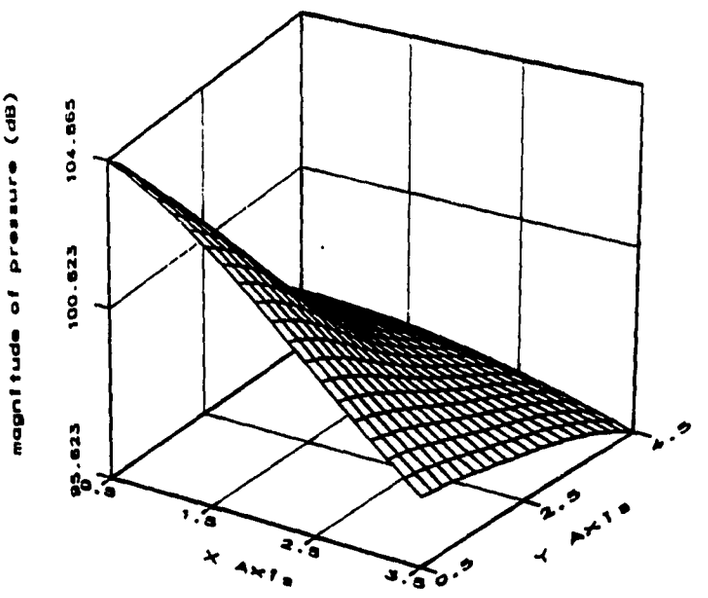

Figure 4.17: Pressure distribution after active control for a secondary source located at the corner.

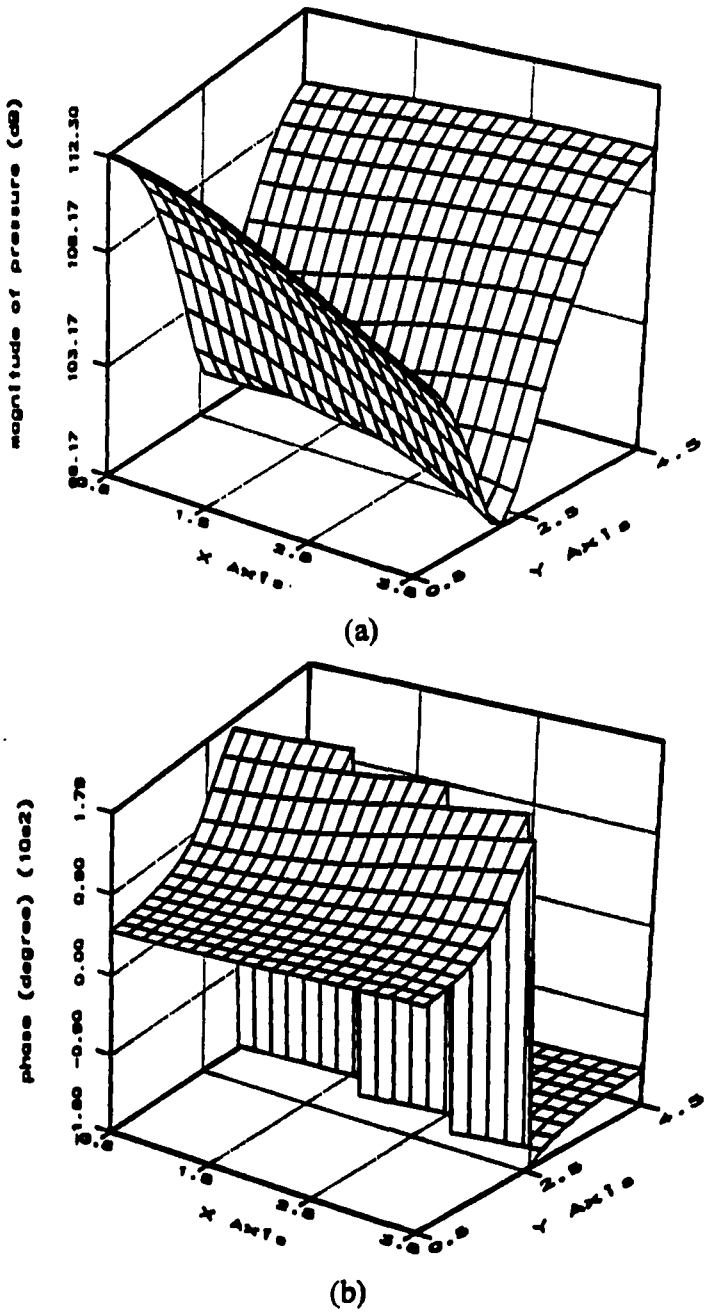

Figure 4.18: Pressure distribution for a secondary source located at a corner of the wall z = 0, (a) magnitude, (b) phase.

the y-direction as was the case for the primary source in Figure 4.13(b) because of the reflection at the corner. This secondary source radiation pattern is not able to match as well to the primary source radiation pattern. Thus, the combination of the two fields will result in less significant reduction than the cases with the secondary source located slightly away from the corner. Further numerical investigations have shown that corner nodes are usually not good locations for secondary sources, even if they are locations of high fictitious source strength.

4.5 Global Control of the (0, 3, 0) Mode

In this example, the same cavity and primary noise source were used as in Section 4.4. The driving frequency of the primary source was increased to 103.0587Hz corresponding to the (2, 0, 1) resonant mode. This case is an attempt to achieve global control in a frequency range of moderately high nodal density. The sound field excited by the noise source is shown in Figure 4.19(a). It is obvious that the mode shape displayed in Figure 4.19(a) is the (0, 3, 0) mode and not the (2, 0, 1) mode. This is because the primary source was located at (1, 1, 1), which is a nodal point of the second mode in the x-direction. Since all boundaries are assumed to be rigid, the nodal point was also a position of zero pressure. As a result, the second mode in the x-direction could not be excited by the primary source. From Appendix B, it can be seen that the resonant frequency for the (0, 3, 0) mode is just below the resonant frequency for the (2, 0, 1) mode, and the two frequencies are so close that this mode was fully excited by the noise source.

This case is a good example of a situation requiring the second criterion for optimal location of secondary sources, which is to avoid excitation of adjacent resonant modes. From the distributions of fictitious source strengths on each boundary surface, the locations of

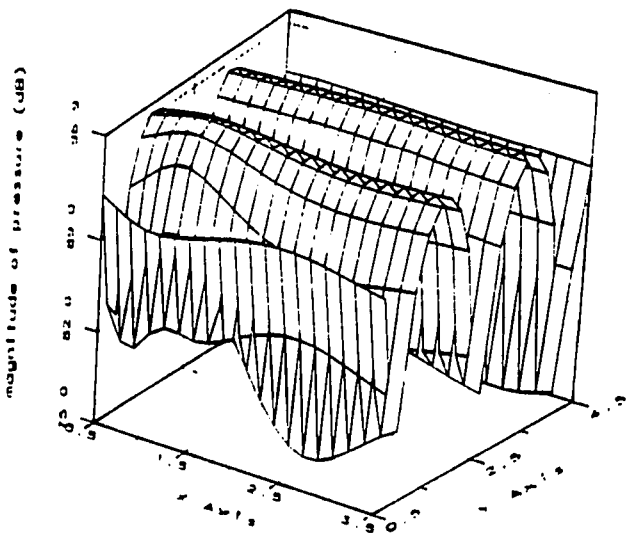

(a)

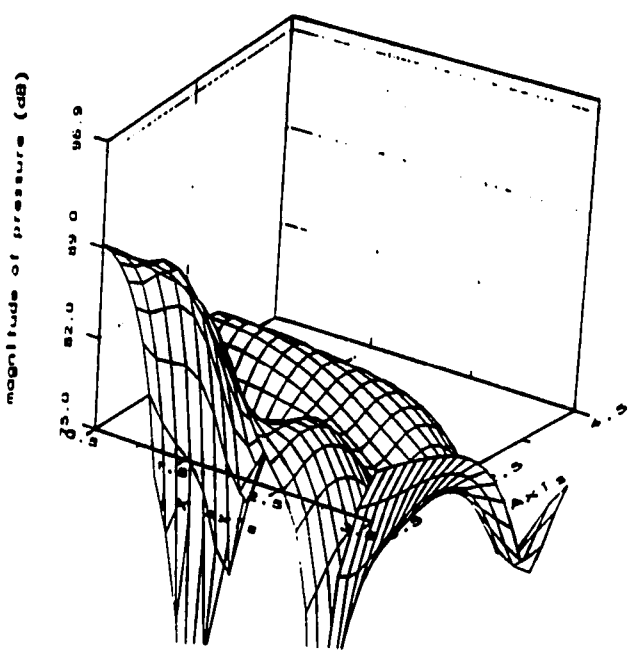

(b)

Figure 4.19: Pressure distribution of sound field, f = 103.06Hz, (a) primary sound field, (b) with active control using two secondary sources.

highest fictitious source strength were found to be at the corners of the boundary. Secondary sources were positioned at these highest fictitious strength locations, but the predicted active attenuation was very poor. Only about 5dB reduction in sound pressure level was obtained for these secondary source locations because the (2, 0, 1) mode shape was significantly excited by the secondary sources and also the corner nodes are not good locations for secondary sources.

To cancel the (0, 3, 0) mode while also avoiding excitation adjacent resonant modes, especially the (2, 0, 1) mode for this case, the secondary sources must be placed at the nodal points or near nodal points of the second mode in the x direction otherwise the (2, 0, 1) mode will be significantly excited by the secondary sources and become the dominant mode. This means that the secondary sources can't be located on the boundaries x = 0 and x = 4m. Examining the fictitious source strength distribution on the remaining boundaries, two locations, (1, 0, 0.2) and (1, 0, 1) denoted by • on the boundary y = 0, were selected for the secondary sources as shown in Figure 4.20. Ten observation points were uniformly distributed along y = 0.5m and y = 4.5m for optimization of secondary source strength. The optimized secondary source strengths were calculated to be (0.03743m/s, 1.616rad) and (0.031m/s, -1.535rad) respectively. With these two secondary sources, the predicted sound field is plotted in Figure 4.19(b). Except for the region dominated by the direct field of the primary noise source, the predicted reduction is more than 20dB for most field points.

This example demonstrated the critical importance of the second criterion for optimal locations of secondary sources when modal density is not low. When two frequencies corresponding to different resonant modes are close together or the modal density is high near the driving frequency, it is very possible to excite additional resonant modes with secondary sources. Thus the two criteria must be considered simultaneously if the global control of the acoustical field is desired. It seems likely that the predicted reduction for this example is less

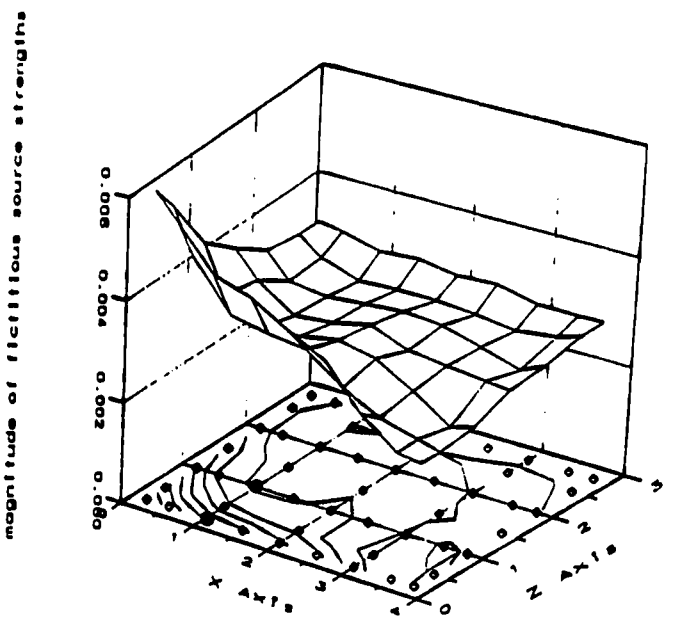

Figure 4.20: Distribution of fictitious source strength on the wall y = 0, •: the locations of secondary sources, ◊ the locations of boundary nodes.

than for the previous example because the secondary sources are not at locations of maximum fictitious source strength. Although some reduction was sacrificed to avoid excitation of nearby resonant modes, the compromise is necessary if global attenuation is to be maximized.

4.6 Active Local Control for High Modal Density Situations

So far all the cases investigated have involved active global control of sound pressure level. Global control is possible only for exterior radiation problems or for interior problems at low frequencies or low modal densities. When the cavity is excited at high frequencies, numerical predictions suggest that global control is not effective, or for some cases even possible, because of high modal density. Generally, it is not possible in such cases to attenuate one dominant resonant mode while avoiding excitation of other nearby resonant modes. For such cases, local control of sound pressure level in a region of particular interest is a more practical and feasible choice.

In this example, local control of the primary field in a selected region was investigated. Using the same geometry as for the previous examples, the cavity was excited at a resonant frequency of 180.7769Hz. The corresponding mode shapes were (4, 0, 1) and (0, 5, 1) since these modes share the same resonant frequency. The primary pressure field is plotted in Figure 4.21(a). Examination of the modal frequency distribution from Appendix B reveals that in addition to the (4, 0, 1) and (0, 5, 1) modes, the resonant frequencies of the (1, 1, 3) (180.075Hz) and the (0, 4, 2) (178.5944Hz) modes are very close to the driving frequency. There are also several additional resonant frequencies within 5Hz of the driving frequency. For this high modal density, it is extremely difficult to achieve significant global attenuation.

Instead of global control an attempt was made to control the central portion of the sound field shown in Figure 4.21(a). Twenty observation points, marked by $\times$ in Figure

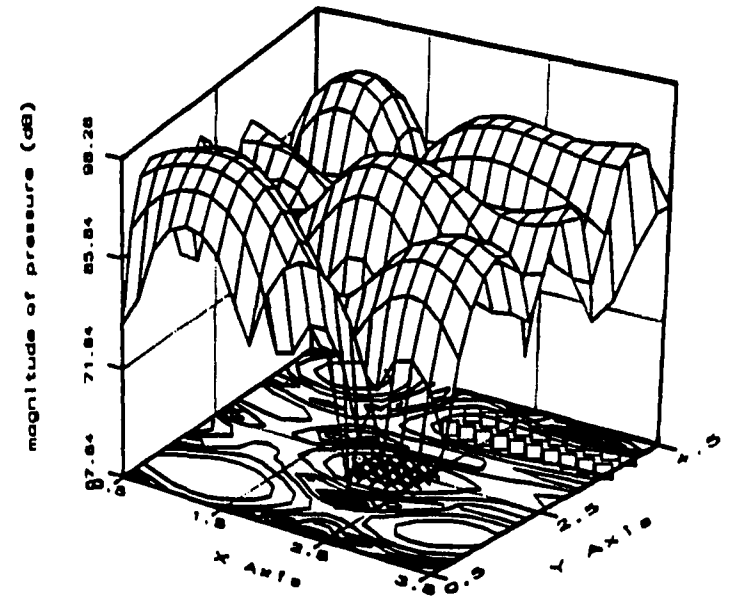

(a)

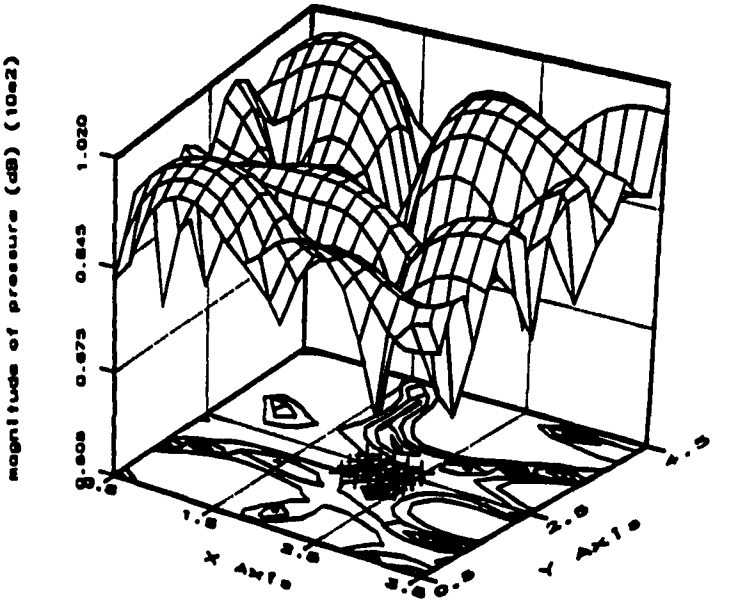

(b)

Figure 4.21: Pressure distribution of sound field, f=180.7769Hz, (a) primary sound field, (b) with active control using two secondary sources, contour maximum=90dB.

4.21(a) were uniformly distributed throughout in the region of interest. The objective of this example was to demonstrate local active control, and also to illustrate a method for estimating the optimal number of secondary sources as discussed in Chapter 3. To estimate the optimal locations of secondary sources for local control, the only criterion is the magnitude of fictitious source strength on the boundary. With the aid of the fictitious source strength distribution on the boundary for the primary source only, two secondary sources were located at (3.8, 4.5, 0) and (3.8, 4.8, 0). After optimizing the strengths of these two secondary sources with the respect to the twenty observation points, the predicted sound field with two secondary sources is plotted in Figure 4.21(b). In Figure 4.21(b), the contour maximum is 90dB and the reduction is generally less than 10dB. For further suppression of the residual sound field, two additional secondary sources were next added to the system. The optimal locations for the additional secondary sources were decided using the fictitious source strength distribution on the boundary in the same way as for the first two secondary sources. The optimal locations of the additional secondary sources were found to be (0.2, 0.5, 3) and (0.5, 4.8, 3). The strengths of the two additional secondary sources were optimized using the original observation points. The predicted sound field due to the primary source and the four secondary sources is plotted in Figure 4.22(a). It is observed that the pressure level at most field points was attenuated with the exception of one corner where a 2dB increase is observed. The contour maximum in Figure 4.22(a) is 85dB. The difference between Figure 4.21(b) and 4.22(a) suggest that more secondary sources might be needed to obtain further reduction in sound pressure level. An additional pair of secondary sources were then introduced into the system. Using the same method as before, optimal locations for the new secondary sources were found to be at (4, 1, 2.8) and (4, 1.5, 2.8). The optimal strengths for the six secondary sources were estimated to be (0.00543m/s, 1.60rad), (0.00325m/s, 1.28rad), (0.0027m/s, -0.874rad), (0.0059m/s, -1.46rad), (0.00178m/s,-1.83rad) and (0.00298m/s,

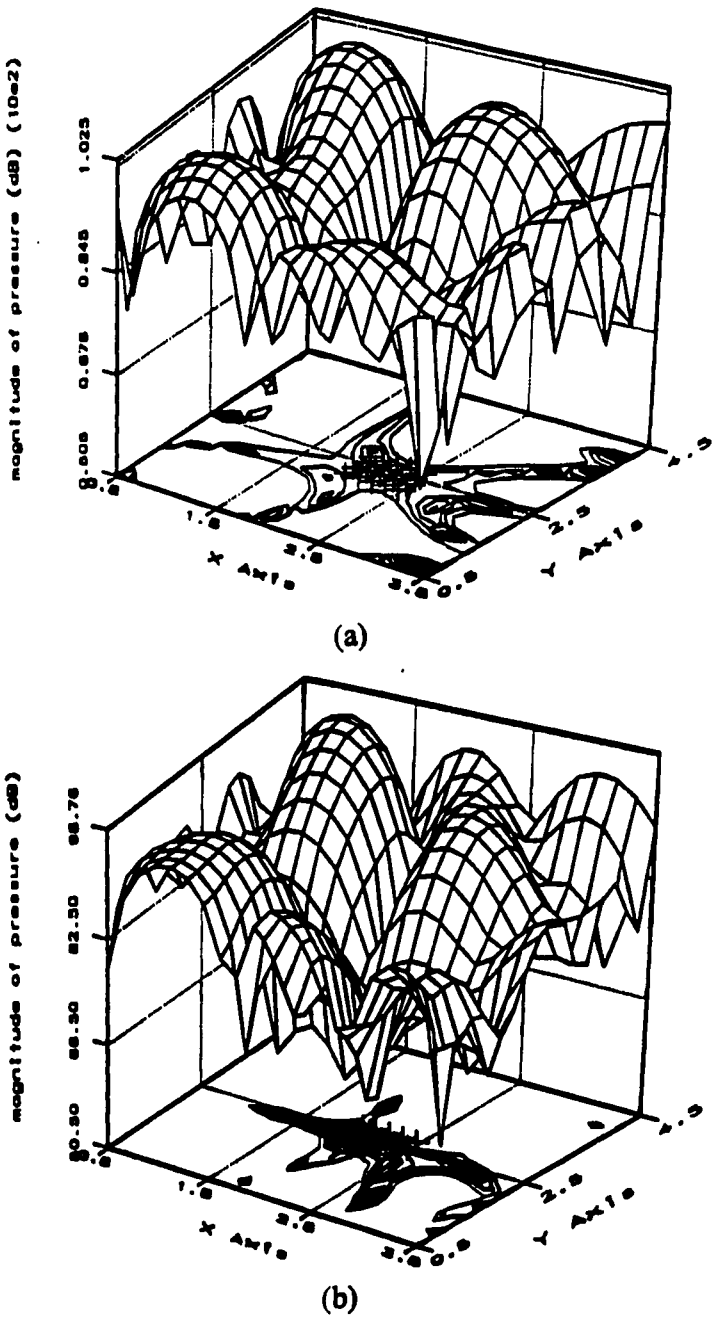

Figure 4.22: Pressure distribution of sound field, f=180.7769Hz, (a) with control using four secondary sources, contour maximum=85dB, (b) with control using six secondary sources, contour maximum=75dB.

1.345rad), respectively. The predicted pressure distribution with the six secondary sources is plotted in Figure 4.22(b). The contour maximum in Figure 4.22(b) is 75dB. Thus, at least 25dB reduction has been obtained in the region of interest with six secondary sources. To investigate saturation with respect to the number of secondary sources, two more secondary sources were inserted into the system, but no further reduction in predicted pressure level was observed. This implies that six might be a near optimal number of secondary sources for this case.

If the region of interest was not at the center of the field, the procedure described above can still be applied to achieve local active control of the sound field. The only difference would be the locations of the observation points. As shown in Figure 4.21(a), twenty observation points represented by □ were placed in another region of interest. After several trials, the optimal number of secondary sources was estimated to be five. The estimated optimal locations for these secondary sources were at (3.8, 4.5,0), (0.2, 0.5, 3), (0.5, 4.8, 3), (4, 1, 2.8) and (4, 1.5, 2.8). The optimal strengths were (0.001964m/s, 1.2376rad), (0.005273m/s, 1.7812rad), (0.006842m/s, -1.319rad), (0.008023m/s, 1.2649rad) and (0.003093m/s, 1.7823rad), respectively. The predicted results of active control with these five secondary sources are illustrated in Figure 4.23. The contour maximum in Figure 4.23 is 85 dB. The reduction in predicted pressure level is more than 15dB within the region of interest. Although the reduction is not as great as in the previous case, the region of interest is larger in this case.

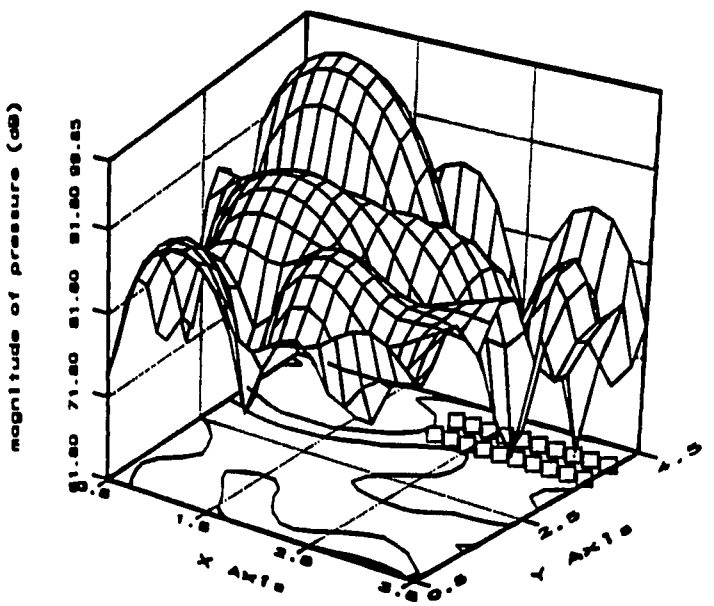

Figure 4.23: Pressure distribution of the sound field using five secondary sources with the observation points marked by □ in figure 4.21(a).

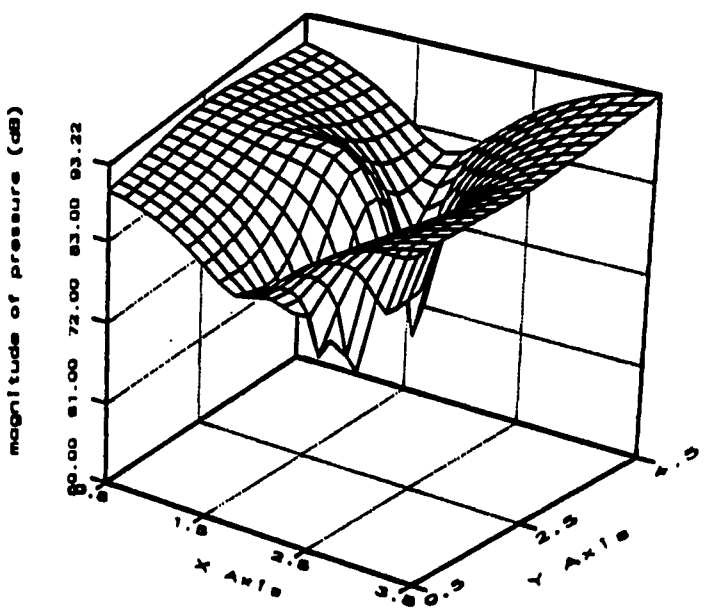

Figure 4.24: Primary pressure distribution, f=43.13Hz and $\alpha = 0.1$.

4.7 Active Control of a Sound Field with Finite Normal Acoustical Impedance Boundary Conditions

All cases investigated thus far have involved the rigid wall boundary condition. Although the rigid wall approximation can lead to satisfactory results for many cases, the finite normal acoustical impedance boundary condition is also important for many practical applications of the method proposed. Because of the effect of finite normal acoustical impedance and associated absorption coefficient, the properties of the sound field will be different from the rigid wall cases. In Chapter 2, it has been shown theoretically that the approach proposed in this research can be applied to cases involving finite normal acoustic impedance boundary conditions. To demonstrate this numerically, the same geometry and point source illustrated in Figure 4.12 were studied for finite normal acoustic impedance boundary instead of rigid wall.

The value of the normal acoustical impedance on the boundary was chosen so that the absorption coefficient on the boundary was a reasonable number. The absorption coefficient is related to the acoustic impedance by [28]

$$\alpha = \frac{4\mathrm{Re}\left(\dfrac{\rho c}{z_n \cos(\theta_i)}\right)}{\left|1+\dfrac{\rho c}{z_n \cos(\theta_i)}\right|^2} \tag{4.2}$$

where α is the absorption coefficient, ρ the density of the medium, c the speed of sound in the medium, z_n the normal acoustic impedance, θ_i the angle of wave incidence with respect to the surface normal and Re representing the real part. According to Equation (4.2) the absorption coefficient is a function of not only the normal impedance, but also the angle of wave

incidence. For the cases considered in this investigation, the resonant modes inside a rectangular cavity, normal incidence is a good assumption. With this assumption, Equation (4.2) can be simplified to

$$\alpha = \frac{4\mathrm{Re}\left(\frac{\rho c}{z_n}\right)}{\left|1+\frac{\rho c}{z_n}\right|^2} \tag{4.3}$$

Using Equation (2.29), the fictitious source strength distribution on the boundary can be estimated with specified z_n on the boundary. From this fictitious source distribution, the optimal locations of secondary sources can be found and optimal strengths can be calculated using selected observation points. The difficulty introduced by the normal acoustic impedance boundary condition is that the strength of the secondary source must be normal velocity in this approach, not normal acoustic impedance. After optimizing secondary source strength, the original normal impedance boundary condition becomes a mixed boundary condition, part of normal acoustical impedance and the other part of normal velocity. The general method to resolve this difficulty is to incorporate the mixed boundary condition into the computer program. In this way, the program becomes more versatile and powerful, but it also becomes more complicated and CPU time increases for even simple jobs.

Since this is only a preliminary investigation of a method for estimating optimal locations of secondary sources using fictitious source strength distributions on the boundary, it is not appropriate to implement a sophisticated general program if a reasonable alternative exits. A simpler method was chosen to overcome the difficulty. The fictitious source strength, σ, calculated from Equation (2.29) is substituted into Equation (2.27) to obtain an equivalent normal velocity boundary condition. In this way, the original normal acoustical

impedance boundary condition is converted into an equivalent normal velocity boundary condition and the previous procedure of optimization can then be utilized.

4.8 Global Control of a Sound Field with Normal Acoustical Impedance Boundary Conditions

The first example studied for normal impedance boundary conditions involved global control in a low modal density case. A point source was located at (1.8m, 2.5m, 0) within the cavity. A primary source with driving frequency of 43.13Hz was considered corresponding to the resonant frequency of the (1, 0, 0) cavity mode. A common boundary condition for all six walls was specified as a normal acoustical impedance z_n=800-j3500 (Pa*s/m). The corresponding absorption coefficient is $\alpha = 0.1$. The predicted field plane was taken to be the same as for the rigid wall case. The primary noise field for this case is shown in Figure 4.24. As expected, the dominant cavity mode is (1, 0, 0). It is obvious that attenuation of the (1, 0, 0) mode should be the initial priority for active noise control. By examining the fictitious source distribution on the boundaries, a node at (0, 2.5m, 0.2m) was chosen as a candidate optimal location for the secondary source because of its high fictitious source strength. The (1, 0, 0) mode is the second lowest resonant mode of the cavity. With the given driving frequency, the only additional mode that might be excited by the secondary source is the (0, 1, 0) mode with resonant frequency of 34.3Hz. The primary source was located at y = 2.5m which is a node point of the first mode in the y direction. The secondary source was also located at y = 2.5m so that the secondary source would not excite the (0, 1, 0) mode efficiently. Ten observation points were uniformly distributed along the pressure maximum in Figure 4.24, which was along x = 0.5m and x = 3.5m. For these observation points, the optimal strength of the secondary source was found to be (0.00475m/s, -1.654rad),

for magnitude and phase, respectively. Predictions for active cancellation with this secondary source are illustrated in Figure 4.25(a). From Figure 4.25(a), it is observed that the x-direction mode was partially canceled by the secondary source, but the reduction is only around 10dB. The residual sound field is dominated by two parts. The high amplitude region near the center of the observation plane results from the direct field of the primary source, and the remaining contribution is from the first resonant mode in the y-direction. Although both primary and the secondary sources were located at node points of the (0, 1, 0) mode, it was still excited significantly because of the effect of the finite impedance boundary condition. For rigid boundaries, the source would be at zero pressure points of the corresponding resonant modes, and thus would be unable to excite the modes. Because of the finite normal acoustical impedance, a node point is no longer a zero pressure point and the resonant modes can still be excited by a source positioned at that node. Usually it is difficult to totally cancel the direct field from the primary source. A better choice if additional attenuation is sought is to reduce the (0, 1, 0) mode. For this particular case, the location of a second secondary source is very critical. If the additional secondary source is located improperly, it might cancel the (0, 1, 0) mode while also re-exciting the (1, 0, 0) mode which was canceled by the first secondary source. If this happens, the total sound field could be increased instead of being attenuated. With this in mind, the optimal location of the second secondary source was selected as (2m, 2.5m, 0) which is a node point of (1, 0, 0) mode. Although the (1, 0, 0) mode might still be modestly excited by a secondary source at this location, this position is probably the best one for the second secondary source in this situation. Ten observation points were distributed near maximum pressure locations in Figure 4.25(a) (along y = 0.5m and y = 4.5m). The optimal strength of this secondary source was calculated to be (0.01896m/s, -1.8906rad). The final prediction for cancellation with two secondary sources are shown in Figure 4.25(b). It is

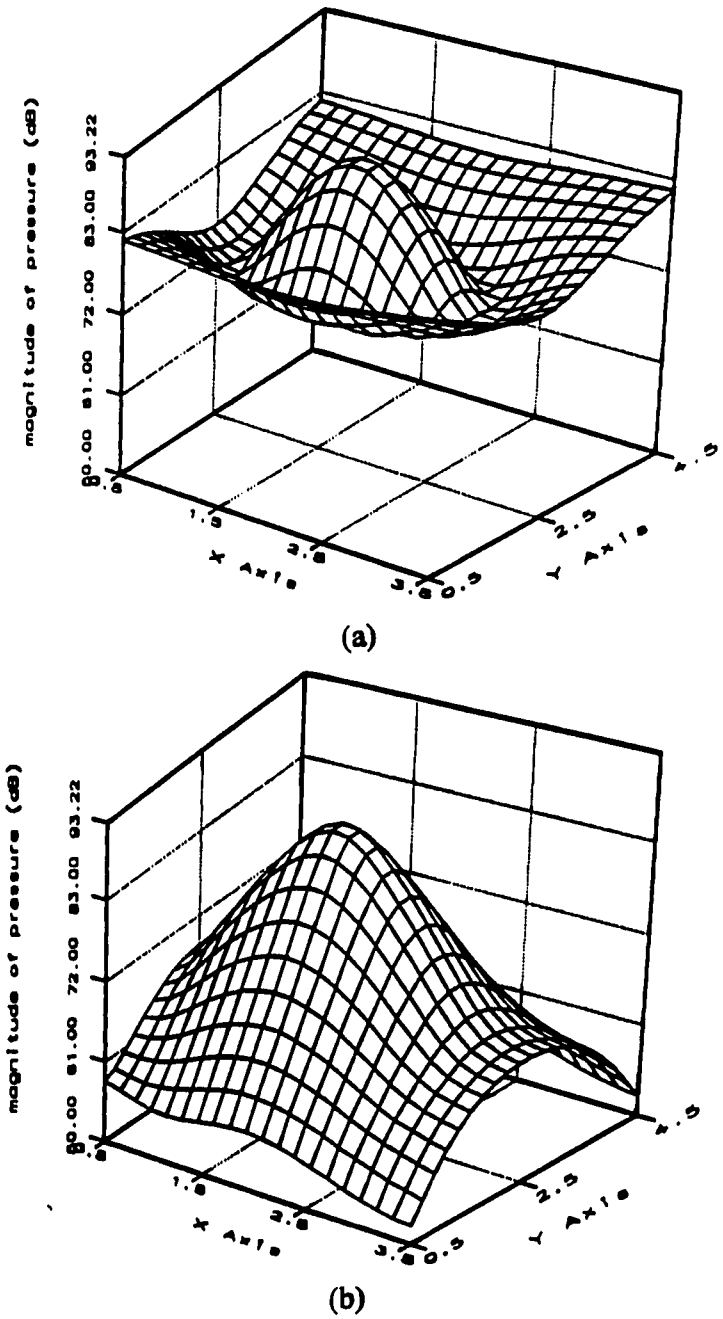

Figure 4.25: Predictions for active control, f = 43.13Hz and $\alpha = 0.1$, (a) one secondary source, (b) two secondary sources.

observed from Figure 4.25(b) that for most of the sound field the pressure level is less than 65dB, except for a small region where the sound pressure is dominated by the direct field from the primary source. The resulting predicted attenuation is significant and satisfactory.

4.9 The Effect of Absorption Coefficient on Global Active Control

The influence of varying the impedance boundary condition, i. e., the absorption coefficient, on the results of global active cancellation of sound field were also investigated. Three different values of normal acoustical impedance were used as boundary conditions. The magnitudes and phases of the normal acoustical impedance on the boundary were (8893Pa*s/m, -1.47rad), (3590Pa*s/m, -1.346rad) and (1612Pa*s/m, -1.052rad). The corresponding absorption coefficients are 0.02, 0.1 and 0.4 pretty much covering the range of practical interest. The primary source was placed at (1m, 1m, 1m) in the same rectangular cavity geometry used previously. The field plane was the same as in the previous case. The exciting frequency was 103.1Hz which was the resonant frequency of the (2, 0, 1) mode. Figure 4.26(a) is a plot of the predicted primary sound field for $\alpha = 0.02$. Because the primary source was at x = 1m, which is a node point of the second mode in the x direction, the (2, 0, 1) mode was not significantly excited and the sound field was dominated by the (0, 3, 0) mode which has a resonant frequency of 102.9Hz. To cancel this dominant mode, two secondary sources were used and the optimal locations of the two sources were found to be (1m, 0, 0.2m) and (1m, 0, 1m). It is noted that both secondary sources were located at x = 1m which is a node point of the second resonant mode in the x-direction. The intention was to diminish the possible excitation of that mode. Twenty observation points were distributed throughout the maximum pressure region in Figure 4.26(a). The optimal strengths of the secondary sources were estimated to be (0.03468m/s, 1.609rad) and (0.0299m/s, -1.578rad)

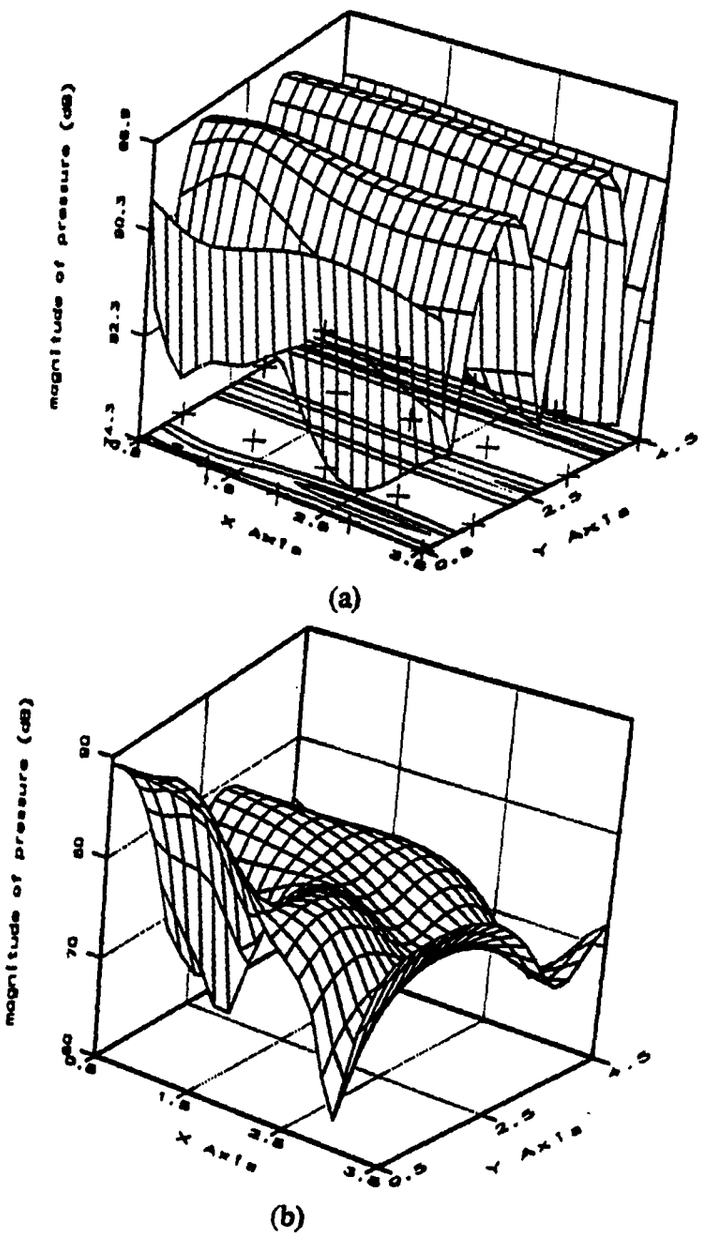

Figure 4.26: Sound pressure distribution, f=103.1Hz and $\alpha = 0.02$, (a) primary sound field, (b) with active control using two secondary sources.

respectively. The predicted results of active control are illustrated in Figure 4.26(b). It can be observed from Figure 4.26(b) that the third resonant mode in the y-direction was canceled, while the second resonant mode in the x-direction was not greatly excited by the secondary sources. The predicted reduction is more than 20dB in most of the field except for a small region where the direct field from the primary source is dominant.

The same experiment was repeated with different normal acoustical impedance, i.e., different absorption coefficient. Figures 4.27(a) and (b) are plots of the predicted primary sound field and active control results for $\alpha = 0.1$. The locations of the secondary sources were unchanged. The optimal strengths were (0.03062m/s, 1.625rad) and (0.02797m/s, -1.635rad). From Figure 4.27(b), it can be seen that the reduction is less than the $\alpha = 0.02$ case, but the reduction is still around 20dB for most of the field.

The predicted primary field and active control results for $\alpha = 0.4$ are shown in Figure 4.28. Comparison of Figures 4.28(a) and 4.26(a) reveals that more resonant modes were excited for the higher absorption coefficient case. It is also observed from Figure 4.28(b) that the average reduction is further decreased. There are no obvious dominant modes in the predicted results and the final predicted sound field is the result of contributions from many resonant modes. The reduction is obviously less than 20dB. From this investigation, it can be concluded that the impedance boundary condition has significant effect on the results of global active control. Increasing the absorption coefficient of the boundary increases the likelihood that more modes will be significantly excited. The resulting sound field includes contributions from many resonant modes and none of them is dominant. It is difficult to achieve significant reduction using the approach proposed in this work for cases with high modal density, and high absorption coefficient boundaries seems to increase the modal density of the field.

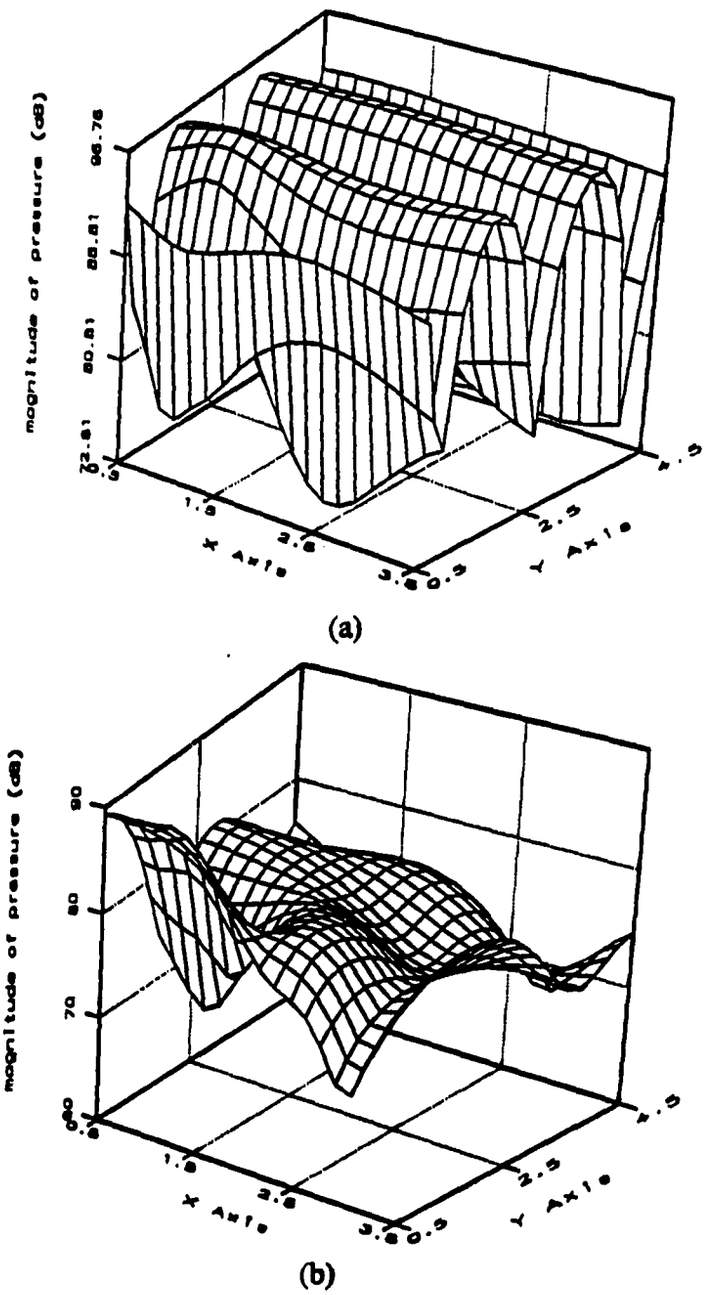

Figure 4.27: Sound pressure distribution, f=103.1Hz and $\alpha = 0.1$, (a) primary sound field, (b) with control using two secondary sources.

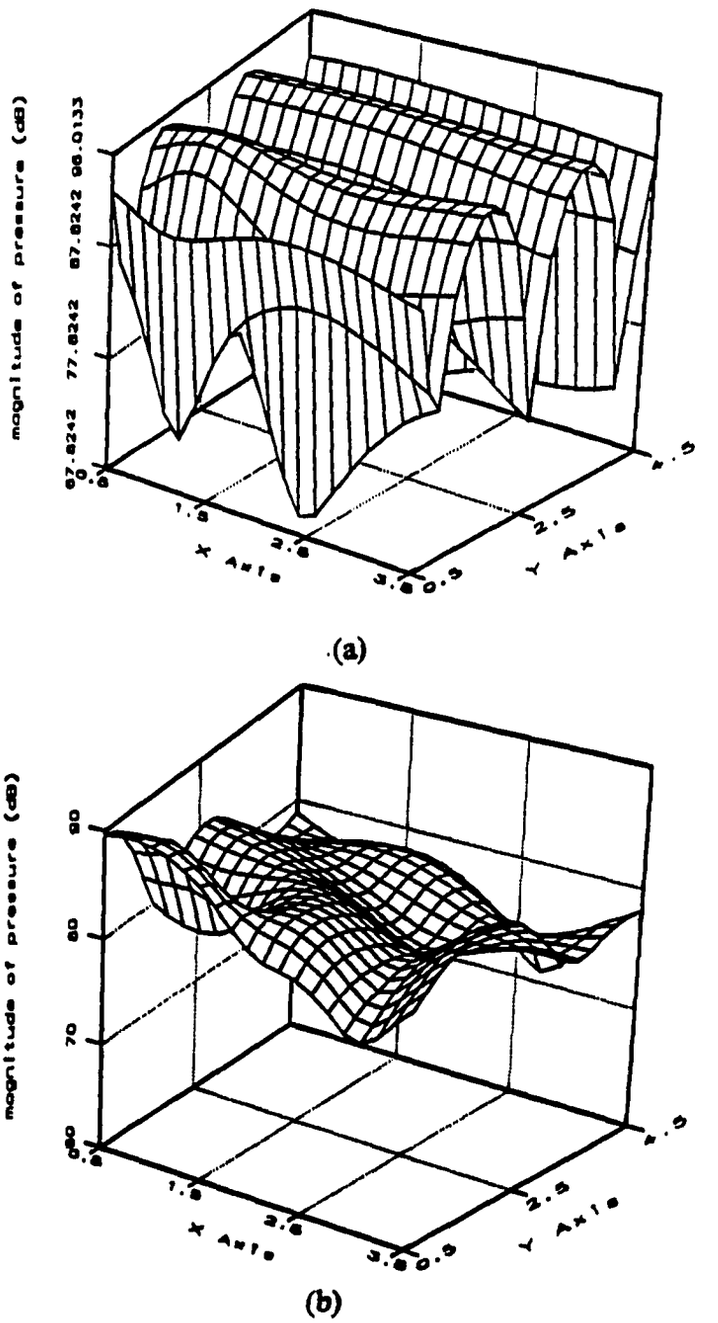

Figure 4.28: Sound pressure distribution, f = 103.1Hz and $\alpha = 0.4$, (a) primary sound field, (b) with control using two secondary sources.

4.10 Combined Global and Local Control for Normal Acoustic Impedance Boundary Conditions

For some cases, significant global control is not possible because of high modal density. In such situations, local control in a region of particular interest is a practical alternative approach. The following example is a typical case where a combination of the two control techniques is useful.

The location of the primary source was at (2m, 1m, 1m) in the rectangular cavity. The boundary condition was specified as z_n = (3590Pa*s/m, -1.345rad) on all surfaces and the corresponding absorption coefficient is 0.1. The exciting frequency was 103.1Hz. The predicted primary sound field for this case is shown in Figure 4.29(a). Although the pressure distribution is still dominated by the (0, 3, 0) mode, it can be seen from Figure 4.29(a) that the second mode in the x-direction has been excited significantly because the primary source was moved away from the node point of that mode. To cancel the third mode in the y-direction, which is the dominant mode in this case, two secondary sources were located at (2m, 0.2m, 3m) and (2m, 0, 2.8m) using the fictitious source strength distribution on the boundaries. With observation points denoted by x's in Figure 4.29(a), optimal strengths for these secondary sources were obtained to be (0.009479m/s, 1.2033rad) and (0.01472m/s, -1.765rad). Active control predictions using these secondary sources are plotted in Figure 4.29(b). The third mode in the y-direction is canceled, but the gross reduction is only around 10dB since the sound field was dominated by other resonant modes. Because the sound field in Figure 4.29(b) is dominated by several modes, global control for this case would not be very efficient or effective. It would be difficult to cancel one mode without further excitation of other modes. If further reduction is desired, local control in a region of particular importance is usually a practical choice. The next attempt in this case was to suppress the

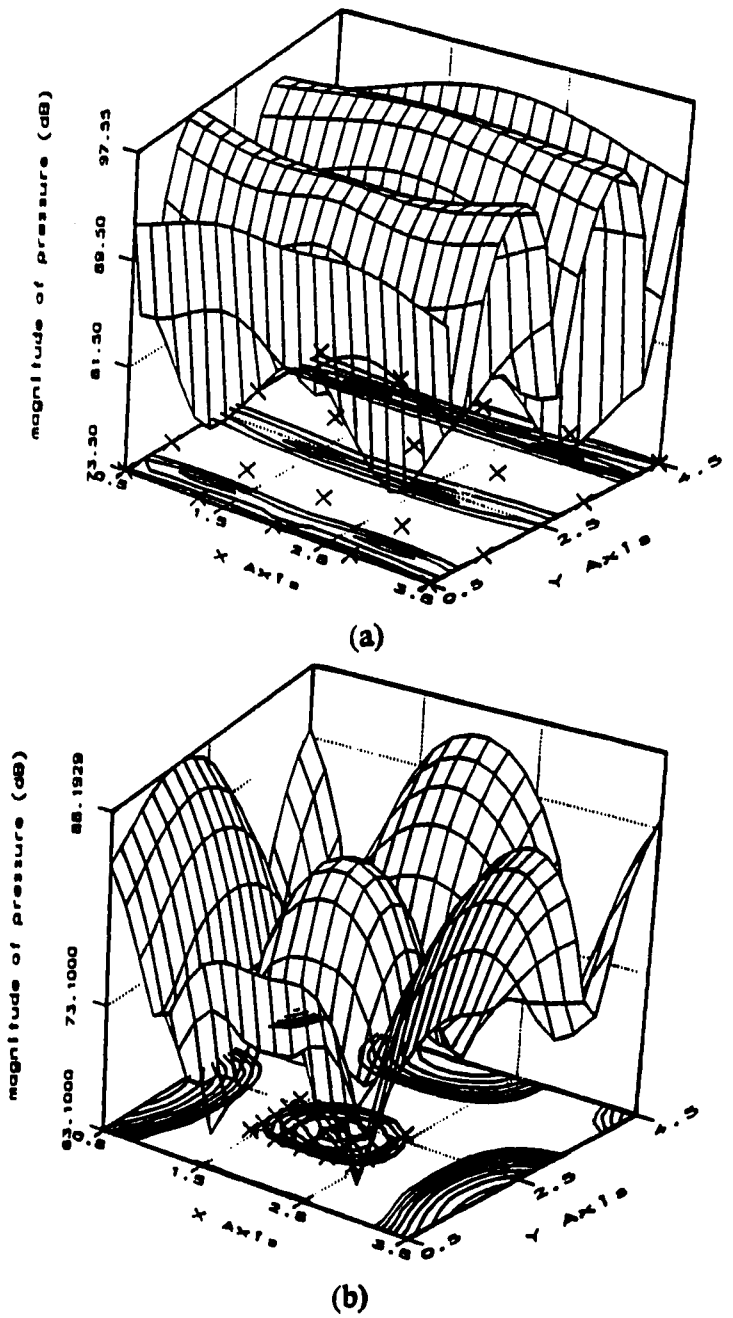

Figure 4.29: Sound pressure distribution, f=103.1Hz and $\alpha = 0.1$, (a) primary sound field, (b) predicted global control using two secondary sources.

local maximum region near the center of Figure 4.29(b). Twenty observation points, denoted by x's in the figure, were used throughout the region of interest as shown in Figure 4.29(b). Optimal locations for the second two secondary sources were found to be (0, 2.5m, 2.8m) and (4m, 2.5m, 2.8m). Both secondary sources were positioned at y = 2.5m to diminish the effect of these secondary sources on the third mode in the y-direction which has been canceled by the first two secondary sources. The optimal strengths for the additional secondary sources were estimated to be (0.003593m/s, -1.7125rad) and (0.003593m/s, -1.7125rad). Predicted results are shown in Figure 4.30. It is noteworthy that pressures in the region near the center of the field were greatly suppressed. The contour maximum in Figure 4.30 is 76dB compared with a contour minimum of 78dB in Figure 4.29(b). More than 20dB reduction has been achieved in the region of interest without negative effects on active control in other positions of the field. Thus, for this case, both modest global and significant local control of the primary sound field were obtained though proper selection of secondary source locations.

4.11 Local Control with Finite Acoustic Impedance Boundary Conditions and High Modal Density

Local active control of a sound field in a cavity with finite normal acoustic impedance boundary conditions and high modal density is investigated in this example. The boundary condition was specified as (8893Pa*s/m, -1.47rad) for all boundaries corresponding to an absorption coefficient of 0.02. The cavity was excited by moderately high resonant frequency of 180.78Hz. This is the same case as the one studied in Section 4.6 except the boundary condition is different. The predicted pressure distribution due to the primary source, shown in Figure 4.31(a), was expected to be similar to that obtained in Section 4.6. As discussed in previous sections, it is difficult to achieve significant global reduction for frequency ranges in

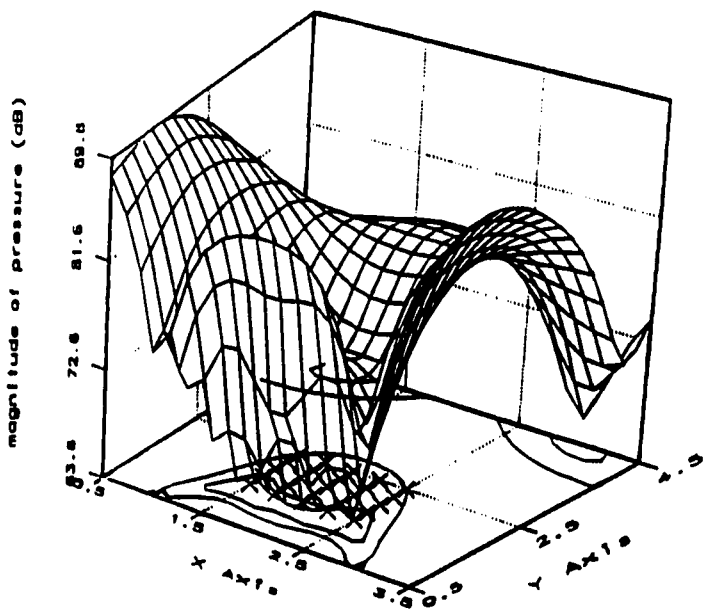

Figure 4.30: Predicted sound pressure distribution with global control and local control, f=103.1Hz and $\alpha = 0.1$.

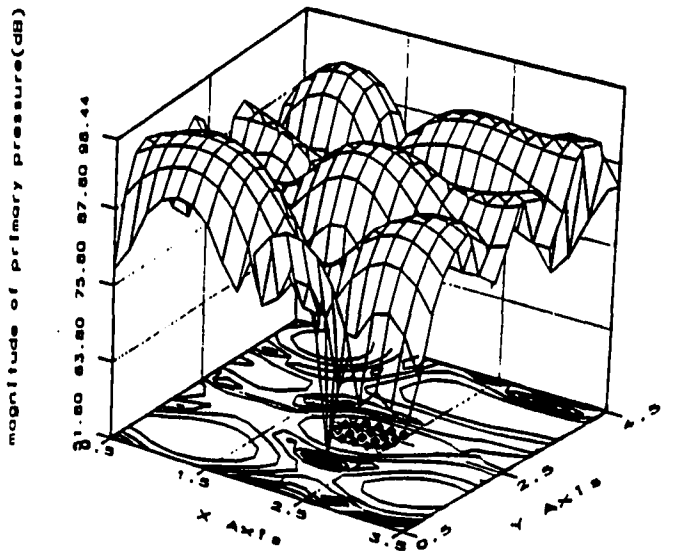

(a)

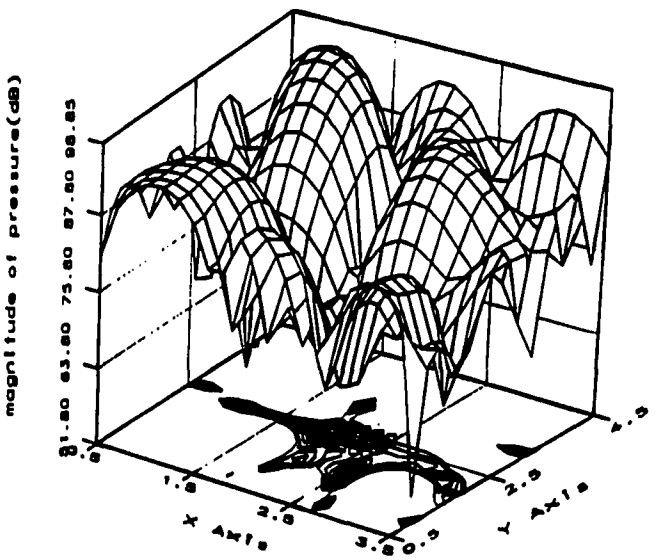

(b)

Figure 4.31: Sound pressure distribution, f = 180.78Hz and $\alpha = 0.02$, (a) primary sound field, (b) with control using five secondary sources, contour maximum=75dB.

which modal density is high. The goal of this example is to reduce the pressure in the central region of the cavity. Using the same procedure as in Section 4.6, the optimal number of secondary sources was estimated to be five. The optimal locations for these secondary sources were found to be (4, 1.5, 2.8), (3.8, 4.5, 0), (3.8, 4.8, 0), (0.5, 4.8, 3) and (0.2, 0.5, 3), respectively. Twenty observation points denoted by ◊s in Figure 4.31(a) were distributed throughout the region of interest. Optimal strengths of these secondary sources were calculated with the respect to these observation points. Predicted results after active control are plotted in Figure 4.31(b). In Figure 4.31(b), the contour maximum is 75dB indicating a reduction of more than 20dB in the region of interest, which is better than the result obtained for the rigid wall case. It is also observed that no significant increase in pressure level occurred outside the region of interest. The final result for this case is very similar to the rigid wall case because of the small absorption coefficient on the boundary.

4.12 Active Control with Variable Normal Impedance the Boundaries

In the previous cases all cavity boundaries have been specified as having the same acoustic impedance. This example will consider the same cavity geometry without the constraint of similar boundary conditions on all boundary surfaces. The acoustic impedance of the bottom wall of the cavity was specified as (8893Pa*s/m, -1.47rad) and the remaining cavity walls were approximated as rigid by specifying an acoustic impedance of (10E09Pa*s/m, 0). The location of the primary point source was at (1m, 1m, 1m), and the driving frequency was f = 42.88Hz corresponding to the resonant frequency of the (1, 0, 0) mode. The predicted primary sound field is shown in Figure 4.32(a). The sound field is dominated by the (1, 0, 0) mode as expected. In order to attenuate this sound field, a secondary source was positioned at (0.5, 0.2, 0) which was selected because of its high

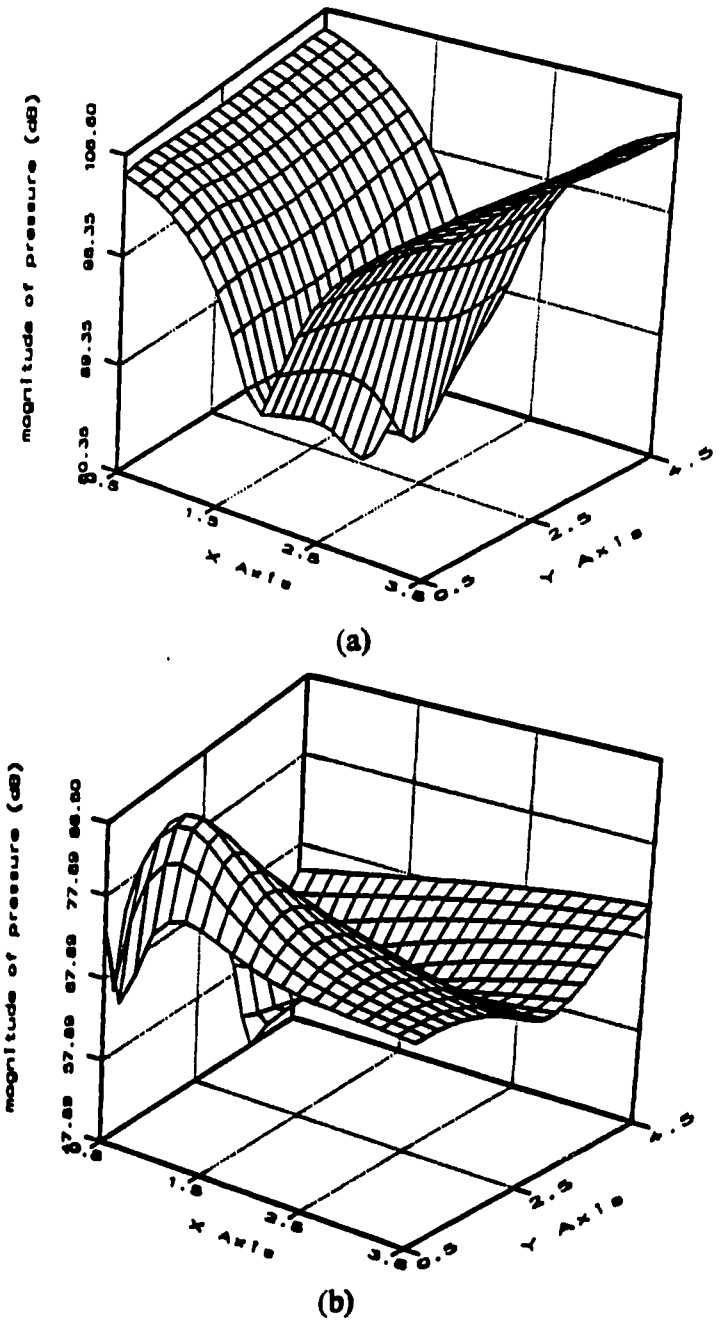

Figure 4.32: Sound pressure distribution, f = 42.88Hz, (a) primary sound field, (b) with active control using one secondary source.

fictitious strength value. Ten observation points located along the pressure maximum, x = 0.5 and x = 3.5, shown in Figure 4.32(a), were used as reference points for optimization of secondary source strength, with a resulting optimal strength of (0.03944m/s, -1.6rad). The predicted field after active cancellation using this secondary source is illustrated in Figure 4.32(b). The average reduction in Figure 4.32(b) is about 40 dB except in the region dominated by the direct contribution from the primary source. Because the secondary source and primary source were not located at node points of the first mode in the y-direction, the first mode in the y-direction moderately excited and becomes the dominant mode after the first mode in the x-direction is canceled. For further suppression of this mode, another secondary source was added. The location of the additional secondary source was (2, 0.2, 0). It was positioned at a node point of the first mode in the x-direction to avoid excitation of that mode by this secondary source. Another ten observation points were distributed along y = 0.5 and y = 4.5 which were locations of the pressure maximum of the (0, 1, 0) mode. The optimal strength for this secondary source was found to be (0.006386m/s, -1.2577rad). The predicted result of active control with two secondary sources is shown in Figure 4.33. The vertical scale in Figure 4.33 was kept the same as in Figure 4.32(b) for easy comparison. From Figure 4.33, it can be observed that the first mode in the y-direction was attenuated and significant further reduction was obtained. The overall predicted suppression is more than 40dB except in the region dominated by the direct field of the primary source.

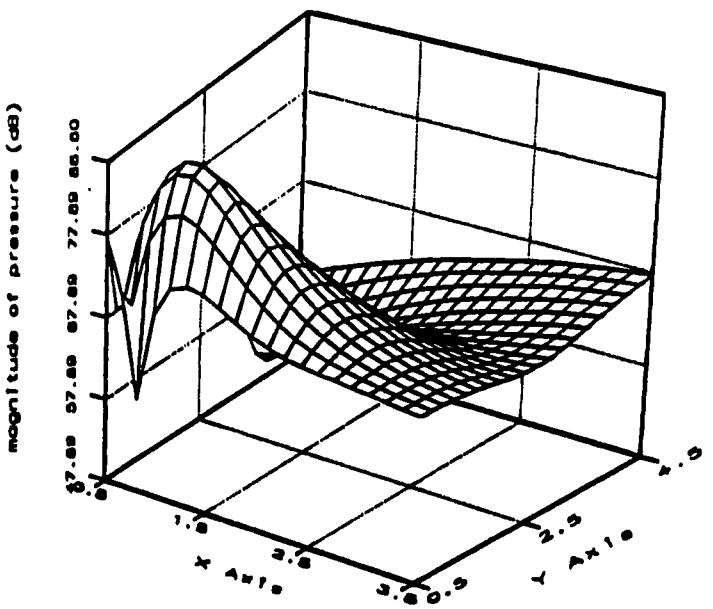

Figure 4.33: Predicted sound pressure distribution with active control using two secondary sources, f = 42.88Hz.

CHAPTER 5. CONCLUSION

The objective of this research was to develop a systematic approach for estimating secondary source locations as part of a general method for active noise cancellation in three-dimensional space, bounded or unbounded. Using the Helmholtz equation and Huygen's principle, the boundary integral equations for acoustical problems were derived and a numerical implementation was developed, computer codes implementing the indirect boundary element method and optimization of strengths of secondary sources were programmed and verified. Examples of active noise cancellation in three-dimensional space were investigated. The major work can be cataloged into three parts.

First, a theoretical derivation from the wave equation and Huygen's principle to the boundary integral equation for different boundary conditions, pressure, normal velocity and normal acoustical impedance was constructed. A numerical implementation of the resulting boundary integral equations was developed and verified for several of examples. Numerical predictions were compared with available analytical, numerical and experimental results from prior work. Good agreement between the numerical results and analytical results were observed. This good agreement suggested that the numerical implementation is reliable and accurate. The indirect boundary element approach was employed to predict the primary sound field and evaluate the results of the proposed approach for active noise attenuation.

Second, a systematic approach for optimizing secondary sources was presented and verified. The procedure for optimizing secondary sources can be divided into three steps:

(a) Using the fictitious source strength distribution on the boundary obtained as an intermediate step in the primary field calculation, the optimal locations for secondary sources are estimated. Different strategies are applied for different cases. For global control of interior sound fields, it is important to have prior knowledge of the modal density distribution within the enclosure. Two criteria apply to interior global control cases, the magnitude of the fictitious source strength on the boundary and the nodal locations of adjacent resonant modes that could be inadvertently excited by secondary sources. For local control of interior sound fields or global control of exterior sound radiation, the only criterion for estimating the optimal locations of secondary sources is the magnitude of fictitious source strengths on the boundary.

(b) Once the optimal locations of the secondary sources have been estimated, the strength of the secondary sources can be optimized using a criterion of minimum squared pressure for observation points located in the region of interest. Usually, better results are obtained if the observation points are distributed in regions of high pressure magnitude of the primary sound field.

(c) The optimal number of secondary sources can be estimated by checking the convergence of active control predictions. Although not investigated extensively in this work, the influence of the number of secondary sources was studied briefly in order to achieve optimal control of the primary sound field. Numerical predictions suggest that saturation of active control results were rapid with increasing number of secondary sources

Finally, the overall approach was investigated for a variety of examples of active noise control. Interior global control and local control, as well as exterior global control of sound radiation, were investigated. Some numerical results were also compared with experimental results and numerical results obtained by other researchers using other numerical techniques. Both normal velocity and normal acoustical impedance boundary conditions were considered.

The predicted active cancellation using the proposed approach turned out to be impressive and promising. The predicted results showed that the fictitious source strength distribution does provide a systematic way to find optimal locations for secondary sources and has significant potential as an efficient procedure for practical applications of active noise cancellation. At low exciting frequency or low modal density, significant reduction of the primary sound field can be achieved using properly located secondary sources. Generally, global control of interior sound fields is difficult when the driving frequency is high or the modal density near the driving frequency is high, but a combination of global control with local control seems to give good cancellation in selected regions of importance. Numerical predictions also indicated that there are exceptions to the criterion of high fictitious source strength. Because of the acoustical properties of the boundary and specific locations of boundary nodes, some boundary nodes with high fictitious source strengths are not optimal locations for secondary sources. In such situations, optimal locations for secondary sources could be found using other boundary nodes with slightly smaller fictitious source strengths. Numerical predictions confirmed that optimal locations for secondary sources would never be those boundary nodes with very small fictitious source strengths. Since there are normally multiple choices of boundary nodes with high fictitious source strengths, the exceptions observed do not inhibit the usefulness of the proposed approach. Numerical prediction also showed that boundary nodes close to the primary source are usually better locations for secondary sources than those far away from it. This is coincident with the conclusion obtained by other researchers that better cancellation can be achieved when secondary sources are within a half wave length of the primary source.

There are several significant advantages associated with the proposed approach. First, it provides a systematic method for determining candidates for optimal secondary source locations as part of the numerical prediction of the primary sound field. There is no auxiliary

procedure needed to obtain the fictitious source strength distribution on the boundary. Second, since there are often multiple choices of boundary nodes with high fictitious source strengths, the method offers design flexibility for a particular application. Similar optimal control results could be achieved with different locations of secondary sources, and thus other constraints in a particular application can be easily accommodated. Finally, the secondary sources used in this technique are baffled pistons mounted on the boundaries of the domain. This provides a relative simple way to implement the method in actual applications. There is no extra space required for the secondary sources. The proposed method is particularly promising for three-dimensional interior problems with limited space, such as the interior of any sort of vehicle or aircraft.

BIBLIOGRAPHY

[1] Lueg, P. Process of Silencing Sound Oscillations. U. S. Patent # 2,043,416, 1936.

[2] Leventhal, H. G. "Developments in Active Attenuators." Proceedings of Noise Control Conference (1976): 33-42.

[3] Jessel, M. and Mangiante, G. A. "Active Sound Absorbers in an Air Duct." Journal of Sound and Vibration 23 (1972): 383-390.

[4] Jessel, M. "Sound Evidence for a General Theory of Active Sound Absorption." Proceedings of Inter-noise 79 (1979): 169-174.

[5] Jessel, M. J. M. "Active Noise Reduction as an Experimental Application of General System Theory." Proceedings of Inter-noise 83 (1983): 411-414.

[6] Jessel, M. and Yamada, S. "Active Noise Control." Journal of the Acoustical Society of Japan 8 (1987): 151-154.

[7] Eriksson, L. J., Allie, M. C., Hoops, R. H. and Warner, J. V. "Higher Order Mode Cancellation in Ducts Using Active Noise Control." Inter-noise 89 (1989): 495-520.

[8] Zander, A. C. and Hansen, C. H. "Active control of Higher-order Acoustic Modes in Ducts." Journal of Acoustical Society of America 92 (1992): 244-257.

[9] Shepherd, I. C., Lafontaine, R. F. and Cabelli, A. "Active Attenuation in Turbulent Flow Ducts." Inter-noise 84 (1984): 497-502.

[10] Eghtesadi, Kh. and Leventhal, H. G. "Comparison of Active Attenuations of Noise in Ducts." Acoustics Letters 4, (10), (1981): 204-209.

[11] Elliott, S. J. and Nelson, P. A. "Models for Describing Active Noise Control in Ducts." Institute of Sound and Vibration Technical Report." No. 127 (1984).

[12] Hong, W. K. W., Eghtesadi, Kh. and Leventhal, H. G. "The Tight-coupled Monopole (TCM) and Tight-coupled Tandem (TCT) Attenuators: Theoretical Aspects and Experimental Attenuation in An Air Duct." Journal of Acoustical Society of America 81 (1987): 376-388.

[13] Munjal, M.L. and Eriksson, L. J. "An Analytical One-Dimensional Standing Wave Model of Linear Active Noise Control System in Duct." Journal of Acoustic Society of America 84 (1988): 1086-1093.

[14] Snyder, S. D. and Hanson, C. H. "Active Noise Control in Ducts: Some Physical Insights." Journal of Acoustical Society of America 86 (1989): 184-194.

[15] Swinbanks, M. A. "The Active Control of Sound Propagation in Long Ducts." Journal of Sound and Vibration 27 (1973): 411-436.

[16] Tichy, J., Warnaka, G. E. and Poole, L. A. "A study of Active Control of Noise in Ducts." Journal of Vibration, Acoustics, Stress and Reliability in Design 106 (1984): 399-404.

[17] Silcos, R. J. Lester, H. C. and Abler, S. B. "Evaluation of Active Noise Control in a Cylindrical Shell." Journal of Vibration, Acoustics, Stress and Reliability in Design 111 (1989): 337-342.

[18] Lester, H. C. and Fuller, C. R. "Active Control of Propeller-Induced Noise Fields Inside a Flexible Cylinder." AIAA Journal 28 (1990): 1374-1380.

[19] Lester, H. C and Fuller, C. R. "Mechanisms of Active Control for Noise Inside a Vibrating Cylinder." Proceedings of National Conference on Noise Control Engineering (1987): 371-376.

[20] Bullmore, A. J., Nelson, P. A. and Elliott, S. J. "Active Minimization of Acoustics Potential Energy in Harmonically Excited Cylindrical Enclosed Sound Fields." American Institute of Aeronautics and Astronautics 86 (1986): 1985.

[21] Salikuddin, M. and Ahuja, K. K. "Application of Localized Active Control to Reduce Propeller Noise Transmitted Through Fuselage Surface." Journal of Sound and Vibration 133 (1989): 467-481.

[22] Quinlan, D. "Active Control of Noise Radiated from Small Axial Flow Fans." Inter-noise 89 (1989): 479-482.

[23] Koopmam, G. H., Neise, W. and Chen, W. "Active Noise Control to Reduce the Blade Tone Noise of Centrifugal Fans." Journal of Vibration, Acoustics, Stress and Reliability in Design 110 (1988): 377-383.

[24] Angevine, O. L., Gupta, P. K. and Rushden, F. A. "Active Acoustic Absorbers for Low-Frequency Hum." 99th Meeting of the Acoustic Society of America (1980).

[25] Baker, B. B. and Copson, E. T. The Mathematical Theory of Huygen's Principle. Oxford University Press, 1939.

[26] Nelson, P. A., Curtis, A. R. D., Elliott, S. J. and Bullmore, A. J. "The Active Minimization of Harmonic Enclosed Sound Fields, Part I: Theory." Journal of Sound and Vibration 117 (1987): 1-13.

[27] Bullmore, A. J., Nelson, P. A., Curtis, A. R. D. and Elliott, S. J. "The Active Minimization of Harmonic Enclosed Sound Fields, Part II: A Computer Simulation." Journal of Sound and Vibration 117 (1987): 15-33.

[28] Elliott, S. J., Curtis, A. R. D., Bullmore, A. J. and Nelson, P. A. "The Active Minimization of Harmonic Enclosed Sound Fields, Part III: Experimental Verification." Journal of Sound and Vibration 117 (1987): 35-58.

[29] Molo, C. G. and Bernhard, R. J. "Generalized Method of Predicting Optimal Performance of Active Noise Controllers." AIAA Journal 27 (1989): 1473-1478.

[30] Sutcliffe, S. G. C. "A Demonstration of Active Noise Reduction in an Aircraft Cabin." Journal of Sound and Vibration 128 (1989): 358-360.

[31] Bullmore, A. J. Nelson, P. A. and Elliott, S. J. "The Active Minimization of Periodic Sound in Enclosures." Inter-noise 85 (1985): 575-578.

[32] Bullmore, A. J., Nelson, P. A and Elliott, S. J. "Active Control of Harmonic Enclosed Sound Fields of Low Modal Density; A Computer Simulation." Proceedings of the Institute of Acoustics 7 (1985): 55-64.

[33] Molo, C. G. and Bernhard, R. J. "The Optimal Performance of Active Noise Controllers in Three Dimensional Cavities." Society of Automotive Engineers 870994.

[34] Lin, C. Y. and Ma, Y. L. "An Acoustic Field-Fitting Method for Free Field Active Noise Control." Inter-noise 89 (1989): 505-508.

[35] White, A. D. and Cooper, D. G. "An Adaptive Controller for Multivariable Active Noise Control." Applied Acoustics 17 (1984): 99-109.

[36] Nelson, P. A., Curtis, A. R. D., Elliott, S. J. and Bullmore, A. J. "The Minimum Power Output of Free Field Point Sources and the Active Control of Sound." Journal of Sound and Vibration 116 (1987): 397-414.

[37] Nelson, P. A. Curtis, A. P. D. and Elliott, S. J. "Quadratic Optimization Problems in Active Control of Free and Enclosed Sound Fields." Proceedings of Institute of Acoustics 7 (1985) 45-53.

[38] Pierce, A. D. Acoustics: An Introduction to Its Physical Principles and Applications, McGraw-Hill Book Company, New York, 1981.

[39] Schenck, H. A. "Improved Integral Formulation for Acoustic Radiation Problems." Journal of the Acoustical Society of America, 44 (1967): 41-58.

[40] Filippi, P. J. T. "Layer Potentials and Acoustic Diffraction." Journal of Sound and Vibration 54 (1977): 473-500.

[41] Dongarra, J. J., Moler, C. B., Bunch, J. R. and Steward, G. W. Linpack: User's Guide, New York: Society for Industrial and Applied Mathematics, 1982.

[42] Kinsler, L. E., Frey, A. R., Coppens, A. B. and Sanders, J. V. Fundamentals of Acoustics, Third Edition, John Wiley & Sons, New York, 1982.

[43] Morse, P. M. and Ingard, K. U. Theoretical Acoustics, McGraw-Hill Book Company, New York, 1968.

[44] Seybert, A. F. and Cheng, C. Y. R. "Application of the Boundary Element Method to Acoustic Cavity Response and Muffler Analysis." Journal of Vibration, Acoustics, Stress and Reliability in Design, 109 (1987): 15-21.

[45] Kipp, C. R. "Prediction of Sound Fields in Acoustical Cavities Using the Boundary Element Method." MS thesis, Purdue University, West Lafayette, Indiana 1985.

APPENDIX A. SHAPE FUNCTIONS AND NUMERICAL QUADRATURE

The quadratic shape functions used in the numerical scheme for regular boundary elements are shown below.

For eight-noded rectangular element, the geometric shape functions are

$$N_1(\xi_1,\xi_2)=\frac{1}{4}(\xi_1+1)(\xi_2+1)(\xi_1+\xi_2-1)$$
$$N_2(\xi_1,\xi_2)=\frac{1}{4}(\xi_1-1)(\xi_2+1)(\xi_1-\xi_2+1)$$
$$N_3(\xi_1,\xi_2)=\frac{1}{4}(1-\xi_1)(\xi_2-1)(\xi_1+\xi_2+1)$$
$$N_4(\xi_1,\xi_2)=\frac{1}{4}(\xi_1+1)(\xi_2-1)(\xi_2-\xi_1+1)$$
$$N_5(\xi_1,\xi_2)=\frac{1}{2}(\xi_1+1)(1-\xi_2^2)$$
$$N_6(\xi_1,\xi_2)=\frac{1}{2}(\xi_2+1)(1-\xi_1^2)$$
$$N_7(\xi_1,\xi_2)=\frac{1}{2}(\xi_1-1)(\xi_2^2-1)$$
$$N_8(\xi_1,\xi_2)=\frac{1}{2}(1-\xi_2)(1-\xi_1^2) \qquad \text{(A.1)}$$

For a six-noded triangle, the geometric shape functions are

$$N_1(\xi_1,\xi_2)=\xi_1(2\xi_1-1)$$
$$N_2(\xi_1,\xi_2)=0$$

$$N_3(\xi_1,\xi_2)=\xi_2(2\xi_2-1)$$

$$N_4(\xi_1,\xi_2)=1-3(\xi_1+\xi_2)+2(\xi_1+\xi_2)^2$$

$$N_5(\xi_1,\xi_2)=4\xi_1(1-\xi_1-\xi_2)$$

$$N_6(\xi_1,\xi_2)=4\xi_1\xi_2$$

$$N_7(\xi_1,\xi_2)=0$$

$$N_8(\xi_1,\xi_2)=4\xi_2(1-\xi_1-\xi_2) \qquad \text{(A.2)}$$

For irregular boundary elements, i.e., for the corner and edge elements, the shape functions for geometry are the same as those for regular elements and the shape functions for acoustic variables are listed here. For an element with one corner as shown in figure A.1, the shape functions for acoustic variables are

$$N_1(\xi_1,\xi_2)=\frac{25}{64}(0.6-\xi_2)(1-\xi_1)-\frac{25}{64}(1+\xi_2)(1-\xi_1)(0.6-\xi_2)$$
$$-\frac{125}{192}(1-\xi_1)(0.6+\xi_1)(0.6-\xi_2)$$

$$N_2(\xi_1,\xi_2)=\frac{25}{64}(0.6-\xi_2)(0.6+\xi_1)-\frac{25}{64}(0.6+\xi_1)(1-\xi_1)(0.6-\xi_2)$$
$$-\frac{25}{64}(1+\xi_2)(0.6+\xi_1)(0.6-\xi_2)$$

$$N_3(\xi_1,\xi_2)=\frac{25}{64}(1+\xi_2)(0.6+\xi_1)-\frac{25}{64}(1+\xi_2)(1-\xi_1)(0.6+\xi_2)$$
$$-\frac{125}{192}(1+\xi_2)(0.6+\xi_1)(0.6-\xi_2)$$

$$N_4(\xi_1,\xi_2)=\frac{25}{64}(1+\xi_2)(1-\xi_1)-\frac{125}{192}(1+\xi_2)(1-\xi_1)(0.6+\xi_1)$$
$$-\frac{125}{192}(1-\xi_1)(1+\xi_2)(0.6-\xi_2)$$

$$N_5(\xi_1,\xi_2)=\frac{25}{24}(1+\xi_2)(1-\xi_1)(0.6-\xi_2)$$

$$N_6(\xi_1,\xi_2)=\frac{25}{24}(0.6+\xi_1)(1-\xi_1)(0.6-\xi_2)$$

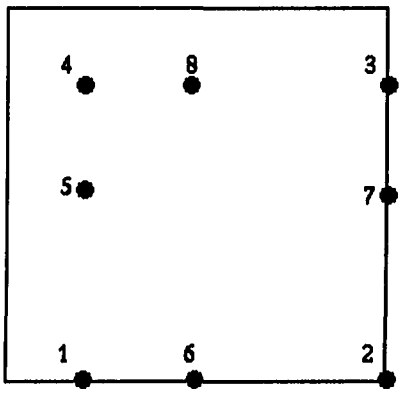

Figure A.1: Element with one corner.

$$N_7(\xi_1,\xi_2)=\frac{25}{24}(1+\xi_2)(0.6+\xi_1)(0.6-\xi_2)$$
$$N_8(\xi_1,\xi_2)=\frac{25}{24}(1+\xi_2)(1-\xi_1)(0.6+\xi_1) \qquad (A.3)$$

For an element with one edge as shown in figure A.2, the shape functions for acoustic variables are

$$N_1(\xi_1,\xi_2)=\frac{5}{16}(1-\xi_2)(1-\xi_1)-\frac{5}{16}(1+\xi_2)(1-\xi_1)(1-\xi_2)$$
$$-\frac{25}{48}(1-\xi_1)(1-\xi_2)(0.6+\xi_1)$$
$$N_2(\xi_1,\xi_2)=\frac{5}{16}(1-\xi_2)(0.6+\xi_1)-\frac{5}{16}(0.6+\xi_1)(1-\xi_1)(1-\xi_2)$$
$$-\frac{5}{16}(1+\xi_2)(1-\xi_2)(0.6+\xi_1)$$
$$N_3(\xi_1,\xi_2)=\frac{5}{16}(1+\xi_2)(0.6+\xi_1)-\frac{5}{16}(1+\xi_2)(1-\xi_1)(0.6+\xi_1)$$
$$-\frac{5}{16}(1+\xi_2)(1-\xi_2)(0.6+\xi_1)$$
$$N_4(\xi_1,\xi_2)=\frac{5}{16}(1+\xi_2)(1-\xi_1)-\frac{5}{16}(1+\xi_2)(1-\xi_1)(1-\xi_2)$$
$$-\frac{25}{48}(1-\xi_1)(1+\xi_2)(0.6+\xi_1)$$

$$N_5(\xi_1,\xi_2)=\frac{5}{8}(1-\xi_2)(1+\xi_2)(1-\xi_1)$$
$$N_6(\xi_1,\xi_2)=\frac{5}{6}(1-\xi_2)(0.6+\xi_1)(1-\xi_1)$$
$$N_7(\xi_1,\xi_2)=\frac{5}{8}(1-\xi_2)(1+\xi_2)(0.6+\xi_1)$$
$$N_8(\xi_1,\xi_2)=\frac{5}{6}(0.6+\xi_1)(1+\xi_2)(1-\xi_1) \qquad \text{(A.4)}$$

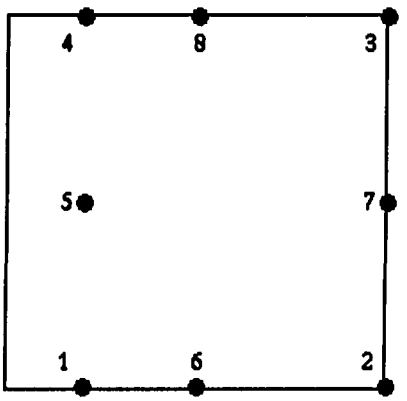

Figure A.2: Element with one edge.

For an element with two corners as shown in figure A.3, the shape functions for acoustic variables are

$$N_1(\xi_1,\xi_2)=\frac{25}{48}(0.6-\xi_2)(1-\xi_1)-\frac{125}{144}(0.6+\xi_2)(1-\xi_1)(0.6-\xi_2)$$
$$\frac{125}{144}(1-\xi_1)(0.6-\xi_2)(0.6+\xi_1)$$
$$N_2(\xi_1,\xi_2)=\frac{25}{48}(0.6-\xi_2)(0.6+\xi_1)-\frac{25}{48}(0.6+\xi_1)(1-\xi_1)(0.6-\xi_2)$$
$$\frac{125}{144}(0.6+\xi_2)(0.6-\xi_2)(0.6+\xi_1)$$
$$N_3(\xi_1,\xi_2)=\frac{25}{48}(0.6+\xi_2)(0.6+\xi_1)-\frac{125}{144}(0.6+\xi_2)(0.6+\xi_1)(0.6-\xi_2)$$
$$\frac{25}{48}(1-\xi_1)(0.6+\xi_2)(0.6+\xi_1)$$

$$N_4(\xi_1,\xi_2)=\frac{25}{48}(0.6+\xi_2)(1-\xi_1)-\frac{125}{144}(0.6+\xi_2)(1-\xi_1)(0.6-\xi_2)$$
$$-\frac{125}{144}(1-\xi_1)(0.6+\xi_2)(0.6+\xi_1)$$
$$N_5(\xi_1,\xi_2)=\frac{125}{72}(0.6+\xi_2)(1-\xi_1)(0.6-\xi_2)$$
$$N_6(\xi_1,\xi_2)=\frac{25}{18}(0.6+\xi_1)(1-\xi_1)(0.6-\xi_2)$$
$$N_7(\xi_1,\xi_2)=\frac{125}{72}(0.6+\xi_2)(0.6+\xi_1)(0.6-\xi_2)$$
$$N_8(\xi_1,\xi_2)=\frac{25}{18}(0.6+\xi_2)(1-\xi_1)(0.6+\xi_1) \qquad \text{(A.5)}$$

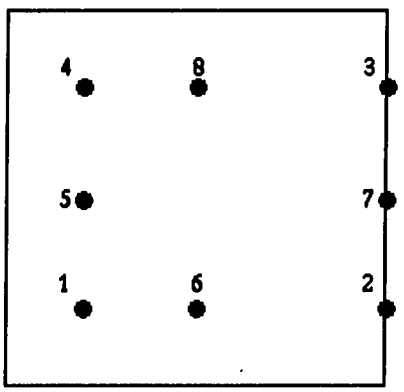

Figure A.3: Element with two corners.

For an element with two edges as shown in figure A.4, the shape functions for acoustic variables are

$$N_1(\xi_1,\xi_2)=\frac{5}{12}(0.6-\xi_2)(1-\xi_1)-\frac{25}{36}(0.6+\xi_2)(1-\xi_1)(0.6-\xi_2)$$
$$-\frac{5}{12}(1-\xi_1)(0.6-\xi_2)(1+\xi_1)$$
$$N_2(\xi_1,\xi_2)=\frac{5}{12}(0.6-\xi_2)(1+\xi_1)-\frac{5}{12}(1+\xi_1)(1-\xi_1)(0.6-\xi_2)$$
$$-\frac{25}{36}(0.6+\xi_2)(0.6-\xi_2)(1+\xi_1)$$

$$N_3(\xi_1,\xi_2)=\frac{5}{12}(0.6+\xi_2)(1+\xi_1)-\frac{25}{36}(0.6+\xi_2)(1+\xi_1)(0.6-\xi_2)$$
$$-\frac{5}{12}(1-\xi_1)(0.6+\xi_2)(1+\xi_1)$$
$$N_4(\xi_1,\xi_2)=\frac{5}{12}(0.6+\xi_2)(1-\xi_1)-\frac{25}{36}(0.6+\xi_2)(1-\xi_1)(0.6-\xi_2)$$
$$-\frac{5}{12}(1-\xi_1)(0.6+\xi_2)(1+\xi_1)$$
$$N_5(\xi_1,\xi_2)=\frac{25}{18}(0.6+\xi_2)(1-\xi_1)(0.6-\xi_2)$$
$$N_6(\xi_1,\xi_2)=\frac{5}{6}(1+\xi_1)(1-\xi_1)(0.6-\xi_2)$$
$$N_7(\xi_1,\xi_2)=\frac{25}{18}(0.6+\xi_2)(1+\xi_1)(0.6-\xi_2)$$
$$N_8(\xi_1,\xi_2)=\frac{5}{6}(0.6+\xi_2)(1-\xi_1)(1+\xi_1) \qquad \text{(A.6)}$$

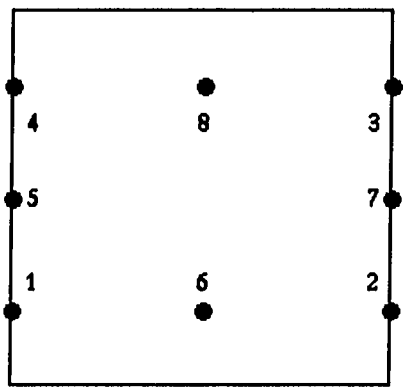

Figure A.4: Element with two edges.

For an element with four corners as shown in figure A.5, the shape functions for acoustic variables are

$$N_1(\xi_1,\xi_2)=\frac{25}{36}(0.6-\xi_2)(0.6-\xi_1)-\frac{125}{108}(0.6+\xi_2)(0.6-\xi_1)(0.6-\xi_2)$$
$$-\frac{125}{108}(0.6-\xi_1)(0.6-\xi_2)(0.6+\xi_1)$$

$$N_2(\xi_1,\xi_2)=\frac{25}{36}(0.6-\xi_2)(0.6+\xi_1)-\frac{125}{108}(0.6+\xi_1)(0.6-\xi_1)(0.6-\xi_2)$$
$$\frac{125}{108}(0.6+\xi_2)(0.6-\xi_2)(0.6+\xi_1)$$
$$N_3(\xi_1,\xi_2)=\frac{25}{36}(0.6+\xi_2)(0.6+\xi_1)-\frac{125}{108}(0.6+\xi_2)(0.6+\xi_1)(0.6-\xi_2)$$
$$\frac{125}{108}(0.6-\xi_1)(0.6+\xi_2)(0.6+\xi_1)$$
$$N_4(\xi_1,\xi_2)=\frac{25}{36}(0.6+\xi_2)(0.6-\xi_1)-\frac{125}{108}(0.6+\xi_2)(0.6-\xi_1)(0.6-\xi_2)$$
$$\frac{125}{108}(0.6-\xi_1)(0.6+\xi_2)(0.6+\xi_1)$$
$$N_5(\xi_1,\xi_2)=\frac{125}{54}(0.6+\xi_2)(0.6-\xi_1)(0.6-\xi_2)$$
$$N_6(\xi_1,\xi_2)=\frac{125}{54}(0.6+\xi_1)(0.6-\xi_1)(0.6-\xi_2)$$
$$N_7(\xi_1,\xi_2)=\frac{125}{54}(0.6+\xi_2)(0.6+\xi_1)(0.6-\xi_2)$$
$$N_8(\xi_1,\xi_2)=\frac{125}{54}(0.6+\xi_2)(0.6-\xi_1)(0.6+\xi_1) \qquad \text{(A.7)}$$

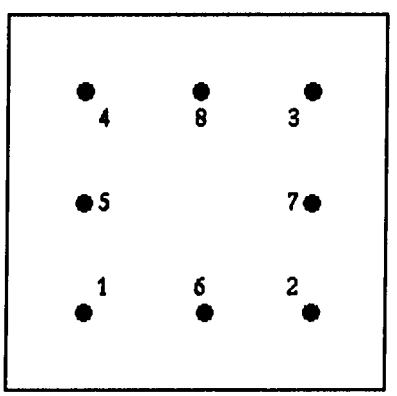

Figure A.5: Element with four corners.

Numerical quadrature over each element is performed in terms of the local coordinates (ξ_1,ξ_2) using Gaussian quadrature. If $f(\xi_1,\xi_2)$ is a function defined over an element area $\partial\Gamma$, the integral becomes

$$
\begin{aligned}
I &= \int_{\partial\Gamma} f(\xi_1,\xi_2)\,d\xi_1 d\xi_2 \\
&= \int_{-1}^{1}\int_{-1}^{1} f(\xi_1,\xi_2)\,d\xi_1 d\xi_2 \\
&= \sum_{i=1}^{n_1}\sum_{j=1}^{n_2} W_i W_j f(\xi_i,\xi_j)
\end{aligned}
\tag{A.8}
$$

where n_1 and n_2 are the number of Gauss points in the direction of ξ_1 and ξ_2, W_i and W_j the weight factors and ξ_i and ξ_j the abscissas of Gauss points. The shape functions for acoustic variables on these regular elements are the same as those for geometry.

APPENDIX B. RESONANT FREQUENCIES OF THE CAVITY

f(0 0 0) = 0.0000Hz	K = 0.0000
f(0 1 0) = 34.3000Hz	K = 0.6283
f(1 0 0) = 42.8750Hz	K = 0.7854
f(1 1 0) = 54.9068Hz	K = 1.0058
f(0 0 1) = 57.1667Hz	K = 1.0472
f(0 1 1) = 66.6672Hz	K = 1.2212
f(0 2 0) = 68.6000Hz	K = 1.2566
f(1 0 1) = 71.4583Hz	K = 1.3090
f(1 1 1) = 79.2640Hz	K = 1.4520
f(1 2 0) = 80.8964Hz	K = 1.4819
f(2 0 0) = 85.7500Hz	K = 1.5708
f(0 2 1) = 89.2972Hz	K = 1.6358
f(2 1 0) = 92.3556Hz	K = 1.6918
f(1 2 1) = 99.0568Hz	K = 1.8146
f(0 3 0) = 102.9000Hz	K = 1.8850
f(2 0 1) = 103.0587Hz	K = 1.8879
f(2 1 1) = 108.6167Hz	K = 1.9897
f(2 2 0) = 109.8136Hz	K = 2.0116
f(1 3 0) = 111.4750Hz	K = 2.0420

f(0 0 2) = 114.3333Hz	K = 2.0944
f(0 3 1) = 117.7134Hz	K = 2.1563
f(0 1 2) = 119.3675Hz	K = 2.1866
f(1 0 2) = 122.1081Hz	K = 2.2368
f(2 2 1) = 123.8025Hz	K = 2.2679
f(1 3 1) = 125.2785Hz	K = 2.2949
f(1 1 2) = 126.8340Hz	K = 2.3234
f(3 0 0) = 128.6250Hz	K = 2.3562
f(3 1 0) = 133.1198Hz	K = 2.4385
f(0 2 2) = 133.3344Hz	K = 2.4425
f(2 3 0) = 133.9458Hz	K = 2.4537
f(0 4 0) = 137.2000Hz	K = 2.5133
f(1 2 2) = 140.0583Hz	K = 2.5656
f(3 0 1) = 140.7566Hz	K = 2.5784
f(2 0 2) = 142.9167Hz	K = 2.6180
f(1 4 0) = 143.7432Hz	K = 2.6331
f(3 1 1) = 144.8755Hz	K = 2.6539
f(2 3 1) = 145.6348Hz	K = 2.6678
f(3 2 0) = 145.7750Hz	K = 2.6704
f(2 1 2) = 146.9750Hz	K = 2.6923
f(0 4 1) = 148.6333Hz	K = 2.7227
f(0 3 2) = 153.8198Hz	K = 2.8177
f(1 4 1) = 154.6937Hz	K = 2.8337
f(3 2 1) = 156.5835Hz	K = 2.8683
f(2 2 2) = 158.5280Hz	K = 2.9040

f(1 3 2) = 159.6834Hz	K = 2.9251
f(2 4 0) = 161.7928Hz	K = 2.9638
f(3 3 0) = 164.7204Hz	K = 3.0174
f(0 0 3) = 171.5000Hz	K = 3.1416
f(4 0 0) = 171.5000Hz	K = 3.1416
f(2 4 1) = 171.5953Hz	K = 3.1433
f(3 0 2) = 172.0945Hz	K = 3.1525
f(3 3 1) = 174.3583Hz	K = 3.1940
f(0 1 3) = 174.8964Hz	K = 3.2038
f(4 1 0) = 174.8964Hz	K = 3.2038
f(3 1 2) = 175.4793Hz	K = 3.2145
f(2 3 2) = 176.1068Hz	K = 3.2260
f(1 0 3) = 176.7782Hz	K = 3.2383
f(0 4 2) = 178.5944Hz	K = 3.2716
f(1 1 3) = 180.0750Hz	K = 3.2987
f(4 0 1) = 180.7769Hz	K = 3.3115
f(1 4 2) = 183.6688Hz	K = 3.3645
f(4 1 1) = 184.0021Hz	K = 3.3706
f(0 2 3) = 184.7112Hz	K = 3.3836
f(4 2 0) = 184.7112Hz	K = 3.3836
f(3 2 2) = 185.2632Hz	K = 3.3937
f(3 4 0) = 188.0644Hz	K = 3.4450
f(1 2 3) = 189.6219Hz	K = 3.4736
f(2 0 3) = 191.7428Hz	K = 3.5124
f(4 2 1) = 193.3552Hz	K = 3.5419